POLITECNICO DI TORINO

Corso di Laurea Magistrale
in Ingegneria Energetica e Nucleare

Tesi di Laurea Magistrale

Synthesis and characterization of perovskites for hydrogen production: study and modelling of a two-step Thermochemical green water splitting cycle.

Relatore/i

Prof. Monica Ferraris
Dr. Salvatore Sau
Dr Anna Chiara Tizzoni

Candidato

Francesco Nucci

Anno Accademico 2022-2023

Dal laboratorio se ne usciva ogni sera, e più acutamente a fine corso, con la sensazione di avere "imparato a fare una cosa";

il che, la vita lo insegna, è diverso dall'avere "imparato una cosa".

(Primo Levi)

Ringraziamenti

Si ringraziano la dott.ssa Francesca Varsano, la dott.ssa Laura Silvestri, Stefano Pucciarmati per la dedizione e l'assistenza nelle fasi di sintesi dei materiali.

Si ringrazia Cadia D'Ottavi, dell'università UniRoma2(la concorrenza) per l'indispensabile contributo riguardo l'analisi strutturale e morfologica.

Si ringrazia l'ing. Alberto Giaconia e l'ing. Gianpaolo Caputo per il prezioso aiuto riguardo l'allestimento del sistema in scala laboratorio.

Siete tantissimi, sicuramente ne ho dimenticato qualcuno (questo non significa che non vi penso)

Ringrazio di cuore tutti i membri del laboratorio TERIN-STSN-SCIS: Michela, Annarita, Natale, Luca, Valeria, Walter, Remo, Raffaele, Elena, Giuseppe, Adio, Daniele, Ettore, Cinzia, Elisabetta e Marco.

In particolare, l'ing. Michela Lanchi, indispensabile per la parte di flow sheeting e l'ing. Luca Turchetti, sempre attento e preciso nel correggere pure le virgole.

Sinceri ringraziamenti, anche, ad Annarita per il contributo sulla macinazione ad alta energia ed a Natale, per aver sopportato tutte cose di un tesista medio non retribuito.

Ringrazio di cuore la professoressa Monica Ferraris per la sua disponibilità e gentilezza.

Ringrazio infinitamente la Doc. Anna Chiara Tinozzi e il dott. Salvatore Sau per la gentilezza, la disponibilità, la presenza, l'esperienza e una serie interminabile di altre qualità.

Ringrazio di cuore la mia famiglia e gli amici, per il supporto che non è mai mancato, nonostante le note di pazzia che si sono verificate sempre più di frequente nell'ultimo lustro.

Ringrazierei anche me stesso, ma non mi va e devo consegnare la tesi!

ABSTRACT

Human activity and energy demand are responsible for many atmospheric emissions, so research into innovative technologies for their reduction will be of paramount interest in the coming decades. Concentrating solar plants (CSP) can convert heat from concentrated solar power into chemical energy which can then be used for several applications, such as thermal green hydrogen production. In this regard, two-steps thermochemical water-splitting cycles (TWSC) using perovskite powders are pioneering technologies for contributing to decarbonise the energy sector, as these processes can reduce operating temperatures, facilitating a more efficient coupling with CSP.

The present work is concerned with the evaluation of the redox capabilities of three different perovskites, selected after a screening of the powders already considered in the literature. The selected perovskites are: $La_{0.8}Al_{0.2}FeO_3\ (LAF\ 20)$ and $Ca_{0.8}Sr_{0.2}MnO_3\ (CSM\ 20)$, which are known from the literature, and $La_{0.8}Sr_{0.2}FeO_3\ (LSF\ 20)$, which is a new material not investigated yet. To understand the best way to produce the powders, taking into account scalability and safety criteria, several synthesis methods were tested. Considering a maximum thermal limit at 1000°C, which allows an efficient use of heat from currently available CPSs, the thermodynamics of the redox reactions were analysed to find a couple of temperatures, one for reduction and one for oxidation; in these conditions, the standard Gibbs free energy of the oxidation reaction with steam is equal or lower than zero, making hydrogen formation favourable. In addition, to fully characterise the redox reactions, a kinetic study was also carried out implementing with MATLAB a shrinking core model. To estimate the hydrogen yield, a laboratory-scale system was designed, representative of both the cycles reactions.

All these evaluations were supported by an exhaustive experimental campaign, including X-ray diffraction (XRD), to check the purity of the synthetized powders, thermogravimetric analysis (TGA) and differential scanning calorimetry (DSC) to calculate conversion rates along with specific and reaction heats, and scanning electron microscopy (SEM) to estimate the average particles size.

Summary

The fool doth think he is wise, but the wise man knows himself to be a fool.

[WILLIAM SHAKESPEARE, As You Like It]

1 Introduction

1.1 Climate change

Climate change is a problem related with the average rising temperature of the earth. The human activities of the last two centuries are the main driver of this problem, primary due to the massive exploitation of the fossil fuels.

Nowadays, according to Figure 1, the share of the fossil fuels for energy production is higher than 70%. The combustion of these fuels is the main responsible of the emission of the so-called greenhouse gases (GHGs), like carbon dioxide (CO_2), that traps the sun heat in the atmosphere causing the rising of temperature.

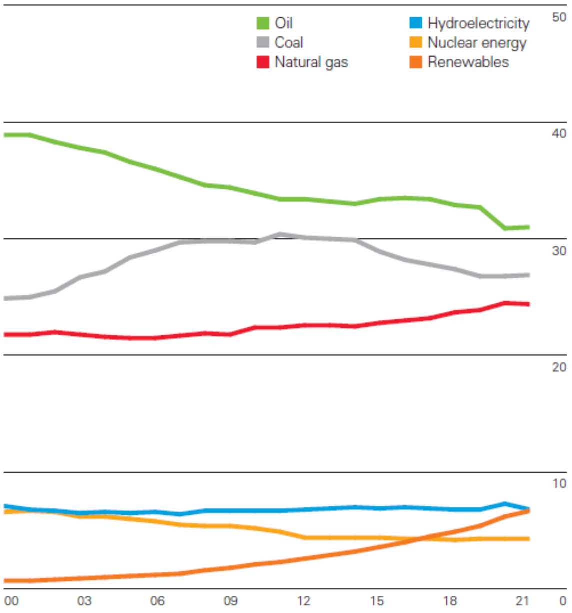

Figure 1-Shares of global energy source [1]

As a result, the average temperature of the earth is 1.1 °C higher with respect to the preindustrial period [2] and the decade 2011-2020 was the warmest on record [3].Moreover, this is not the only consequence: climate change is responsible for the reduction in the biodiversity and for increasing the probability of the devastating events, which, in turn, lead to poverty, water scarcity and so on [4].

Several possible scenarios have been done by different organizations with the aim to forecast the greenhouse emissions in the 2050: in each of them the renewables energy cover a different percentage of the global energy mix. To maintain the global increasing average temperature below 1.5°C this share should be over 90% [5].

1.2 Renewables Energy

In the energy production sector, renewable sources represent the possible environmentally clean alternative to fossil fuels. The main advantage refers to their infinite nature, so they will not run out and can be replenished at a higher rate that they are consumed. Therefore, their exploitation on a large scale reduces the GHGs, helping and speeding up the decarbonization of the energy sector.

Renewable energy systems (RES) include bioenergy, geothermal, hydropower, ocean and wave energy, solar and wind energy, and green hydrogen.

The development of these clean and innovative technologies is incentivized by the increasing of the annual global energy demand and the related impacts on global warming and environmental pollution.

Nowadays, the total renewable energy generation capacity covers about the 29% of the global energy mix [6] and to encourage the energy transition, it is expected that this value will increase in the future. In fact, in Figure 2, it is possible to appreciate the upward trends from 2010 to 2021 related to renewable power generation.

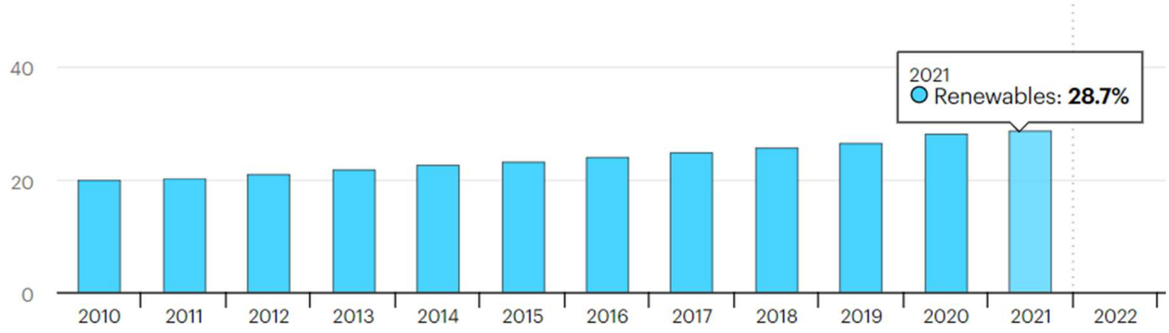

Figure 2-Renewables share of power generation. [6]

1.2.1 Solar Energy

In this context, solar energy can play a fundamental role thanks to the huge and diffuse availability of the solar radiation. Imaging the earth as a plate disk, the solar irradiation would be 1377 W/m^2, but due to the shape of the earth and the presence of the atmosphere, this is lower than ten times.

However, even considering this lowered value, the word energy consumption could be covered by harvesting al allow percentage of the solar irradiation.

Furthermore, shown Figure 3 , a significant percentage of investments in renewables regards solar energy, suggesting that investors see this technology as the dominant one in future scenarios.

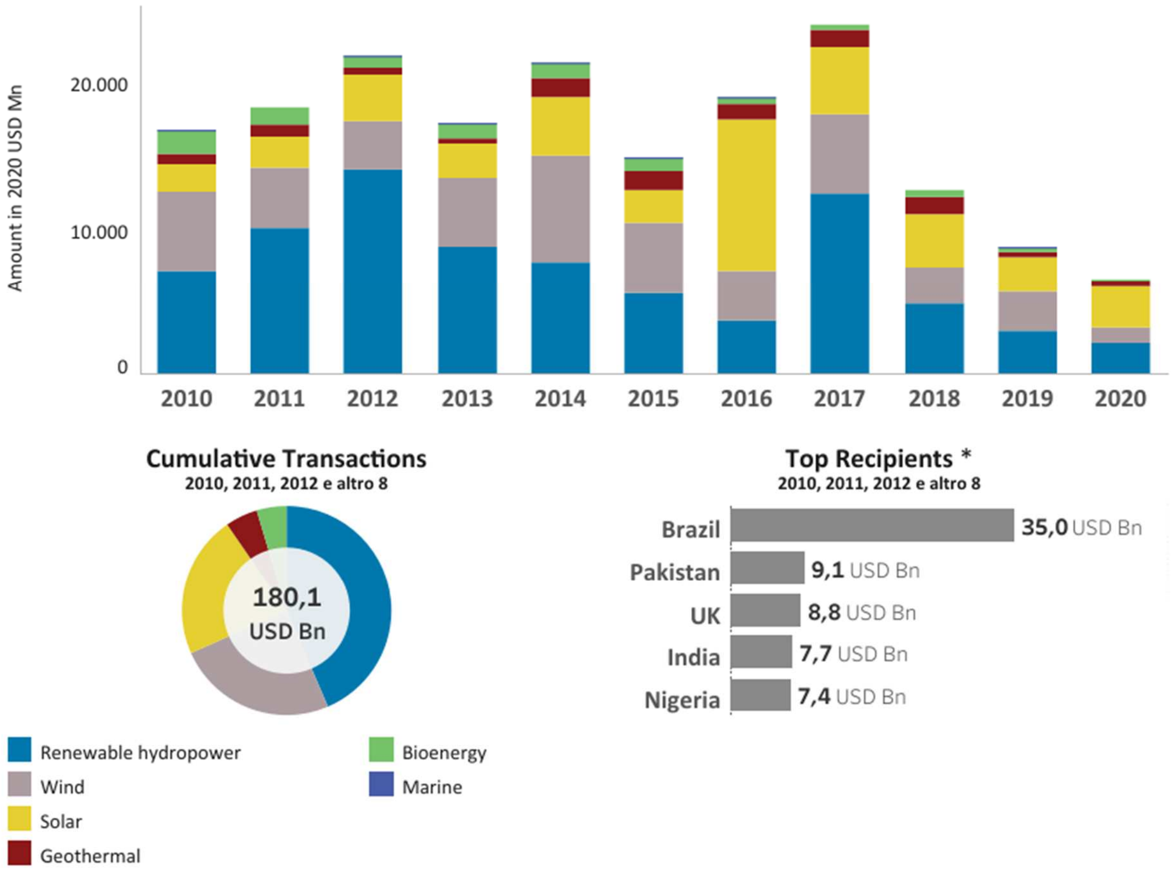

Figure 3-Public investment renewable trends from 2010 to 2020 [7] .

Nowadays only two technologies are used to exploit solar energy: Photovoltaic (PV) and Concentrated Solar Power (CSP).

Photovoltaic systems use both direct (sunrays that reach the earth surface without direction changes) and scattered (rays deviated, for instance, by the atmosphere and the environment) solar radiation, and, consequently, they are suitable also in zones with low irradiation.

On the other hand, concentrated solar power systems can exploit only the direct normal irradiation to produce heat at high temperature, thus they should be located in zonas where the solar irradiation is sufficiently high. Places like the Mediterranean Sea region, Spain, Marocco and so on presents high solar irradiation, and therefore conditions suitable for CSP installations.

Among the various solar technologies, Concentrated Solar Power systems can offer, in a medium-term perspective, a significant contribution to the production of both thermal energy and electricity in a sustainable way.

1.3 Concentrating Solar Power (CSP)

The basic idea of these plants is to concentrate, using mirrors or lenses, the direct normal irradiation on a specific point or area, called receiver. The radiation is then absorbed and transferred to a heat transfer media (typically a fluid, HTF), that can be used to directly feed a thermodynamic cycle, or as storage media to accumulate all or a part of the absorbed energy. The first path Is related to the pure energy production exploiting solar radiation, while the last one is used to improve the flexibility of a plant.

To give an order of magnitude, about 300 GWh/year of electric energy could be potentially produced per square kilometre of solar receiver surface. This is equal to the yearly production of a traditional thermoelectrical plant working for 6000 hours/year. In this way, about 500,000 oil barrels per year will not be consumed, with a reduction of CO_2 emission of around 200,000 tons/year [8].

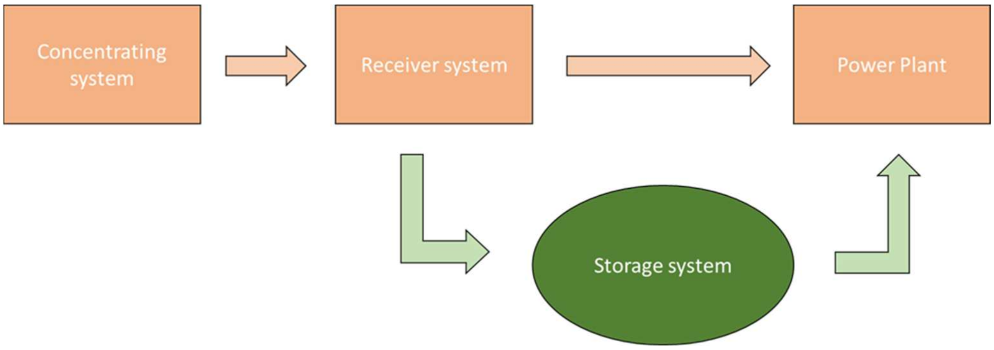

Figure 4-Figure 4-Schematic sketch of CSP plant

In Figure 4, a very simple sketch of a CSP plants is represented. When the solar heat is transferred to the receiver system two possibility are available: store it with a storage system or directly send it to the power plant.

The usage of thermal storage system increases the reliability and the flexibility of the whole plant because it allows to accumulate the extra solar heat and utilizes it when solar radiation is not available, solving the problem of the time delay between production or availability of energy and its consumption in receiving system (power plant, cogeneration, etc). In this way, the storage system makes it possible to use the available solar heat source for more hours per day in relation to the available solar hours [9], [10].

From an economic point of view, as represented in Figure 5, the levelized cost of energy (LCOE) of Concentrated solar power system could be comparable with the LCOE of the fossil fuels.

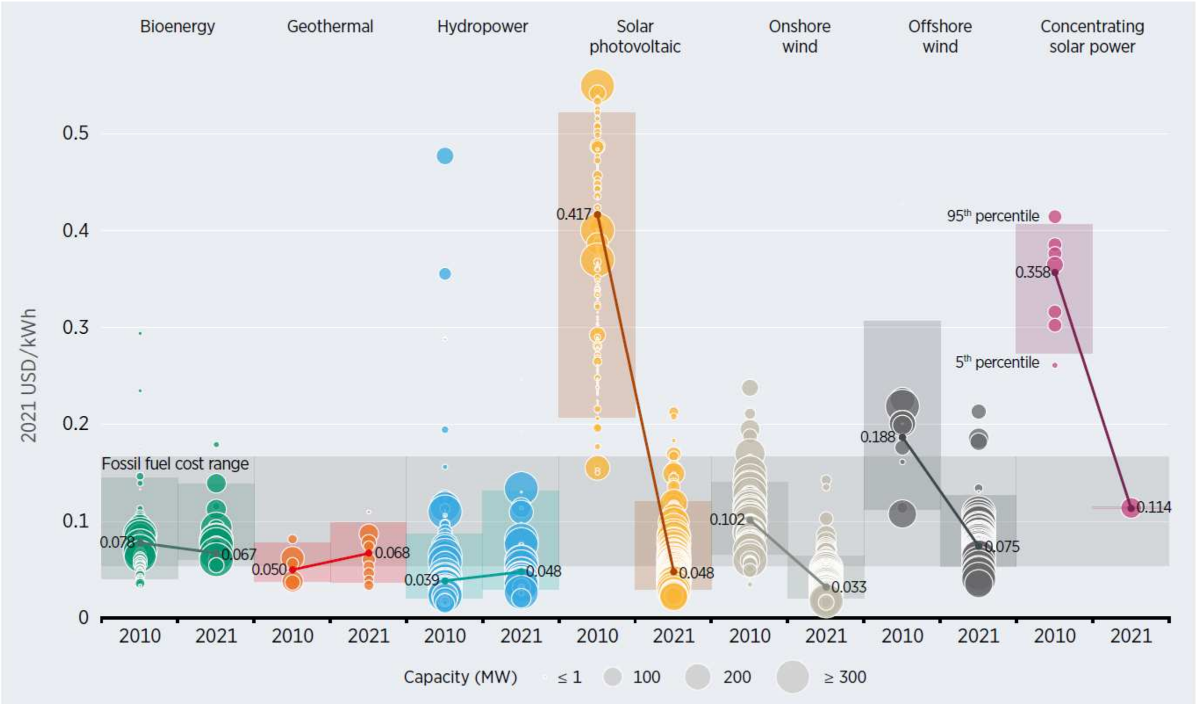

Figure 5- Global weighted average LCOEs from newly commissioned, utility-scale renewable power generation [11]

Actually, the global weighted average LCOE of CSP declined by 68% over the period from 2010 to 2020 [11].

With further improvement this technology could play a fundamental role in the energy transition and in the decarbonization of the energy sector also from an economic perspective.

Typically, concentrating technologies can be divided in two different categories: point focusing and line focusing. Solar parabolic dish and solar tower characterize the first category, while parabolic trough and Fresnel reflector characterize the second one.

1.3.1 Solar-Parabolic Dish (SPD)

An SPD system is a parabolic point focusing CSP technology. This system is used to concentrate the solar radiation in the focal point of the parabolic dish, where the receiver is located. Typically, SPD systems are equipped with a two axis-tracking system, to follow the movement of the sun and optimize the concentration ratio. A Stirling/Brayton engine is typically installed in the focal point to utilize the concentrated solar energy to heat the cycle working fluid. In Figure 6 is reported a sketch of the SPD System.

Figure 6 -Solar parabolic Dish, ENEA, Casaccia, Roma,Italy

1.3.2 Parabolic trough collector (PTC)

A Parabolic Trough Collector (PTC) system is a parabolic line focusing CSP technology. In this kind of technology, the collectors, made of hundreds of parabolic troughs placed in parallel rows and aligned on a north-south axis, concentrate the solar energy on the receiver, which is an absorption tube. The orientation can be also on a east-west axis but the efficiency is lower than the other configuration.

PTC systems are equipped with a one axis-tracking system, generally oriented from east to west to collect the direct radiation during the entire sun-path.

The receiver of this system is a pipe which contains the heat transfer fluid, which is heated up during the day and then sent to the power block to produce electricity. The tubes are covered with absorbed materials, generally contained in an external vacuum tube, to reduce the heat transfer toward the external environment and increases the whole absorption efficiency. Typically, the heat transfer fluid, that is enclosed in the receiver system, can be molten salt or thermal oil [12].

Figure 7-Parabolic Trough collectors demonstrative plant ENEA, Casaccia, Rome, Italy

PTC systems are the most widespread CSP technology in the world and account for the main part of the global CSE production. Nowadays, globally, there are 77 operational parabolic-trough power plants and most of them are in Spain and in the United States [13].

1.3.3 Linear Fresnel reflectors

The basic idea behind linear Fresnel reflectors is very similar to the one of the PTC, but the parabolic concentrator is replaced by many flat mirror strips, that concentrate the solar radiation on to the absorber tube through which the working fluid is pumped.

Figure 8-Linear Fresnel collectors demonstrative plant ENEA, Casaccia, Rome, Italy

In 2014, the largest operational linear Fresnel-reflector CSP plant was installed in India, with a capacity of 125MW and a planned electricity generation of 280,000MWh/year [14].

1.3.4 Solar power tower

A Solar tower power plant is characterized by a heliostat field and a central tower, on the top of which is placed the receiver. The heliostat field is composed by a large number of mirrors equipped with a two-axis sun tracker, called heliostats, that concentrates the solar radiation on a zone of the central tower, and transformed into heat for the working fluid. The average solar flux impinging on the receiver can generally vary from 200 kW/m^2 to 1000 kW/m^2, providing an opportunity to achieve high working temperatures [13].

Figure 9-Solar Two Tower System[15]

In 2009, the Sierra Sun Tower, a modular two-tower system in the Mojave Desert, powered more than 5000 homes, and in 2010 construction began of the 392MW three-tower system of the Ivanpah Solar Electric Generating System located in California, USA. In this plant there are about 175,000 mirrors. This California plant has created more than 1000 jobs and will power more than 350,000 homes [13].

1.4 Hydrogen

Hydrogen, as reported in the periodic table, it is the lightest element and, since it composes the 90% of the visible in the universe [16], it is the atom most abundant in the molecules present in nature. Usually, it is stored in water, hydrocarbons, or organic matter; in its elementary form and at standard conditions of temperature and pressure it is colourless, odorless and non-toxic. The transition between the gaseous form and the liquid one happens at around -253 °C, while the solidification occurs at around -260 °C [17]. From an energetic point of view, hydrogen is the element with the highest mass specific energy, 142 MJ/Kg, at least 2.5 times greater than that contained in the same mass of any of the other fuels[18]. If the focus is switched to specific volumetric energy, this perspective changes because the hydrogen density is very low, about 14 times lower than air. Nevertheless, it remains a competitive fuel with respect to hydrocarbons.

In Table 1 the main physical and chemical properties are reported.

Table 1- Main hydrogen properties

	Melting Temperature	Boiling Temperature	Density	HHV	LHV	LHV (at 15°C, 1 atm)
H2	-259.14 °C	-252.87°C	0.084 kg/m^3	141.86 MJ/kg	119.93 MJ/kg	10.70 MJ/m^3

Compared with other fuels, hydrogen is the only one that in combustion process produces water without GHGs, such as carbon dioxide, in accordance with the following reaction:

$$H_2 + \frac{1}{2} O_2 \rightarrow H_2O \qquad \Delta h = -285 \frac{kj}{mol} \text{ [18]} \qquad \textit{Eq. 1}$$

Hydrogen ignition energy is very low, around the 10% of the one of the GPL [19], and it is flammable within large concentration range, between 4% and 75% in air[18]. Therefore, even small air infiltration could be very dangerous and can lead to significant safety problems. On the other hand, its autoignition temperature in air is higher than 500°C making hydrogen stable enough from a thermal viewpoint [18].

Nowadays, hydrogen is mainly used in the industrial sector, both in its pure gaseous and mixed form. It is, for instance, employed for oil reforming and for ammonia production. Furthermore, it can be used to decarbonise in the so called 'hard to abate' sectors, such as glass industry and steel industry, in which electrification is difficult and uncompetitive. Out of the industrial sector, hydrogen can be used as fuel for fuel cells, for electricity production or as a fuel for vehicles.

1.4.1 Green Hydrogen

As mentioned above, a main advantage in hydrogen employment is related to the non-production of GHSs during the combustion process. However, to correctly evaluate its sustainability from the emissions point of view, also its production process must be considered.

Several hydrogen production methods are reported in the scientific literature, and a colour is typically assigned according to the synthesis process. This is done to define with simplicity in which way hydrogen is extracted from other molecules. This classification is recognised at global level, and it is based on six different colours [20]:

1. **Brown hydrogen** is the hydrogen produced starting from coal gasification. This process is based on the partial oxidation of the coal at around 1000°C with syngas production, that is a mixture of gas mainly based on H_2 and CO. Subsequently, the syngas is subjected to purification in order to obtain sufficiently pure hydrogen. Evidently, this methodology is responsible for high CO_2 rate emissions.

2. **Grey Hydrogen** is the hydrogen produced starting from methane. The most used process is the methane steam reforming (SMR) at high temperature. In this methodology methane is reacted with vapor producing carbon monoxide and H_2, according to the reaction:

$$CH_4 + H_2O \rightarrow CO + 3H_2 \qquad \textit{Eq. 2}$$

Then, the carbon monoxide can react again with vapor producing carbon dioxide and H2, following the so-called Water-gas shift reaction:

$$CO + H_2O \rightarrow CO_2 + H_2 \qquad \textit{Eq. 3}$$

In the end, via a process called P-swing adsorption, carbon dioxide and the other impurities are removed from the gas stream obtaining a hydrogen flow approximately pure. Nowadays SMR is the most used technique to produce Hydrogen, the drawback is related to a non-zero environmental impact if the process is not combined with carbon capture system (CCS).

3. **Blue hydrogen** is the hydrogen produced starting from fossil fuels associated with carbon capture, utilization, and storage system (CCUS). This type of systems allows to store, for long or permanent periods the carbon dioxide produced. Even if these systems can be relatively expensive, they allow to significantly reduce CO2 emissions.
4. **Turquoise hydrogen** is the hydrogen produced by methane pyrolysis. Pyrolysis involves thermal decomposition of methane, generally starting from the natural gas and operating at temperatures higher than 1000°C without catalyst. The resulting products are hydrogen and solid carbon, which can be permanently stored. This is an emerging technique for H_2 production with lower carbon intensity than SMR.
5. **Pink hydrogen** is the hydrogen produced exploiting nuclear energy. As the produced electricity can be used, to feed water splitting through electrolysers, or as thermal energy, to feed water splitting through a thermochemical cycle [21]. From the emissions point of view, the nuclear energy does not produce any greenhouse gases, therefore this type of hydrogen can be considered as carbon free. However, only some countries have nuclear energy plants and pink can be produced hydrogen only in localized zones.
6. **Green hydrogen** is the hydrogen produced exploiting renewables energies. In fact, renewable energy systems can be used to produce electricity with very low carbon dioxide emissions, which can be subsequently converted into H2 exploiting water electrolysis. The electrolyse process is the water electrochemical conversion in H_2 and O_2. The reaction can be expressed as:

$$H_2O + 237{,}2\left(\frac{kJ}{mol}\right)_{el} + 48.6\left(\frac{kJ}{mol}\right)_{heat} \rightarrow H_2 + \frac{1}{2}O_2 \qquad \textit{Eq. 4}$$

Today, three different types of electrolysers are practically available: PEM, Alkaline systems and SOEC [22].

Anyway, water electrolysis is not the only way to produce green hydrogen with low carbon emissions. Indeed, it is possible to split the water molecule following another process, called thermolysis, in which thermal energy is employed to break the water-chemical bond.

The main problem of a direct water thermolysis is a temperature requirement higher than 2000°C. At these temperature levels problems related to material stability and products recombination can arises, making it difficult to take heat from renewable sources in efficient way.

A possible solution is trying to lower the splitting temperatures using so called thermochemical cycle, where hydrogen and oxygen are produced separately through different chemical reactions, and all intermediate reactants are totally recycled.

1.4.2 Hydrogen storage

Like other fuels, hydrogen can be stored for a long time. Storage systems allow to store a part or the whole hydrogen produced and release it when it is needed, increasing the flexibility of the facility or of the entire energy network. This is fundamental in green hydrogen contest because renewables sources are subjected to fluctuations, making systems feeded by RES less competitive than more stable systems, like fossil fuels. Actually, in terms of penetration in the global energy market, the success of the whole hydrogen supply-chain depends on how storage solutions will be implemented [23]. The available Hydrogen storage systems in commerce are mainly divided in two categories: Physical-based and Material-based systems. The first group includes three different kinds of storage:

1. **Compressed gas Hydrogen** can be stored in four different vessels; among them, the most used and cheapest are the fully metallic pressure vessel. Normally, they are made of aluminium or steel, and can withstand under pressures up to 500 bar. In industrial applications hydrogen is stored at 200/300 bar, but the mass storage efficiency of this kind of vessel, about 1%wt of hydrogen storage [24]
2. **Liquid/cryogenic H2 storage**, where hydrogen is cooled down and maintained at around -250 °C. Liquid hydrogen has higher density with respect to the compressed one; in fact, liquid hydrogen density is 72 g/L while compressed H_2 at 700 bar has 42 g/L [23]. Increasing the density also the energy density increases and, therefore, the potential of the storage. On the other hand, liquefaction is both time and energy consuming and up to 30% of energy content could be lost in this process [20],in contrast to about 10% energy loss in Compressed hydrogen storage[23]. Thus, this storage method is most often used for medium and large-scale storage.
3. **Cryo-compressed H2 storage.** In this configuration hydrogen is a supercritical gas. To realize that it is cooled down to -233°C and then compressed. This kind of storage allows to obtain high storage density, 80 g/L around 10 g/L higher than cryogenic storage. The disadvantage is the same of the Liquid/cryogenic H2 storage.

For what concern the material-based storage, it has only two main sub-groups: chemisorption and physisorption. In Chemisorption storage hydrogen molecule is split in its atoms and integrated into the chemical structure of the storage material. Metal hydrides is the most used material group, where the H_2-storage capacity can reach 12.6 % wt, around ten times higher than the compressed gas in fully metallic pressure vessel [23]. On the contrary, in physisorption storage, hydrogen molecule is physically absorbed on the surface of a solid that is then used as storage material. This physisorption process is easy to handle and reversible with rapid and lossless adsorption-desorption kinetics, because the Van Der Valls bonds created are weak. The involved materials, such as carbon-based species or zeolites, must have large surface area, to obtain a significant high number of sites to store hydrogen molecules. The efficiency of the storage depends also by the pore volumes and the operating conditions [20].

All the mentioned typologies of storage are thought for small of medium quantities of hydrogen, in accordance with the actual hydrogen utilization. In the next future, the role of hydrogen in different sectors could become fundamental and therefore could be requested to store larger quantity of this fuel. Today, the principal method to do this is building an artificial salt cavern able to store gaseous hydrogen. The salt cavern is used because salt is inert, and it would not react with H2 [23]. In Table 2 are reported the main characteristics of a salt cavern-systems.

Table 2-Main characteristics of a Salt Cavern

				[25]			
	Permeability	**Suitable depth range**	**Recommended dimensions**	**Pressure**	**Depth**	**Volume**	**Kg H2**
	highly impermeable to hydrogen	200–2000 m	are at least a height of 300 m and a diameter of 70 m	Up to 20 MPa and above (ref	1000m	700000 m^3	6000000kg at 20 MPa [26]

1.5 Project Context -POR-WP1.1LA1.1.33

The Paris agreement is a legally binding international treaty on climate change. Its goal is to limit global warning well below 2, preferably to 1.5 Celsius degree, compared to pre-industrial levels [27]. Beyond this, the European Union has the goal to reach the carbon neutrality before the 2050. Hydrogen can play a fundamental role to achieve this result because its usage does not cause carbon emissions and so atmospheric pollution. For what concern the production, if renewable energy sources are used, it can be carried out with low greenhouse emissions. Nowadays, hydrogen represents only 2% of the European energy mix: the target for the 2050 is to increase this share to 13/14% and use it for the decarbonization of carbon-intensive sectors. The cumulative investments in favour of green hydrogen by 2050 could be quantified between 180 and 470 billion euros [28].

Part of this capital investment is designed to Italy by means of the PNRR. PNRR is a document that describes how the next generation EU funds will be managed. Specifically, around one third of these funds is assigned for the green transition and a share is allocated for research and development regarding hydrogen [29].

In this context, this work was born from the collaboration between the ENEA-Casaccia research centre, MASE and the Politecnico di Torino. In particular, these activities are part of the objective of the research plan stipulated between ENEA and MASE.

The main purpose of this thesis is to study and analyse innovative redox materials for hydrogen production exploiting a two-step thermochemical water splitting.

2 Two-Step Thermochemical Cycle (Two-Step TCWS)

2.1 Steam Methane Reforming (SMR)

The most conventional way to produce hydrogen is through hydrocarbons reforming. The fuels mostly used for this process are natural gas (NG) and light hydrocarbons, such as ethane, propane, butane, and pentane [30]. In Figure 10 is represented a general flow diagram of natural gas steam reforming.

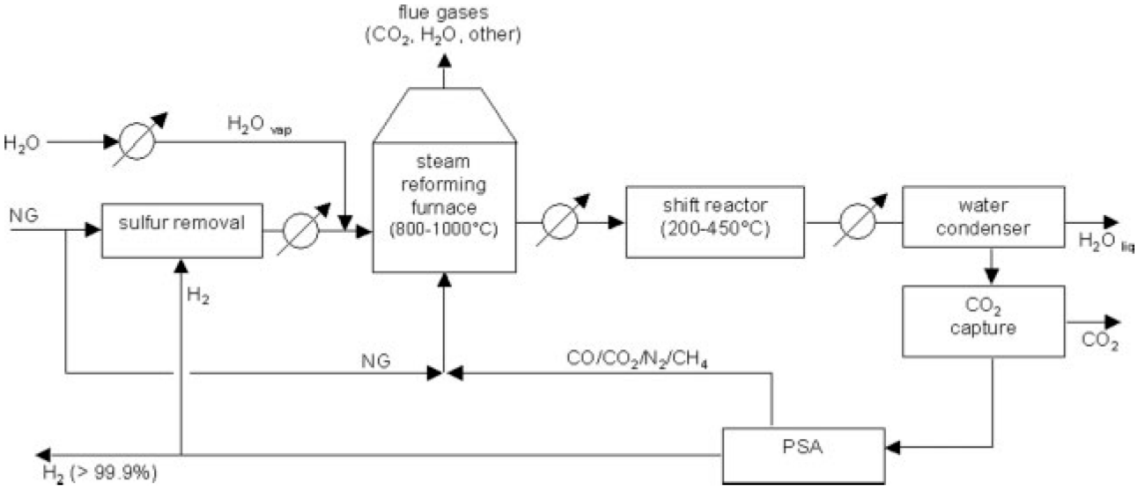

Figure 10-General sketch of a typical natural gas (NG) steam reforming process [31].

Usually, these reactants are contaminated with sulphur, mostly in form of in hydrogen sulphide (H_2S), which can be a poison for the reaction catalyst, and it is dangerous for the human health. Different purification technologies are used in relation to the amount of the sulphur content of the feedstock. The core of reforming process is the reactor in which occurs the following endothermic step:

$$CH_4 + H_2O \rightarrow 3H_2 + CO \qquad \Delta h = 206\frac{kJ}{mol} \quad [32] \qquad \text{Eq. 5}$$

The thermal energy needed by the reaction is obtained from the combustion of part of the initial fuel. What come from the steam methane reactor is a mixture of H_2, CO, unreacted methane and water, the so-called syngas. Hydrogen production can be further improved by further reacting carbon monoxide with steam, in a process called water gas shift reaction (WGSR):

$$CO + H_2O \rightarrow CO_2 + H_2 \qquad \Delta h = -\frac{41kJ}{mol} \, [32] \qquad \text{Eq. 6}$$

In general, even if almost all carbon monoxide and methane are transformed into hydrogen, the resulting gas mixture is still composed by unreacted water and methane plus carbon dioxide, which are to be removed by respectively a condenser and a clean-up system. The final product after is then nearly pure hydrogen.

With respect to this base method, two improvements can be done:

1. The residuals from the clean-up system can be recirculated to feed part of the thermal energy required by the burner.
2. The sensible heat of the two reactors products can be recovered and used for water vaporization.

The efficiency of the SMR process is calculated as:

$$\eta = \frac{G_{H_2} \cdot LHV_{H_2}}{G_{NG} \cdot LHV_{NG} + Auxialiary} \qquad \textit{Eq. 7}$$

In which:

- G_{H_2} is the produced hydrogen mass flow rate.
- LHV are the lower heating values of the hydrogen and the natural gas.
- G_{NG} is the feedstock mass flow rate.
- $Axualiary$ is the energy consumed to feed all the secondary systems that require energy.

For large plants the process efficiency can be in the order of 75% [33] with total emissions up to 0.3–0.4 kg of CO2 per cubic meter of hydrogen produced [30].

SMR is not the only way to produce hydrogen starting from fossil fuels, alternatives are:

- Dry reforming of methane (DRM), according to the reaction:

$$CH_4 + CO_2 \rightarrow 2CO + 2H_2,\ \Delta h(298\,K) = 247\,\frac{kJ}{mol}\,. \qquad \textit{Eq. 8}$$

Due to its endothermicity behaviour, the reaction is performed at high temperatures, in the order of 1273 K. The forward reaction is favoured at low pressures as dictated by stoichiometry [34].
Partial oxidation of the methane, following the reaction:

$$CH_4 + \frac{1}{2}O_2 \rightarrow CO + 2H_2\ \ [35]\,. \qquad \textit{Eq. 9}$$

As for the DRM, the reaction is also favoured at low pressure.
1. Coal gasification: this process can reach efficiencies up to 50%, around two times higher than for typical coal power plant fossil [36]. H_2 yield is highly variable depending on many factors, such as operating pressure, coal properties, injection agents and so on [37].

Hydrogen production by these kind methods is responsible for the 2.5 % of the total CO_2 emissions [38]. They should not be an option for a future sustainable hydrogen economy. An improvement to make hydrogen from fossil fuels competitive is to install carbon capture systems, but in the present state they are not economical and reduce considerably the production efficiency.

2.2 Water electrolysis

As already mentioned before, electrolysis is currently the reference technology for green hydrogen production. The basic idea is converting electricity produced by RES into chemical energy, in the form of hydrogen.

The available electrolysers can be divided in two subcategories: Low Temperature Electrolysis (LTE), in which the operating temperature is lower than 100°C and High Temperature Electrolysis (HTE), in which the operating temperature can reach 1000 °C. At commercial level, only the LTE are available, Alkaline Water Electrolyser (AWE) and Proton Exchange Membrane Water Electrolysers (PEMWE).

For what concern the HTE, although high Temperatures (close to 800°C) allow to reduce the input electrical energy up to 30 % [39], these systems are still in a research and development phase. The principal studies on HTE are focused on the cathode material and how to handle the high temperatures.

In Table 3 is reported a comparison between different electrolyser in terms of the principal operating parameters and the conversion efficiency, defined as $\frac{\dot{m} * LHV_{H_2}}{Electrical\ work}$ [40].

Table 3-Comparison of different water electrolysis technologies [41] .

		AWE	PEMWE	SOEC
Operational Temperature	$°C$	20-80	20-200	500-1000
Stack energy consumption	$\frac{kWh}{nm^3}$	4.2-5.9	4.2-5.5	>3
Lifetime of stack	kh	60-120	60-100	8-20
Hydrogen Purity	%	>99.8	99.999	-
Efficiency	%	59-70	65-82	Up to 100
TRL	$-$	9	7	5

2.2.1 Alkaline Water Electrolyser (AWE)

AWE is the most employed and mature electrolysis technology. The electrolyte is an alkaline solution composed by 25-30% of potassium hydroxide or sodium hydroxide[42]; water is fed in the cathode, and it is splitted in H_2 an OH^-, by electrons released from the anode, through an external metallic circuit. The hydroxide anion can pass through the electrolyte membrane reaching the anode, where both oxygen and water are formed. The governing semi-reactions are:

$$Cathode: H_2O + 2e^- \rightarrow 2OH^- + H_2$$

$$Anode: 4OH^- \rightarrow O_2 + 2H_2O + 4e^-$$

In Figure 11 the operational scheme of an AWE is reported.

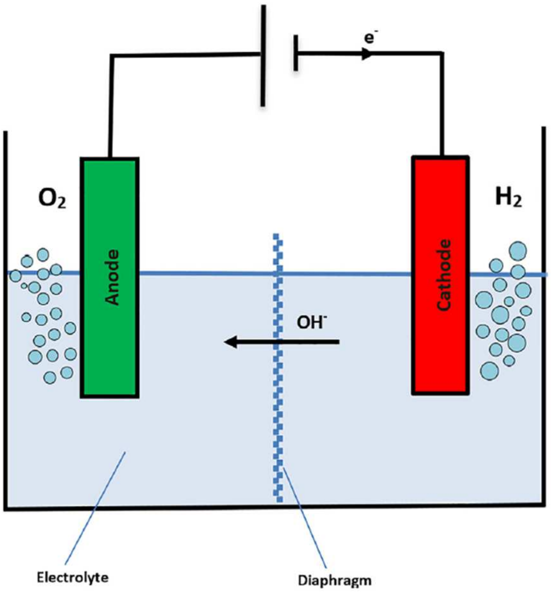

Figure 11-Operating diagram of an Alkaline Water Electrolyser[42].

The diaphragm allows the passage of the hydroxide ions from the cathode to the anode to maintain the charge balance. At present, most of AWE adopt tiny gap or zero gap structure, as reported in Figure 12. This is done to reduce the ohmic losses and increase the efficiency of the process [41].

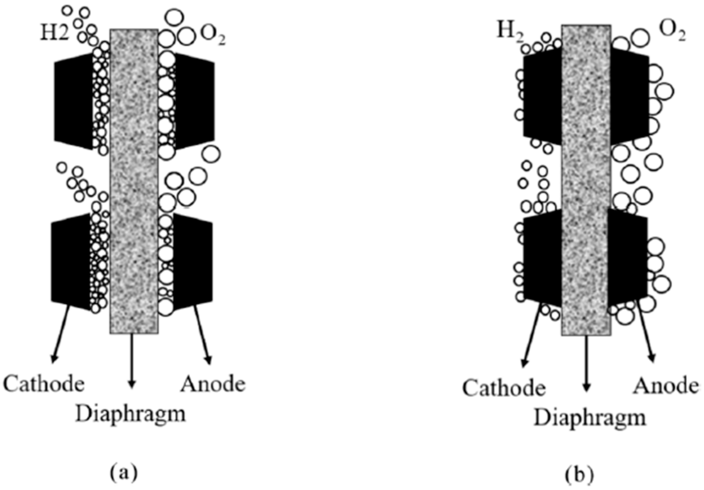

Figure 12-AWE electrolyser structure: (a) tiny gap and (b) zero gap [41].

2.2.2 Proton Exchange Membrane Water Electrolyser (PEMWE)

In a PEMWE water is fed at the anode side and through the electricity it is converted in oxygen and protons. The produced oxygen is taken out of the system and the protons can pass within the electrolyte to the cathode while electrons circulate to the cathode through an external circuit. At the cathode side, the electrons reduce protons, producing hydrogen [43]. The reactions occurring in a PEMWE are the following:

$$Anode: H_2O \rightarrow \frac{1}{2}O_2 + 2H^+ + 2e^- \text{ Oxygen Evolution Reaction (OER)}$$

$$Cathode: 2H^+ + 2e^- \rightarrow H_2 \text{ Hydrogen evolution Reaction (HER)}$$

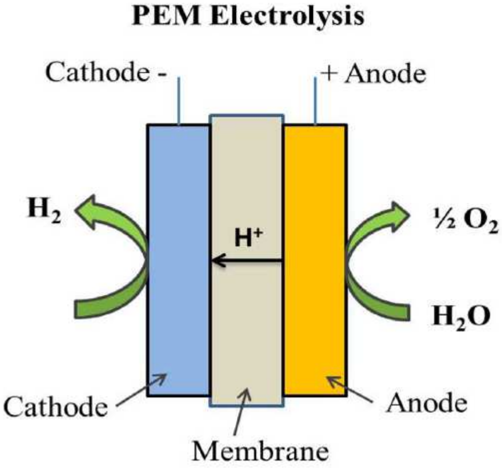

Figure 13-Schematic illustration of PEMWE [44].

In standard conditions (1 atm and 25°C), the Gibbs free energy of the global reaction is around $237\frac{kJ}{mol}$, it is higher than zero meaning that the water splitting is not spontaneous, thus it requires energy by an external source [43]. The electrolyte is typically made of Nafion, that is a modified structure of Teflon to which lateral chains containing a mobile ion in the end is added. The mobile ion is the SO^-_3 this sulphur ionic state allows the motion of the protons in the electrolyte layer. The ionic conductivity of the dry Nafion is very low, thus it must be hydrated with water. Due to the presence of water at 1 atm the operational temperature must be lower than 100 °C. Furthermore, PEMWE system requires a very good catalyst because there isn't the temperature contribution on the global reaction, platinum catalyst is a possible choice. Platinum is very active but suffers effect of impurities therefore the water used as spitting media should be controlled [45] .Of course, the usage of precious catalyst increases the cost for the electrolyser system.

2.3 Thermochemical cycles

The most interesting way to substitute the SMR and in general all the processes that include fossil fuels is water splitting. This can be obtained by electrolysis, providing electrical energy, or by thermolysis, using thermal energy. Regarding the latter, a promising alternative is to provide the necessary heat from CSP plants, still better if the system is coupled with a Thermal Energy Storage (TES) allowing to mitigate the effects of the climate fluctuations.

A direct Thermal Water Splitting (TWS) would occur at very high temperatures higher than 2000 °C [46], which are unaffordable for CSP plants material. Thus, to reduce the operating temperatures, more steps are considered for decomposing the water molecule [47]. Water splitting in more than one step is called "Thermochemical Water Splitting cycle" (TWSC). TWSCs involve water degradation through a series of reactions using recyclable substances, with the aim to make the process as much as possible reproducible and economical. Independently from the number of reactions, the cycle receives heat and water to produce hydrogen in addition to unreacted water, and no membrane is necessary for oxygen and hydrogen separation, because they are obtained in separate steps. TWSCs can be classified according with the number of steps involved in the cycle [48]. Two steps cycles normally require temperature in the order of 2000 K, while this value is reduced to less than 1200 K in some three steps TWSCs and to less than 800 K TWSCs involving more reactions. Another solution to reduce the temperature is introduce an electrochemical step, with the so called "hybrid" cycles [49].

Thermochemical cycles can be also classified in accordance with the thermal behaviour of the redox material. Volatile Thermochemical cycles involve temperature higher than the melting temperatures of the reduced species, thus at the end of the reduction step the resultant oxide is in its gaseous form. Volatile reaction has higher oxygen exchange capability, and the reduction is favoured by the entropy contribution generated in the phase transition. On the other hand, the reduction products must be quenched in order to avoid recombination with the stripped oxygen, the heat recovery more difficult. On the contrary, non-volatile Thermochemical Cycles involve temperatures lower than the melting point of the reduced material, hence during the cycle reagents are always in solid form, making easy the separation between the reduced product and the extracted oxygen. Non-volatile cycle can involve also non stochiometric oxides, which despite weaker oxygen storage capabilities, remain crystallographically stable during oxygen vacancies formation. Moreover, O_2 is the only gaseous species released during the solid-state partial reduction, thereby avoiding products recombination encountered for volatile oxides [50].

In Table 4 the redox reactions of some well-known cycles are reported.

Table 4- Redox reactions of some well-known two step redox cycles

		Reduction	Oxidation	Comments
Non-Volatile	Non-Stochiometric	$CeO_2 \rightarrow CeO_{2-\delta} + \frac{\delta}{2} O_2$ [51]	$CeO_{2-\delta} + \delta H_2O \rightarrow CeO_2 + \delta H_2$ [51] (Operating Temperature: 400-600 °C)[52]	It can also be used for CO_2 splitting.
	Stochiometric	$Fe_3O_4 \rightarrow 3FeO + \frac{1}{2} O_2$ (Endothermic, above 2500 K under 1 bar) [53]	$3FeO + H_2O \rightarrow Fe_3O_4 + H_2$ (Exothermic, <1000 K) [53]	Relatively high theoretical hydrogen yields. Avoid the recombination reactions and irreversibility associated with quenching needed with volatile- metal oxides such as zinc or cadmium oxides.
Volatile	Stochiometric	$ZnO \rightarrow Zn + \frac{1}{2} O_2$ [54] (Endothermic, 1700-1800 °C) [53]	$Zn + H_2O -> ZnO + H_2$ [54] (Exothermic, <1000 K) [53]	Maximum efficiency is equal to 29% [55]
		Step 1	Step 2	Step3
Sulphur based	Stochiometric	$H_2SO_4(aq) \rightarrow H_2O(g) + SO_3(g) \rightarrow H_2O(g) + SO_2(g) + ½ O_2(g)$ [49]	$2H_2O(l) + SO_2(g) \rightarrow H_2SO_4(aq) + H_2(g)$ (Endothermic at 800/900 °C) [49]	-
		$2H_2O(l) + x/2\ I_2(l) + SO_2(g) \rightarrow H_2SO_4(aq) + 2HI_x(aq)$ (Exothermic at 80/120°C) [56]	$2HI\ (aq, g) \rightarrow I2(g) + H2(g)$ (Exothermic at 300/450°C) [56]	$H_2SO_4(aq) \rightarrow H_2O(g) + SO_3(g) \rightarrow H_2O(g) + SO_2(g) + ½ O_2(g)$ (Endothermic at 800/900 °C) [56]

Nowadays, the attention is focused mainly on the non-volatile redox materials due to the absence of the quenching step and the possibility of the heat recovery. Currently, scientific investigations are focused on decreasing the thermal reduction temperature, to improve stability over the redox cycles, of the cycling instability, and to mitigate material sintering, with the final aim to increase H2 yield [57].

For solid intermediates, the most used method to reduce the thermal reduction temperature and increase the vacancy oxygen velocity is the doping of the redox material, either via the formation of more oxygen vacancies or by having the oxygen sites closer to each other. In the first case the undoped redox material is partially replaced by a metal with a smaller ionic radius, while in the second case the metal is partly substituted by a metal with a lower valency[58].

Hydrogen production tends to decrease with the increase of the number of steps involved in the cycle. Where solid species are employed, sintering is the most relevant cause, and a possible solution to overcome this problem is to support the redox material upon a proper structure [59].

2.4 Two-steps TWSC

Increasing the number of steps allows to reduce the operating temperature but can also increases the losses associated with heat transfer and products separation in each step. Moreover, each reaction can require different temperature levels that brings challenges in process integration [60].

Two steps thermochemical cycles can eliminate the largest part of these problems due to their relatively simplicity and operation feasibility. Typically, two step TCWSs are based on metal oxide pairs. The main idea is to convert concentrated solar energy through a solar reactor into chemical one, via the thermal reduction reaction:

$$MO_x \rightarrow MO_{x-\delta} + \frac{\delta}{2} O_2 \qquad \text{Eq. 10}$$

This step is endothermic and so requires heat, thus it is generally spontaneous at high temperatures. The temperature level changes with the involved redox pair. Eventually, the reduced oxide can be used to split the water molecule into green hydrogen, following the reaction:

$$MO_{x-\delta} + \delta H_2O \rightarrow MO_{x-\delta} + \delta H_2 \qquad \text{Eq. 11}$$

The oxidation reaction is exothermic; therefore, it is favourable at temperature lower with respect to the reduction step.

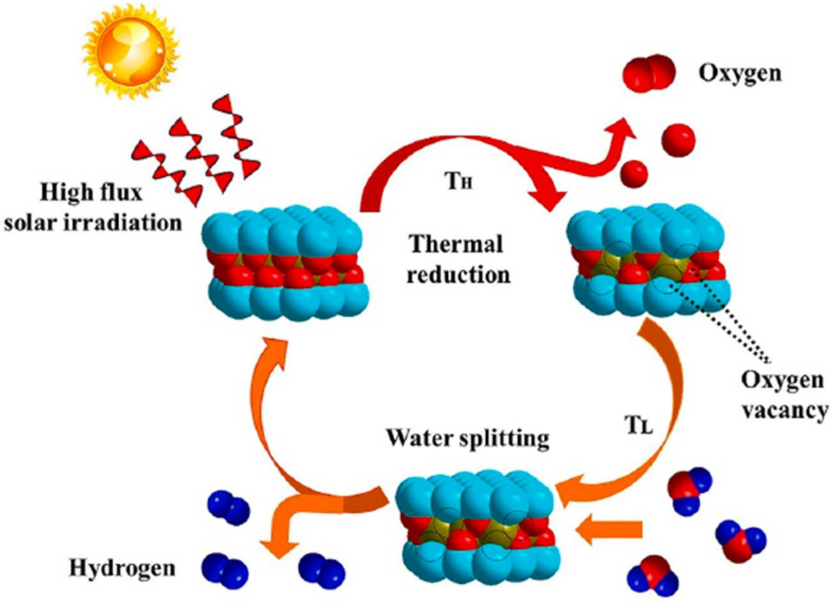

Figure 14-A diagram of solar-hydrogen production via two-step thermochemical [61].

In Figure 14 is reported a general scheme of two steps TWSC. Metal oxide redox pairs AND, more in general two step thermochemical cycles, can also be used to split other molecules, such as carbon dioxide following the reaction:

$$MO_{x-\delta} + \delta CO_2 \rightarrow MO_x + CO \text{ [62]} \qquad \textit{Eq. 12}$$

Alternatively, syngas can be produced by a combined reduction of water and CO_2.

As discussed above, solar reactors ban be utilized, directly or indirectly to drive the thermal reduction step. For a perfectly insulated blackbody cavity receiver the absorption efficiency is described as:

$$\eta_{Absorption} = 1 - \frac{\sigma \cdot T^4}{I \cdot C} \quad \text{[63]} \qquad \textit{Eq. 13}$$

Where:

- σ is Maxwell- Boltzmann constant.
- I is the incident normal beam insolation.
- T is the nominal cavity-receiver temperature.
- C mean normal flux over a target area normalised to the incident normal beam insolation I

The exergy efficiency defines how well solar energy is converted into chemical energy, stored as H_2 [64] and it is expressed as:

$$\eta_{Exergy} = \frac{\dot{n}_{H_2} \cdot \Delta G}{Q_{solar}} \qquad \textit{Eq. 14}$$

Where:

- $\dot{n}$ is the molar flow rate of hydrogen.
- ΔG is the standard Gibbs free energy of the oxidation reaction at 298 K.
- Q_{solar} is the detected solar radiation.

The solar conversion is limited not only by the $\eta_{Absorption}$ but also by the η_{Carnot}. Thus, the efficiency of an ideal solar thermochemical process is given by:

$$\eta_{Exergy,Ideal} = \eta_{Absorption} \cdot \eta_{Carnot} = (1 - \frac{\sigma \cdot T^4}{I \cdot C}) \cdot (1 - \frac{T_l}{T}) \qquad \textit{Eq. 15}$$

Where:

- T_l is the temperature of the thermal reservoir for heat rejection, typically ambient temperature.
- T is the operating temperature.

By placing the last equation equal to zero the maximum achievable temperature by an ideal solar reactor is obtained:

$$T_{Stagnation} = \left(\frac{I \cdot C}{\sigma}\right)^{0.25} \qquad \textit{Eq. 16}$$

In this condition the energy is re-irradiated at the same velocity at which is absorbed. Obviously, an energy-efficient process must operate at temperatures that are substantially below $T_{Stagnation}$. There is an optimum temperature for which the maximum efficiency is obtained:

$$\frac{\partial \eta_{Exergy,Ideal}}{\partial T} = 0 \qquad \textit{Eq. 17}$$

Assuming a uniform power flux distribution an explicit equation for the optimal temperature can be derived:

$$T_{opt}^{5} - (0.75T_{l})T_{opt}^{4} - \left(\frac{T_{l} \cdot I \cdot C}{4 \cdot \sigma}\right) = 0 \qquad \textit{Eq. 18}$$

If the concentration C is between 1000 and 13000, then T_{opt} is in the range between 1100 and 1800 K. Assuming the T_{opt} in the formula for the ideal exergy efficiency, the results give the maximum solar energy that can be ideally converted into hydrogen, neglecting conduction and convective heat transfer losses.

The exergy efficiency is an important criterion for judging the relative industrial potential of the solar process. The higher the exergy efficiency, the lower is the required solar collection area for producing a given amount of solar H2, and, consequently, the lower are the costs incurred for the solar concentrating system, which usually correspond to half of the total investments for the entire solar chemical plant. Thus, high exergy efficiency implies favourable economic competitiveness [63].

The global solar to fuel efficiency, which considers all the possible losses, can be defined as the ratio between the energy stored in the hydrogen flow and the solar energy absorbed by the solar system to produce it:

$$\eta_{Solar-To-Fuel} = \frac{n_{H_2} \cdot (HHV\ or\ LHV)}{Q_{Solar}} \qquad \textit{Eq. 19}$$

where:

- $n_{H_2}$are the produced hydrogen moles.
- HHV is the higher heating value.
- $LHV$is the lo lower heating value.

2.5 Reactor systems and methodologies

The selection of an appropriate reactor, in a possible industrial plant, is fundamental due to the involved high temperatures and because the cycle steps occur at different temperatures. Solar reactors can be used for these kind of reactions up to 2000°C, typically coupled with STP and SPD systems. A possible solar reactor configuration is proposed by Chueh et al. [57] and it is illustrated in Figure 15.

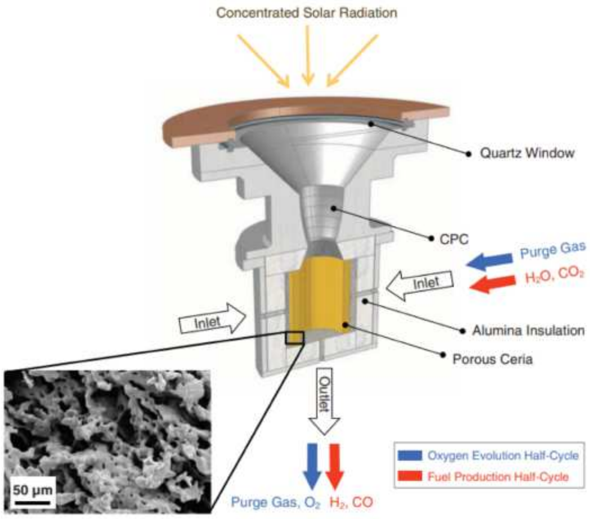

Figure 15-Schematic representation of the solar reactor used for thermochemical water and carbon dioxide splitting [57].

The solar radiation passes through a quartz window, and it concentrated onto the sample, that in this cases is porous ceria. Thermal reduction is performed at 1600°C for one hour while oxidation (with H_2 production) is carried out at 500°C, by passing a mixture of Ar and vapor on the reduced material for about 30 minutes [57].

Another possible solar reactor configuration was reviewed by Al-Shankiti et al [65],and it is represented in Figure 16.

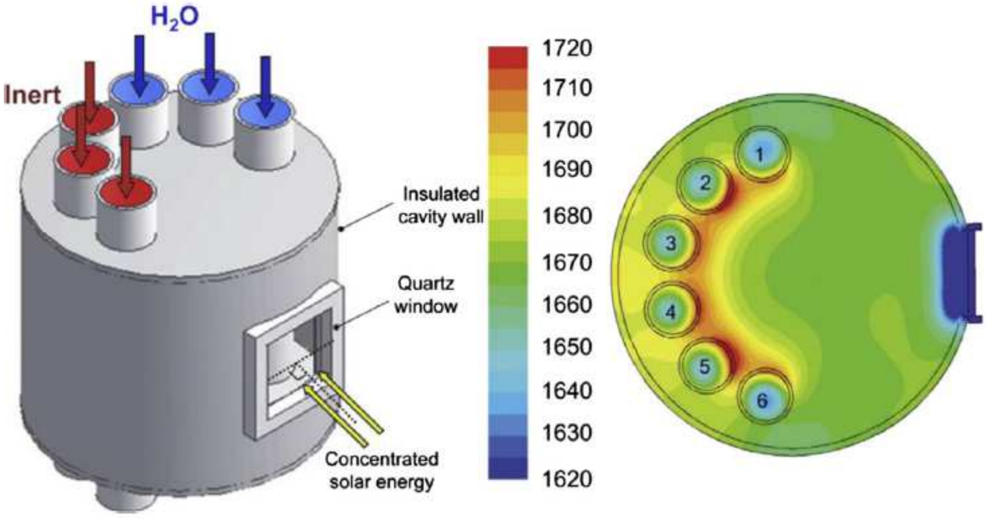

Figure 16-Packed Bed reactor used for thermochemical water splitting [65].

The receiver contains a packed bed reactor in which can be supplied the inert gas for the reduction and the vapor for the oxidation. Moreover, the redox material is indirectly radiated by the solar heat. In this configuration the reactor temperature is not uniform, and this issue might be mitigated by using a fluidizing bed reactor [65], proposed by Kodama et al. [66] and illustrated in Figure 17.

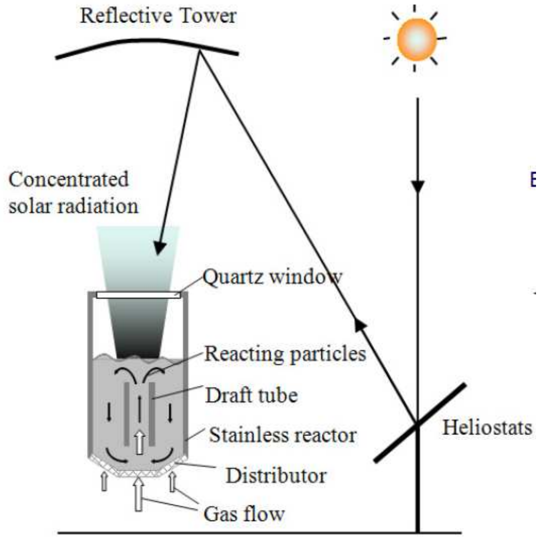

Figure 17-Windowed fluidized-bed reactor [66].

Also, in this case the solar radiation comes to the particles through a quartz window, leading to temperatures up to 1400 °C, while cooled to 1000°C for oxidation [66]. A reactor of this type is used for the thermal reduction of the Nife2O4 supported of monolithic zirconia, as proposed by Gowon et al. [67].

Other possible configurations can be:

- Infrared reactors, in which an infrared furnace is used. In this way the maximum achievable temperature is lower than the classical solar reactors, but it can be easily controlled.
- Microwave Ovens, [68]which present fast heating kinetics, but difficulties in temperatures control, which leads to a temperature gradient in the sample.

2.6 Perovskites based Two- Step TCWS

The considered materials for the two step cycles can be divided into two categories: pure metal oxide and mixed metal oxide. In general, pure metal oxides undergo stochiometric reaction and they present a very width operating temperatures range. For what concern mixed metal oxides, they present partial reduction reactions, obtaining, as a result, stable sub-stochiometric oxides. In this scenario, perovskites are particularly promising because in several cases they allow to work with temperature lower than 1000°C, opening the possibility of drawing heat efficiently from the currently available CSP systems [69]–[71].

Perovskites, present a general AMO_3, formula, and are mixed oxides in which A is a bivalent cation and M is a transition metal: whit respect to anions, the M cation is in a six-fold coordination while A cation is in a twelvefold coordination.
The ideal perovskite structure is represented in Figure 18 and can be obtained using a huge variety of A and M ions. Furthermore, the sites can be doped with some elements giving rise to complex oxides to tune the redox properties of the material maintaining the perovskite structure.

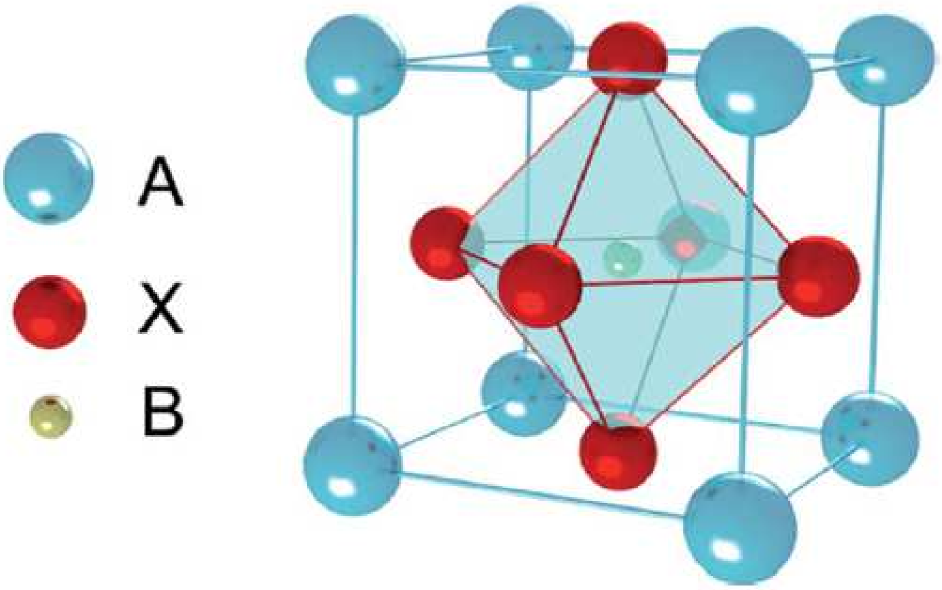

Figure 18-ABX_3 ideal perovskite structure with cation B at the centre of the unit cell [72]

Actually, the Perovskite structure is maintained, if the tolerance factor, t from the Goldschmidt relation [73], is near the unity:

$$t = \frac{r_A + r_o}{\sqrt{2} \cdot (r_M + r_o)} \qquad \textit{Eq. 20}$$

Where r_i is the radius of i-species.

If the tolerance factor is exactly one the structure is an ideal cube. Otherwise, also distorted structure can be formed, i.e. t>1.02 hexagonal structure is formed while if t<1 the structure should be orthorhombic and tetragonal phases [73]. Transition between these phases can take place during reduction due to changes in atomic radii of the cations. This parameter can be controlled varying the bivalent cation or the transition metal. By appropriately selecting M site ion, the enthalpy of reduction can be tuned over a very large range of $\Delta h = 100 - 500 \frac{kJ}{mol}$ [73].

In Figure 19 is reported a scheme of a two-step cycles involving mixed oxides with perovskite structure.

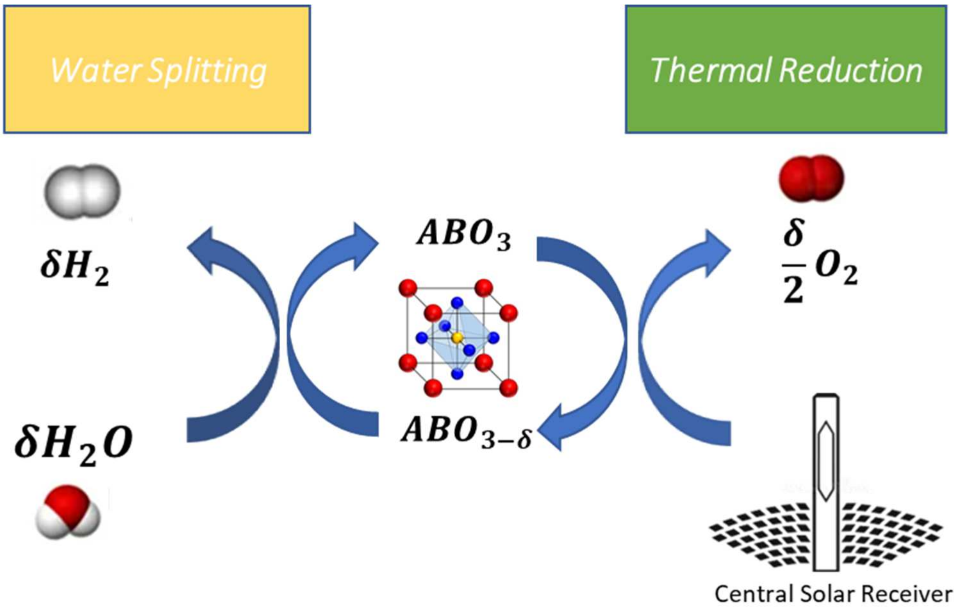

Figure 19-A diagram of solar-hydrogen production via two-step thermochemical filled with perovskite.

The reactions are:

$$TR\ (Thermal\ reduction):\quad ABO_3 \rightarrow ABO_{3-\delta} + \frac{\delta}{2}O_2 \qquad \text{Eq. 21}$$

$$\text{WS (Water shift)}:\quad ABO_{3-\delta} + \delta H_2O \rightarrow ABO_3 + \delta H_2 \qquad \text{Eq. 22}$$

The state of the art regarding this specific technology is still in a preliminary stage and for the most part the proposed materials required temperatures higher than 1000°C, making the match with CSP systems inefficient. Furthermore, some Perovskites contain toxic element such as Nickel and Cobalt, that today are possibly avoided for safety reason. The most used synthesis method is the “Pechini” one and its modified versions, in which an auto-combustion process is present. This method leads to high purity products, but it is not totally safe and likely not very scalable. Finally, the reoxidation thermogravimetric tests with vapor are generally performed with saturated inert gas at maximum 80°C, not considering how the partial pressure of the steam can influence the reaction.

The present state of art is summarized in Table 5.

Table 5-State of art review

Perovskite	Synthesis	TR-Temperature	WS-Temperature	Ref.
$La_{0,7}Sr_{0,3}Mn_{0,3}Cr_{0,1}O_3$	Modified Pechini Method	$1000 - 1350\ °C$	$1200\ °C$	[74]
$BaCe_{0,25}Mn_{0,75}O_3$	-	$1350\ °C$	$850\ °C$	[75]
$La_{1-x}Sr_xMeO_3 - Me = Mn, Co\ and\ Fe$	-	$LSM20 - 1150\ °C$ $LSM35 - 950\ °C$ $LSF - 800/550\ °C$ $LSC - 800\ °C$	$1400\ °C$	[76]
$La_{1-x}Ca_xCoO_3$	Modified Pechini Method	$1300 - 1600\ °C$	$900\ °C$	[77]
$CaTi_{0,5}Mn_{0,5}O_3$	Solid State Reaction	$1350\ °C$	$1150\ °C$	[78]
$La_{0,8}Al_{0,2}MeO_3 - Me = Fe, Co, Ni$	Modified Pechini Method	1000$°C$	800$°C$	[69]
$Sr_2CoNb_{1-x}Ti_xO_{6-\delta}$	Modified Pechini Method	$1000\ °C$	700 $°C$	[70]
$La_{0,8}Sr_{0,2}CoO_{3-\delta}$	Solid State Reaction At high temperature	$1000\ °C$	800$°C$	[71]

Starting from the available scientific literature, the aims of this thesis work are:

- Material safety: each used element is non-toxic.
- Synthesis method: the powders synthesis is carried out by high energy ball milling process followed by thermal calcination at high temperatures. Milling processes are totally safe and scalable.
- Reactions thermodynamic analysis.
- Reactions kinetic investigation.
- A qualitative evaluation of the whole cycle by a lab-scale equipment.
- Preliminary flow sheeting analyses of the water splitting process using experimental data.

2.7 Perovskite synthesis

As already mentioned before, Perovskites, as mixed nonstoichiometric oxides can be conveniently used below 1000°C to convert solar energy in green hydrogen. This work is concerned with the synthesis and the characterization of three different perovskites, with the aim to satisfy the assumed thermic limit. In particular, the powders were selected following several criteria:

1. The elements involved must be nontoxic and easily available.
2. One material was chosen among the ones already present in scientific literature to validate the synthesis method.
3. Then, the synthesis method was to prepare and characterize a material already proposed in the scientific literature, but not fully studied yet.
4. Synthesis of a new perovskite.

In Table 6 are reported the perovskites investigated in this thesis.

Table 6-Synthesized Perovskites

Available in literature	Theoretically Available in literature	Novel Perovskite does not present in literature
LAF 20:$La_{0.8}Al_{0.2}FeO_3$	CSM 20: $Ca_{0.8}Sr_{0.2}MnO_3$	LSF 20: $La_{0.8}Sr_{0.2}FeO_3$

As an alternative to the largely used “Pechini” method [79]–[81], various preparation routes synthesis methods have been attempts. Initially, the reactants in carbonate or nitrate form are mixed in demineralized water and isopropyl alcohol to create a homogeneous mixture. At this point the solution is heated to eliminate the solvents and possible NO_X. Finally, the resulting powder is subject to a calcination process at different temperatures, up to 1000°C.

Another method involved the use of acetates along with nitrates, exploiting the resulting exothermic reaction to promote the reaction between the different components.

However, both these two procedures were unsuccessfully in producing the target materials.

Perovskites can also be obtained directly by dry high energy generally followed by calcination [82]. The XRD analysis of the products showed the validity of the approach, meaning that is possible to use different milling methods with different materials and transfers the minimum amount of energy in order to activate the components, which subsequently are calcinated in order to form the Perovskite phase, with sufficiently high purity levels.

The method can be adapted to synthesize from 2 to 20 g of material, can, demonstrating the flexibility of this route in terms of scalability.

The detailed synthesis procedures and results are reported in the following chapters.

To globally characterized the milling process, a predictive model was used to evaluate the energy exchanged between the balls of the mill and the powders in the jar.

2.8 Laboratory-scale system for hydrogen production

Several experimental tests needed to be performed to ensure that, at least theoretically, oxidation with vapor is possible for the prepared perovskites. The synthesis powders were subjected to TGA analysis in order to understand their reduction capabilities, firstly under inert nitrogen and then under air. The redox cycle was completed oxidizing the reduced perovskites under air, with two scopes: study the samples under redox cycle and confirm that the oxidation, at least with oxygen, is possible at temperatures below 1000°C.

With this kind of experimentation was possibly know the "delta" of the reactions and compare the results with the ones achieved through the system for the direct measurement oxygen partial pressure, that will be described in the following chapters.

After completing all these preliminary tests, hydrogen production could be experimentally verified by the laboratory-scale facility, reported in Figure 20.

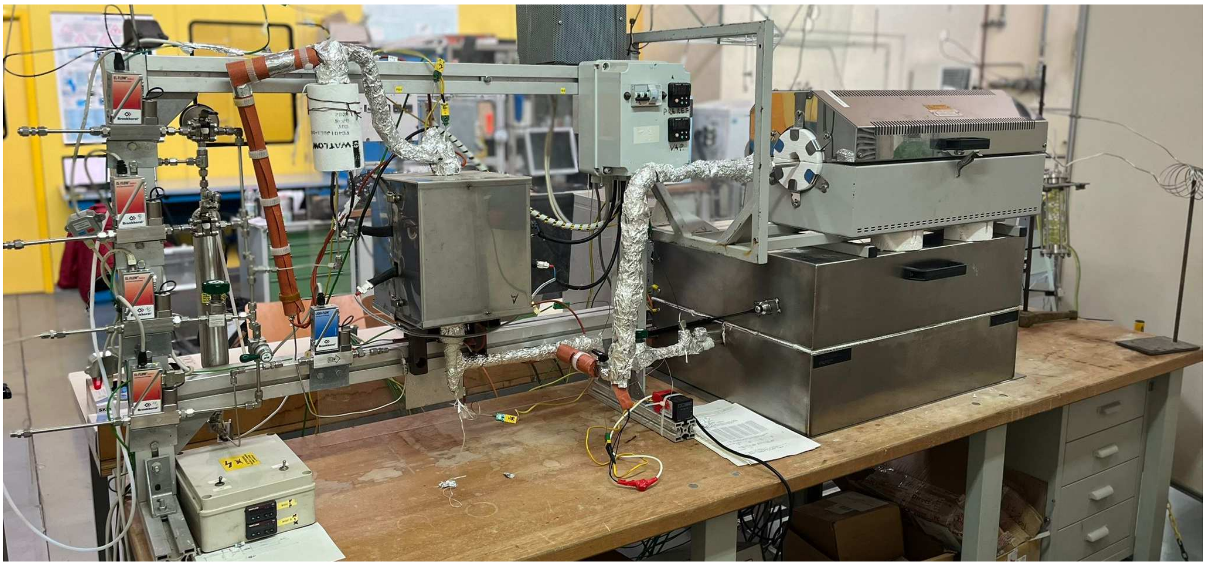

Figure 20-Experimental facility used to reproduce the thermochemical cycle. Located at ENEA, Casaccia.

Through this system it was possible to reproduce the whole cycle.

The gas required for reduction is introduced by the flowmeters placed at the inlet of the system (Figure 21). The water used for oxidation is vaporized inside a dedicated heating system.

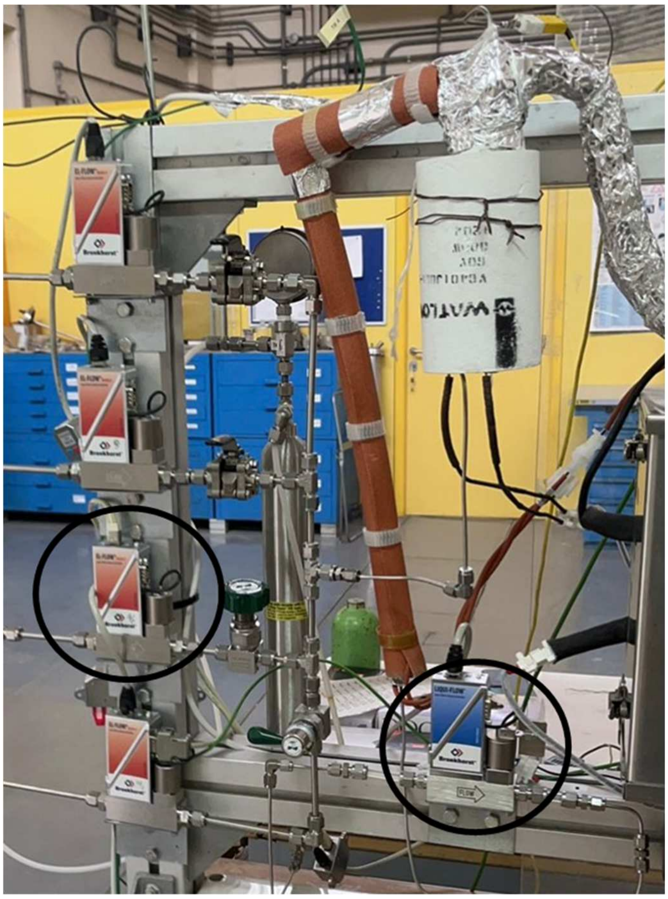

Figure 21-Flowmeters and flow controllers injection system; only nitrogen and water are injected in the system.

The gas stream (inert or inter plus steam) enters a heated stainless-steel reactor containing the perovskite powder. The reduction and water shift temperature were set according to the results of the preceding experimental campaign.

When oxidation is performed, the outlet gases from the reactor are sent to a condensation unit to remove the unreacted vapor from the gas stream.

Then, the gas stream, formed by a nitrogen carrier and hydrogen produced in the reaction, is directed into a gas chromatograph and, finally, expulsed directly in the atmosphere through a vent system.

This system is at TRL 4 level, with respect to the TGA trials, has the advantages to investigate the oxidation step at different steam pressures, up to 8 bar, and allows to use of higher number of powders (order of grams).

3 Thermodynamics and Kinetics of the redox reactions

3.1 Theoretical thermodynamics considerations

Starting from the reduction reaction, the standard reaction Gibbs free energy can be written from the formation standard free energies of reagents and products:

$$\Delta G_{reduction} = \sum \Delta G_{f,Products} - \sum \Delta G_{f,Reactants} \qquad \textit{Eq. 23}$$

Where:

$$\Delta G_{f,Products} = \Delta G°_{f,ABO_{3-\delta}} - \frac{\delta}{2} \Delta G_{f,O_2} \qquad \textit{Eq. 24}$$

$$\Delta G_{f,Reactants} = \Delta G°_{f,ABO_3} \qquad \textit{Eq. 25}$$

$$\Delta G_{f,ABO_{3-\delta}} = \Delta G°_{f,ABO_{3-\delta}} \qquad \textit{Eq. 26}$$

More in detail:

$$\Delta G_{f,O_2} = \Delta G^{\circ}_{f,O_2} + R \cdot T \cdot ln(p_{O_2}) \qquad \textit{Eq. 27}$$

$$\Delta G_{f,ABO_3} = \Delta G°_{f,ABO_3} \qquad \textit{Eq. 28}$$

$$\Delta G^{\circ}_{f,O_2} = 0 \qquad \textit{Eq. 29}$$

In which:

- $\Delta G°_{f,ABO_{3-\delta}}$ is the standard Gibbs Free energy of the reduced Perovskite.
- $\Delta G°_{f,ABO_3}$ is the standard Gibbs Free energy of the fully oxide Perovskite.
- $\Delta G^{\circ}_{f,O_2}$ is the standard Gibbs Free energy of the oxygen.
- p_{O_2} is the oxygen partial pressure.

The Gibbs free energy for the solids is equal to the standard value at each temperature, while, for what concerns oxygen, it depends on its partial pressure and temperature.

Eq. 29 can be arranged in this way:

$$\Delta G_{reduction} = \left(\Delta G°_{f,ABO_{3-\delta}} - \Delta G°_{f,ABO_3}\right) + \frac{\delta}{2} \cdot R \cdot T \cdot ln(p_{O_2}) \qquad \textit{Eq. 30}$$

$$\Delta G_{reduction} = \Delta G°_{Solid} + \frac{\delta}{2} \cdot R \cdot T \cdot ln(p_{O_2}) \qquad \textit{Eq. 31}$$

Where:

$$\Delta G°_{Solid} = \Delta G°_{f,ABO_{3-\delta}} - \Delta G°_{f,ABO_3} \qquad \textit{Eq. 32}$$

In equilibrium condition:

$$\Delta G_{reduction} = 0 \rightarrow \Delta G°_{Solid} = -\frac{\delta}{2} \cdot R \cdot T \cdot \ln\left(p_{O_2}\right) \qquad \textit{Eq. 33}$$

The same results can be obtained by evaluating the equilibrium constant, that, can be evaluated as [[71], [83], [84]]:

$$K_{red} = {p_{O_2}}^{\frac{\delta}{2}} \quad \text{Eq. 34}$$

Then, the standard Gibbs free energy of the reaction can be expressed, by its definition, as function of the equilibrium constant in this way:

$$\Delta G^{\circ}_{reduction} = -RTln(K_{red}) \quad \text{Eq. 35}$$

$$\Delta G^{\circ}_{reduction} = -RTln\left({p_{O_2}}^{\frac{\delta}{2}}\right) \rightarrow \Delta G^{\circ}_{reduction} = -\frac{\delta}{2}RTln\left(p_{O_2}\right) \quad \text{Eq. 36}$$

It follows that $\Delta G^{\circ}_{reduction}$ is equal to ΔG°_{Solid}.

Under thermodynamic control, in which oxygen partial pressure and temperature can be imposed, it is possible to measure the delta of the reaction through a TGA analysis and therefore obtain the trend of $\Delta G^{\circ}_{Solid}(T, \delta)$ as a function of these parameters.

With the available TGA equipment, it is possible to work with oxygen partial pressure down to 0.025 bar, in a temperature range from room temperature up to 1000°C. According to this, several tests were performed at fixed temperatures varying p_{O_2}. As a result, it was possible to derive an extrapolation of the $\Delta G^{\circ}_{Solid}(T, \delta)$ as function of delta at fixed temperature.

Considering the oxidation reaction with vapour, it is practically the sum of the inverse of the reduction process and water splitting, and its standard Gibbs free energy can be written as:

$$\Delta G^{\circ}_{Oxidation} = \sum \Delta G^{\circ}_{f,Products} - \sum \Delta G^{\circ}_{f,Reactants} \quad \text{Eq. 37}$$

Where:

$$\Delta G^{\circ}_{f,Products} = \Delta G^{\circ}_{f,ABO_3} - \delta \Delta G^{\circ}_{f,H_2} \quad \text{Eq. 38}$$

$$\Delta G^{\circ}_{f,Reactants} = \Delta G^{\circ}_{f,ABO_{3-\delta}} + \delta \Delta G^{\circ}_{f,H_2O} \quad \text{Eq. 39}$$

In which:

- $\Delta G_{f,ABO_3}^{\circ}(T, \delta)$ is the standard Gibbs Free energy of the oxidised Perovskite.
- $\Delta G_{f,ABO_{3-\delta}}^{\circ}(T, \delta)$ is the standard Gibbs Free energy of the reduced Perovskite.
- $\Delta G_{f,H_2}^{\circ}(T, \delta)$ is the standard Gibbs Free energy of oxygen.
- $\Delta G^{\circ}_{f,H_2O}(T)$ is the standard Gibbs Free energy of steam.
- δ is the oxygen released during the reduction reaction.

With $\Delta G^{\circ}_{Solid}(T, \delta)$ defined above as:

$$\Delta G^{\circ}_{Solid} = \left(\Delta G^{\circ}_{f,ABO_{3-\delta}} - \Delta G^{\circ}_{f,ABO_3}\right) \quad \text{Eq. 40}$$

Equation 1 becomes:

$$\Delta G^{\circ}{}_{Oxidation} = -\Delta G^{\circ}{}_{Solid} - \delta \Delta G^{\circ}{}_{f,H_2O} \qquad \textit{Eq. 41}$$

In general, a reaction becomes favourable under standard conditions when $\Delta G^{\circ}$is lower than zero. This condition can be expressed as:

$$\Delta G^{\circ}{}_{Oxidation} = 0 \; when - \Delta G^{\circ}{}_{Solid} - \delta_{minimum,reduction} \Delta G^{\circ}{}_{f,H_2O} = 0 \qquad \textit{Eq. 42}$$

$\Delta G^{\circ}{}_{Solid}$ as a function of delta can be extrapolated using the experimental data from the reduction reaction and can be used find the delta value for which is solved Eq. 42. Thus, the reduction temperature must be chosen to obtain a delta ($\delta_{minimum,reduction}$) that makes the oxidation reaction spontaneous at a certain temperature.

Therefore, several couple of temperatures, one for the reduction and one for oxidation, could be determined to carry out (at least from thermodynamics point of view) the water splitting cycle under 1000°C.

3.1.1 System for the direct measurement of the oxygen partial pressure

The system represented in Figure 22 and Figure 23 is composed by a stainless-steel shell in which the reactor is inserted, between the reactor and the shell there are two radiative heaters contained into an insulting material. The reactor is connected with nitrogen or air, which is provided by a flowmeter directly connected with the gas cylinders.

Figure 22-Experimental set-up for the measurement of the equilibrium oxygen pressure

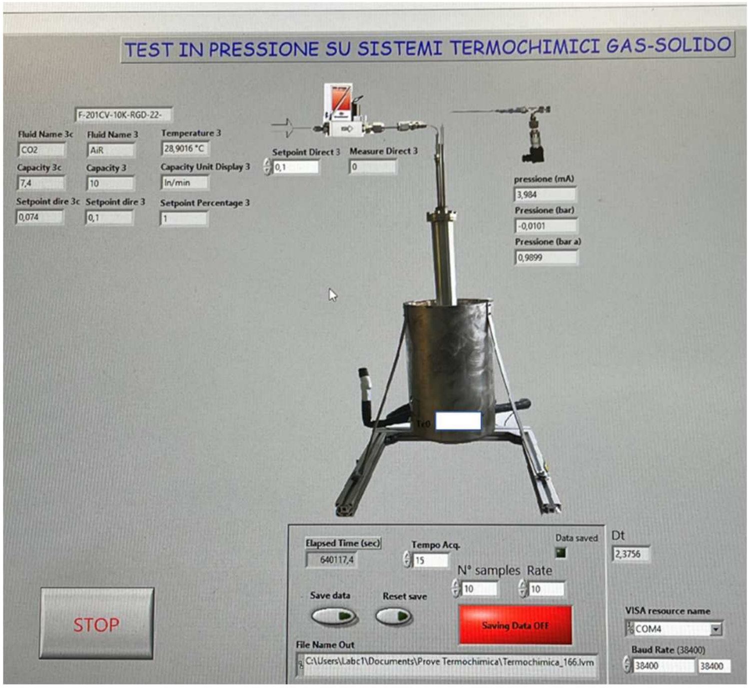
TEST IN PRESSIONE SU SISTEMI TERMOCHIMICI GAS-SOLIDO

F-201CV-10K-RGD-22-

Fluid Name 3c: CO2
Fluid Name 3: AiR
Temperature 3: 28,9016 °C
Capacity 3c: 7,4
Capacity 3: 10
Capacity Unit Display 3: ln/min
Setpoint dire 3c: 0,074
Setpoint dire 3: 0,1
Setpoint Percentage 3: 1
Setpoint Direct 3: 0,1
Measure Direct 3: 0
pressione (mA): 3,984
Pressione (bar): -0,0101
Pressione (bar a): 0,9899
Elapsed Time (sec): 640117,4
Tempo Acq.: 15
Dt: 2,3756
N° samples: 10
Rate: 10
File Name Out: C:\Users\Labc1\Documents\Prove Termochimica\Termochimica_166.lvm
VISA resource name: COM4
Baud Rate (38400): 38400 38400

Figure 23-Lab-view interface for the used experimental set-up

The aim is to measure in equilibrium condition the oxygen partial pressure as a function of temperature. During the endothermic reduction step, thermal energy creates vacancies in the perovskite structure with oxygen, until the equilibrium partial pressure is reached.

Beforehand, the empty reactor (blank test) is inertized with nitrogen, closed, and the total gas pressure is measured as a function of temperature. Then, the perovskite (about 14 g) is inserted, and the resulting pressure was determined at several isothermal values, in the range between 700°C and 900°C.

Realistically assuming an ideal behaviour for nitrogen and oxygen, the resulting equilibrium oxygen partial pressure can be calculated as following:

$$p_{O_2}(T_i) = p_{O_2+N_2}(T_i) - p_{blank}(T_i) \qquad \textit{Eq. 43}$$

Then, the perovskite is re-oxidized with air at 800°C for about one hour.

3.2 Reaction kinetics

Thermodynamics is not sufficient to completely characterize the redox reactions. Indeed, from the thermodynamics is possible to know if the reaction in specific conditions is spontaneous or not but it does not provide information on the time it takes to reach equilibrium. To know this kind of information, such as the rate of conversion or the reaction velocity also kinetics must be studied.

In this treatment, reaction velocities were determined by a model able to approximate the thermogram generated by the experimental tests in TGA. The first derivative of the thermogram represents the velocity of the reaction toward the equilibrium at each temperature or over a determined temperature ramp.

3.2.1 Kinetic models for solid reduction and oxidation

The reactions of a two-step thermochemical cycles are heterogeneous, in which a fluid reacts in contact with a solid transforming part of the latter in fluid or solid products. Such reactions can be described as:

$$A_{fluid} + bB_{solid} \rightarrow products$$

Following this methodology, the redox reactions are written as:

$$TR\text{: } \frac{2}{\delta}N_{2\,(g)} + \frac{2}{\delta}ABO_{3\ (s)} \rightarrow \frac{2}{\delta}N_{2\,(g)} + \frac{2}{\delta}ABO_{3-\delta\,(s)} + O_{2\,(g)} \qquad \textit{Eq. 44}$$

$$WS\text{: } \frac{1}{\delta}ABO_{3-\delta\ (s)} + H_2O_{(g)} \rightarrow + \frac{1}{\delta}ABO_{3\,(s)} + H_{2\,(g)} \qquad \textit{Eq. 45}$$

Approximating the particle size with a spherical shape, the Shrinking Core (SC) model can be used [85] . This model is based on the fact that the reactions occur firstly on the outer part of the particle, then, the reaction layer moves continuously toward the centre of the particle, leaving behind material and inert solid, the latter is called ash. The shrinkage of the unreacted core during the reaction is correctly explained by Figure 24.

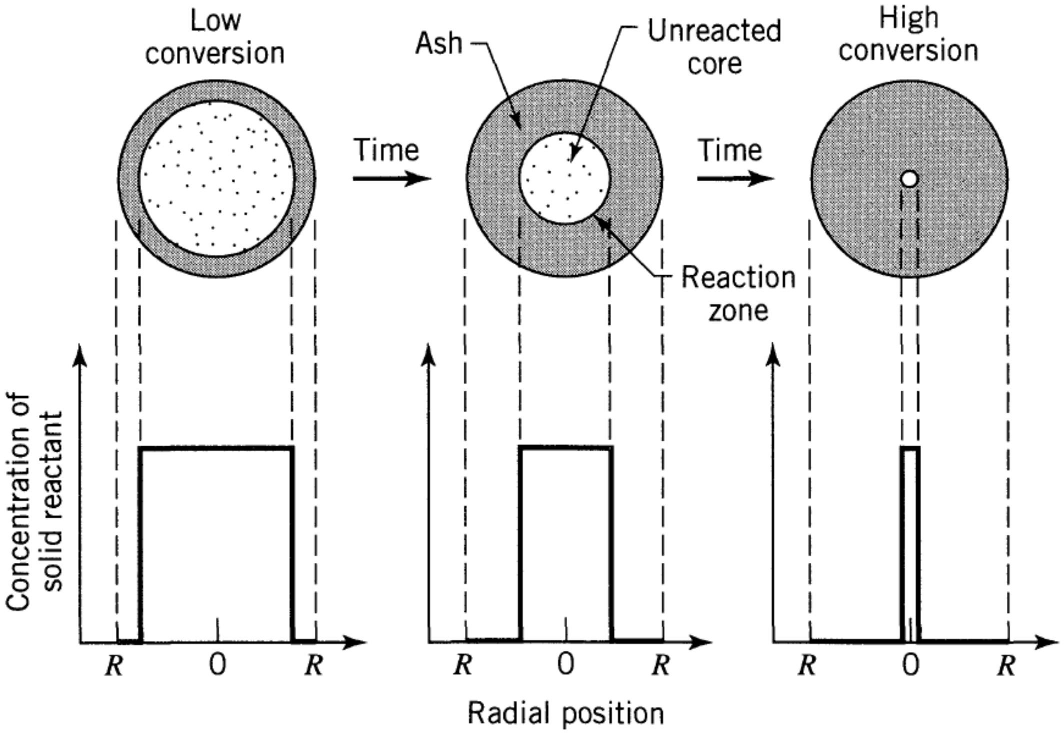

Figure 24-According to the SC-model, reaction proceeds at narrow front which moves into the soli particle. Reactant is completely converted as the front pass.

The SC model was developed by Yagi e Kunii(1955,1961). They identified five consecutive steps during the reaction:

- Step 1: Diffusion of the gaseous reactant A from the surface surrounding the particle to the solid surface.
- Step 2: Penetration and diffusion of A within the blanket of the ash to the surface of the unreacted core.
- Step 3: Heterogeneous reaction between gaseous A and solid B on the moving reaction surface
- Step 4: Diffusion of the gaseous products from the blanket of ash back to the external surface of the solid
- Step 5: Diffusion of gaseous products through the gas film back to the fluid or body

In some specific case some steps are not present, e.g., steps 4 and 5 would not exist if there are not gaseous products because they do not contribute directly to the resistance to reaction. More in general, the resistances of different steps vary between each other, in these cases the step with highest resistance is considered the rate-controlling step.

In first approximation diffusion problems and ash problems can be neglected, therefore under these hypothesis steps 3 is the rate- controlling step. Under chemical reaction control, the rate of the reaction is proportional to the surface of the unreacted core. Thus, based on unit surface of unreacted core, r_c, the rate of reaction for a single heterogeneous reaction is:

$$-\frac{1}{4\pi r_c^2}\frac{dN_B}{dt} = -\frac{b}{4\pi r_c^2}\frac{dN_A}{dt} = b\,k''\,C_{A_g} \qquad \textit{Eq. 46}$$

Where:

- $k"$ is the rate constant of the surface reaction.
- Nb can be written ad function of the shrinking radius and so:

Nb can be written ad function of the shrinking radius and so:

$$dN_B = \rho_B dV = \rho_B d\left(\frac{4}{3}\pi r_c^3\right) = 4\rho_B \pi r_c^2 \, dr_c \qquad \textit{Eq. 47}$$

Therefore:

$$-\frac{1}{4\pi r_c^2}\frac{dN_B}{dt} = -\frac{4\rho_B \pi r_c^2}{4\pi r_c^2}\frac{dr_c}{dt} = -\rho_B \frac{dr_c}{dt} = b\, k" \, C_{A_g} \qquad \textit{Eq. 48}$$

Solving this last equation is know the rate constant of the surface reaction. In this treatment the considered equations are slightly different. Indeed, it is not possible to evaluate the radius of the unreacted core during the reaction. For this reason, the kinetics reactions will refer to the conversion, that is function of the variation of the sample mass with time.

Conversion is expressed in different ways with respect to which reaction is considered.

The perovskite powders are analysed under different conditions:

- Redox reactions at constant temperatures.
- Redox reactions over temperature ramps with constant heating rate.

From the thermodynamic considerations described in chapter 5, it resulted that a suitable reduction step can only be performed under nitrogen, for this reason only decomposition with nitrogen was taken into account in the kinetic section.

Moreover, the kinetics equations vary with the considered reaction. The reduction reaction can be described by a zero-order model because the velocity does not depend on the gas concentration, therefore a reactant is consumed at the same velocity until the end of the reaction. A zero-order model with nitrogen is confirmed by the evaluation of the first derivative of the thermogram.

Manipulating the chemical reaction control equation:

$$-\rho \frac{dr_c}{dt} = b\, k_{red} \qquad \textit{Eq. 49}$$

And defining $\alpha_{reduction}$ as:

$$\alpha_{reduction} = 1 - \frac{r_c(t)}{R_{oxidated}} = 1 - \frac{n(t)}{N_i} = 1 - \frac{m(t)}{m_i} \qquad \textit{Eq. 50}$$

Therefore:

$$r_c = (1-\alpha) R_{oxidazed} \qquad \textit{Eq. 51}$$

Substituting Eq. 51 in Eq. 49is possible to define the reduction kinetic equation as function of the conversion:

$$\rho\, R_{oxidazed} \frac{d\alpha_{reduction}}{dt} = \; b\, k_{red} \qquad \textit{Eq. 52}$$

The oxidation reaction under air cannot be described by a zero-order model because the first derivative of the thermogram is not constant over time. Thus, its order is higher than zero and it is arbitrary chosen of first order model. According to the chosen model, the chemical reaction control becomes:

$$\rho \frac{dr_c}{dt} = b\, k_{ox} C_{O_2}(1 - \alpha_{oxidation}) \qquad \textit{Eq. 53}$$

As done for the reduction reaction the conversion can be defined as:

$$\alpha_{oxidation} = \frac{r_c(t)}{R_{reduced}} - 1 = \frac{n_c(t)}{n_{reduced}} - 1 = \frac{m\,(t)}{m_{reduced}} - 1 \qquad \textit{Eq. 54}$$

Therefore:

$$r_c = (1 + \alpha) R_{reduced} \qquad \textit{Eq. 55}$$

At the end:

$$\rho R_{reduced} \frac{d\alpha_{oxidation}}{dt} = b\, k'' C_{O_2}(1 - \alpha_{oxidation}) \qquad \textit{Eq. 56}$$

The calculations were carried out under the following assumptions:

- $R_{reduced} \approx R_{oxidazed} \approx R_{particle}$
- $R_{particle}$ was estimated by the SEM analysis, and it was assumed a spherical shape for the granules.
- The b parameter was calculated by the delta value obtained at 900°C (see paragraph x)
- The bulk density rho was estimated using the value of the CSM XRD reference pattern card.
- C_{O_2} was calculated from the ideal gas law and an average value was considered when the kinetics was evaluated over temperature ramps.

3.2.2 Isothermal approach

The material conversion (or conversion of matter) is described in chemical kinetics at a given, constantly maintained temperature *T*, at first. The temperature dependence of the material conversion is then established by an exponential relationship between temperature *T* and the corresponding reaction rate constant *k* namely as function *k* = *k*(*T*): where E_a is the molar activation energy, *A* the preexponential factor, and *R* the universal gas constant. This well-known relationship is the so-called Arrhenius equation in literature [86] .

The rate constant can be calculated solving the kinetic equation and since it does not depend on time because temperature is constant in time, it becomes:

$$TR\colon \rho\ \alpha\ R_{oxidazed} = \ b\ k_{red}t$$

$$WS\colon -\rho R_{reduced}\ln\left(1-\alpha_{oxidation}\right) \ = b\ k_{ox}C_{O_2}t$$

Now the Arrhenius parameters for each steps can be calculated starting from the equation:

$$k_{generic} = Aexp\left(-\frac{Ea}{RT}\right) \qquad \textit{Eq. 57}$$

Making the logarithm of both members:

$$\ln\left(k_{generic}\right) = \ln(A) - \frac{Ea}{RT} \qquad \textit{Eq. 58}$$

It is then possible to obtain with three different temperatures value a straight line in which:

$$Y = mX + q$$

More precisely:

- the intercept q is equal to $\ln(A)$.
- the slope m is equal to $-\frac{Ea}{RT}$.

and it is therefore possible to derive the values of the kinetic constants Ea and A.

3.2.3 Non-Isothermal approach

From a thermo-analytical point of view, the temperature is a function of time, meaning $\mathrm{T} = \mathrm{T(t)}$. Experimentally, this dependency in time is set by a constant linear heating rate $\beta = \frac{dT}{dt}$ [86]. Therefore, the rate constant for a non-isothermal evaluation cannot be directly calculated as done before because it varies continuously in time.

Mathematically, the integration of the rate constants is necessary, so that the kinetic equations become:

$$TR\colon \rho\ \alpha\ R_{oxidazed} = b\int_0^{t_{reduction}} k_{red}\ dt \qquad \textit{Eq. 59}$$

$$WS\colon -\rho R_{reduced}\ln\left(1-\alpha_{oxidation}\right) \ = C_{O_2}b\int_0^{t_{oxidation}} k_{ox}\ dt \qquad \textit{Eq. 60}$$

in which $t_{reduction}\ and\ t_{oxidation}$ represents respectively the time for complete the reduction step and for complete the oxidation step. Substituting the Arrhenius law:

$$TR\colon \rho\ \alpha\ R_{oxidazed} = b\int_0^{t_{reduction}} Aexp\left(-\frac{Ea}{RT(t)}\right) dt \qquad \textit{Eq. 61}$$

$$WS\colon -\rho R_{reduced}\ln\left(1-\alpha_{oxidation}\right) = C_{O_2} b\int_0^{t_{oxidation}} Aexp\left(-\frac{Ea}{RT(t)}\right)\, dt \qquad \textit{Eq. 62}$$

It is not possible directly solve those integrals; however, they can be approximated with the rectangular approximation, thus, substituting the integrals with a summation and explicit the time dependence of the temperature with time:

$$\int_0^t Aexp\left(-\frac{Ea}{RT(t)}\right)\, dt = \sum Aexp\left(-\frac{Ea}{R(T_{initial}+\beta t)}\right)\Delta t \qquad \textit{Eq. 63}$$

The Arrhenius parameters are calculated solving kinetic equation for three different heating rates or cooling rates: $\pm 5\frac{°C}{min}, \pm 10\frac{°C}{min}, and \pm 20\frac{°C}{min}$.

3.3 Energy transfer estimation for a planetary milling process

A simplified version for modelling the energy transfer mechanism is adopted. This is done to estimate the order of magnitude of the total energy transfer in a planetary milling process. Under the hypothesis the primary energy transfer event is collision the energy releases for each collision can be expressed as [87]:

$$\Delta E = K_a \frac{1}{2} m_b V_b^2 \qquad \textit{Eq. 64}$$

In which:

- K_a is a constant coefficient.
- m_b is the mass of the ball.
- V_b is the relative impact velocity.

K_a depends on the elasticity of the impact: for a perfect elastic collision the energy released is null ($K_a = 0$), whilst the energy transfer is total for perfect inelastic collision ($K_a = 1$). Obviously, the material used and the diameter of the ball itself will determine the mass of the ball. The relative impact velocity, finally, can be derived by the kinetic equation of a planetary milling[88], that is:

$$V_b = K_b \omega_p r_p \qquad \textit{Eq. 65}$$

In which:

- K_b is a constant coefficient, that mainly depends by the geometry of the mill.
- ω_p is the rotational speed of the mill.
- r_p is the useful radius of the mill, measured as the distance between the centre of the jar and the centre of the main disk [88].

If the number of balls (N_{balls}) in the jar is sufficiently low, it is possible to neglect the reciprocal hindering, thus the total collision frequency can be given by:

$$\nu_{total} = N_{balls} K_{\nu} \omega_p \qquad \textit{Eq. 66}$$

In which, $K_{\nu}$is another constant that depends mainly on the geometry of the mill.

The total energy released by the process can be estimated:

$$E_{tot} = \Delta E \ \nu_{total} \ t \qquad \textit{Eq. 67}$$

Where, t indicate the residential time of the sample material in the jar in operating condition.

4 Methods and materials

4.1 Material & Perovskite Preparation

This section is a detailed description of the perovskite sample preparation methods used in this work. The procedures are described for the preparation CSM 20 which was used as a benchmark to determine the best synthesis method. Then, the other perovskites were synthesised accordingly. High purity compounds supplied by Sigma-Aldrich were employed for all syntheses; a list of these materials with their identification CAS is given in Table 7.

Table 7-List of materials used for the synthesis.

Compound	Formula	CAS
Manganese carbonate	$MnCO_3$	598-62-9
Calcium Nitrate tetrahydrate	$Ca\ (NO_3)\ _2\text{-}4H_2O$	13477-34-4
Strontium Nitrate	$Sr\ (NO_3)_2$	10042-76-9
Manganese acetate tetrahydrate	$(CH3COO)_2Mn\text{-}4H_2O$	6156-78-1
Calcium carbonate	$CaCO_3$	471-34-1
Strontium carbonate	$SrCO_3$	1633-05-2
Lanthanum nitrate hexahydrate	$La\ (NO_3)_3 \cdot 6H_2O$	10277-43-7
Aluminium nitrate nonahydrate	$Al\ (NO_3)_3 \cdot 9H_2O$	7784-27-2
Iron Nitrate nonahydrate	$Fe\ (NO_3)\ _3\text{-}9H_2O$	7782-61-8

4.1.1 First synthesis route

The reactants were manganese carbonate, calcium nitrate and strontium nitrate. Firstly, they are weighed under stochiometric conditions and then mixed in a flask using deionised water plus isopropyl alcohol as solvents ($water: isopropyl\ alcohol\ 88: 12\ V/V$) . The mixture was stirred both manually and mechanically at room temperature, then the solvent was evaporated placing the flask over a hotplate. The obtained powder was dried by raising the temperature to 300-350°C (Figure 25). The time required to complete the process was approximately 3 hours.

Figure 25-Mechanical stirring and solvents evaporation process at 300/350°C

Then, the dry mixture was transferred into a quartz tube reactor and heated to 600°C, as shown in Figure 26, to decompose the nitrates. This process took a further 3 hours.

Figure 26- Tubular reactor used for makes dry and NOX free the mixture.

At that point, the obtained mixture was expected to be homogeneous, dry, and free of NOx. To produce the perovskite structure, a step followed at three different temperatures: 700°C, 850°C, 1000°C. The products (Figure 23) were evaluated by XRD analysis.

Figure 27- Sample preparation for a calcination process.

In Table 8 it is summarized the synthesis procedure with the first route.

Table 8- Route one: synthesis procedure.

	Step	Scope	Time
1	Preparation and weighting of the reactants	-	-
2	The reactants are dispersed in a flask of 200 ml.	-	-
3	Manual and Magnetic mixing of the components	Homogeneous mixing	-
4	The bottom part of the flask is heated up to 200°C in reduced mixing condition, using a warmed plate.	Evaporation of the water and isopropyl alcohol (dry mixture	~35 minutes
5	The temperature of the plate is raised up to 300/350°C.	Elimination of the NO_x (not detectable at this stage)	~150 minutes
6	The mixing result is transfer in a quartz tube.	Elimination of the NO_x (yellow gases)	-
7	The quartz tube is used in a reactor, that is heated up to 600°C.	-	~210 minutes
8	Calcination at 700/850/ 1000°C.	Elimination of all the volatile substances	~6 hours

4.1.2 Second synthesis route

With this method, the manganese carbonate is replaced by manganese acetate tetrahydrate. The solid reactants were manually mixed with deionised water and isopropyl $alcohol$ $(water: isopropyl\ \ alcohol\ 88:12\ \ V/V\ )$ inside a flask at room temperature, with the aim to dissolve the reactants in the solution. When the mixture was as homogeneous as possible, it was transferred to a Rotavapor system, in which the flask was immersed in a thermal oil, and then stirred at a temperature between 50°C and 150°C, as reported in Figure 28.

Figure 28- Mixture stirring in a Rotavapor system.

The time required to obtain a dry and homogeneous mixture was approximately 90 minutes. At that point, a solid portion of the mixture was extracted and analysed by TGA to determine the temperature for the exothermic reaction between air, nitrate, and acetate, which resulted at about 250°C Figure 29.

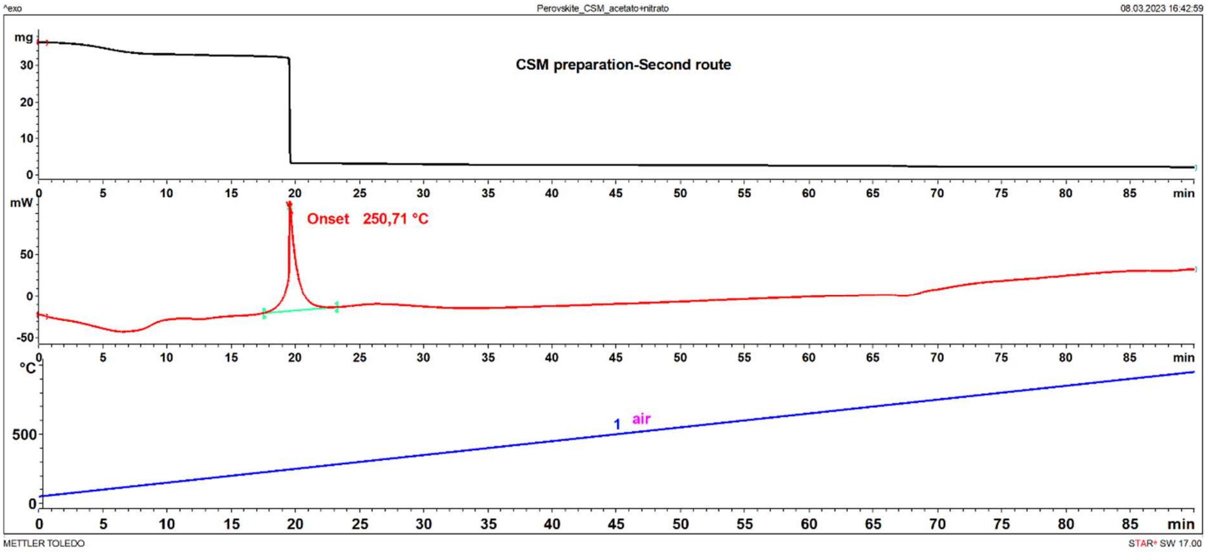

Figure 29- TGA/DTA analysis of the reaction between manganese acetate and calcium and strontium nitrates, used to synthesize CSM by the second route: the Figure shows, from top to bottom, the thermo-gravimetric pattern, the heat-flow and the temperature program used. The red line shows the reaction enthalpy measured by integrating the exothermic peak. Test carried out with a flow of 40 Nml/min of air (segment 1).

Then, the powder was reacted at that temperature inside a quartz tube (Figure 30), trapping the formed NOx with a NaOH solution.

Figure 30- Set-up for the reaction between manganese acetate and strontium and calcium nitrates. The powder is inserted within an alumina crucible wrapped with aluminium. The material is heated inside a quartz tube to trap downstream the produced nitrogen oxides (NO_x)

The obtained product was crushed several times inside a mortar, and then calcined at 700/800/900/1000 °C. In Table 9 is reported the synthesis procedure of the second route.

Table 9-Second route: synthesis procedure

	Step	Scope	Time
1	Preparation and weighting of the reactants	-	-
2	The reactants are dispersed in a balloon.	-	-
3	Mixing of the components at room temperature	Dissolve the reactants	-
4	Transfer to Rotavapor under chemical hood with silicone oil bath (thermal oil).	Homogeneous mixing	-
5	The temperature of the oil is raised up to 150°C, with a step of 50°C.	Solvents evaporations	∼2 hours
6	Determination of NOX development temperatures in TGA.	-	-
6	The mixing result is transfer in a quartz tube.	Elimination of the NO_x (yellow gases)	-
7	The quartz tube is used in a reactor, that is heated up to 400°C.	-	∼3 hours
8	Calcination at 700/800/900/1000°C.	Elimination of all the volatile substances	Depends on temperature

4.1.3 Third synthesis route

A stoichiometric mixture of calcium, strontium and manganese carbonates is prepared and suspended in acetone and stirred in a Rotavapor system. After three hours at room temperature, the temperature was raised to 85°C for promoting the complete evaporation of acetone. This process took over an hour. The dry mixture was then ground using high energy milling procedures. The resulting powders were crushed inside a mortar, and finally calcined at 1000°C. In Table 10 is summarized the synthesis procedure of the third route.

Table 10- Third route: synthesis procedure

	Step	Scope	Time
1	Preparation and weighting of the reactants	-	-
2	The reactants are dispersed with acetone in a balloon.	-	-
3	Mixing of the components at room temperature	-	3 hours
4	The temperature of the oil is raised up to 85°C	Solvent evaporation	90 minutes
5	Ball milling process	Powders activation	-
6	Calcination at 1000°C	-	6 hours

4.2 Methods and instrumentations

In this section is listed a description of each instrument and of all the methodologies employed.

4.2.1 High energy ball milling

Mechanochemistry is defined as a particular branch of chemistry that studies chemical reactions caused by mechanical energy. [89] The mechanical energy transferred to a system in fact produces a series of effects, of which the crushing of large objects into smaller objects is the most evident phenomenon. However, together with the crushing, less known phenomena occur, consisting of real chemical reactions: in a grinding process, a transfer of mechanical energy is achieved from the grinding bodies (balls, walls of the mill) to the system subjected to grinding. The transfers of this energy take place, in principle, through two mechanisms: friction and collision.

Mechanical activation of solids to promote solid-state reactions is a well-established process for the synthesis of compounds at temperatures near room temperature. [90]

Mechanochemical technology has already highlighted enormous possibilities in the field of metallic materials, a field in which industrial applications already exist. Figure 31 shows the trend in the number of publications between the 70s and 90s in the field of mechanical alloying. Other works are showing that mechanochemical processes can also be used successfully for the development and treatment of non-metallic materials such as ceramics and polymeric materials. It is a preparation methodology with a low environmental impact (for example it does not require the use of solvents), easily scalable and with great potential both in high-tech and medium-low tech sectors.

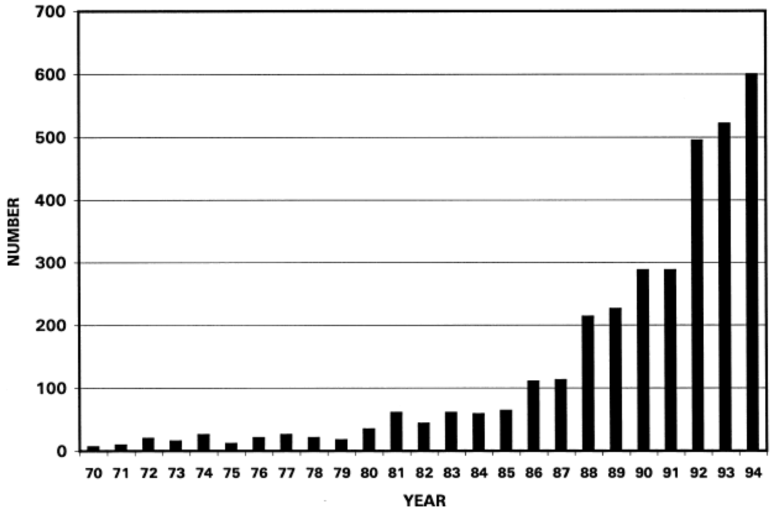

Figure 31- Growth rate of publication in mechanical alloying during 1970-1994

On industrial scale, INCO, a pioneer company in the production of alloys for Mechanical Alloying, has used two different types of mills, which base their operation on dynamic phenomena of friction: rolling and sliding of the balls (rolling/sliding) in a case, fall by gravity of the same in the other. The phenomena may or may not coexist and overlap depending on the equipment and the conditions of use. At laboratory level, equipment capable of processing modest quantities of powders and producing good results in a relatively short time are frequently used. Among these, the most used mills are those with vibration and in planetary mills. In the latter, the jar, containing the balls and the material to be processed, performs a double rotation. The first rotation is around its main axis of symmetry, while the second consists of an orbital rotation around an axis parallel to the first but placed at a given distance from it. The action of inertial forces is such as to throw the balls contained in the jar against the opposite wall. During its action the mill carries out a movement analogous to the motion of the earth around the sun, being the rotation of the jar around the centre of the plate where it is placed and around itself equivalent to that of the earth around the sun and around its own axis, as described in Figure 32.

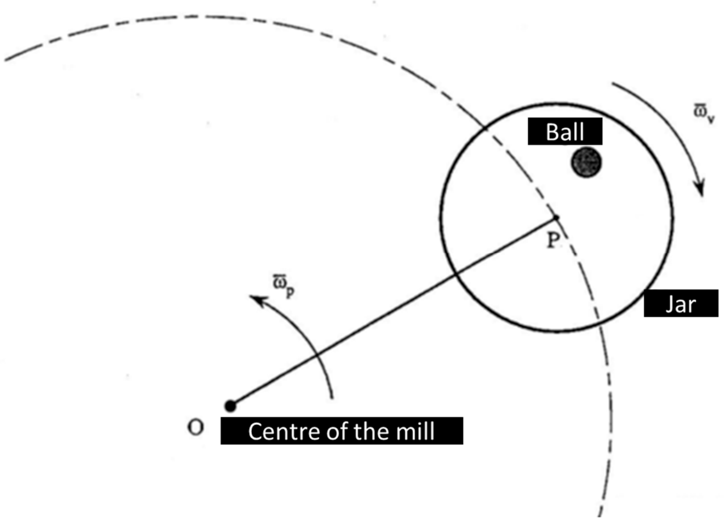

Figure 32- Movement of a planetary mill. The jar rotates on itself with speed $\overrightarrow{\omega_v}$ *around the axis passing through the point P, which rotates around the point O (centre of the mill) with speed* $\overrightarrow{\omega_p}$ *.*

The rotation ratio of a planetary mill is defined as:

$$R = \frac{\overrightarrow{\omega_v}}{\overrightarrow{\omega_p}} \qquad \text{Eq. 68}$$

Where $\overrightarrow{\omega_p}$ is the angular velocity of the plate to which the jars are attached and $\overrightarrow{\omega_v}$ is the angular velocity of the jar.

It is important to underline that $\overrightarrow{\omega_v}$ it is the absolute angular velocity of the jar, therefore measured with respect to an external reference system. R can assume negative or positive values depending on whether the direction of rotation of the jar is coupled with the plate.

A planetary mill used in this work and reported as an example is the *Fritsch Pulverisette 5.* This is a commercial device with vertical rotation axes, with a negative R value and the radius of the planetary orbit greater than the radius of the jar. The motion is achieved by exploiting a driving pulley with radius R_1, rotating with an angular speed ω_1, to which the driving moment M_m is applied, and a driven pulley with radius $R_2 > R_1$, rotating with an angular speed ω_P, to which the resistance moment M_u. The comminution of the material is due to the high-energy impact between balls and sample on the inner wall of the jars and between balls and the sample trapped between them. To obtain this, jars are positioned eccentrically on the main disk of the mill, and they rotate around their own axis, whilst the main disk rotates in the opposite direction. In Figure 33 a sketch of a grinding station equipped with 4 jars of a PBM is reported.

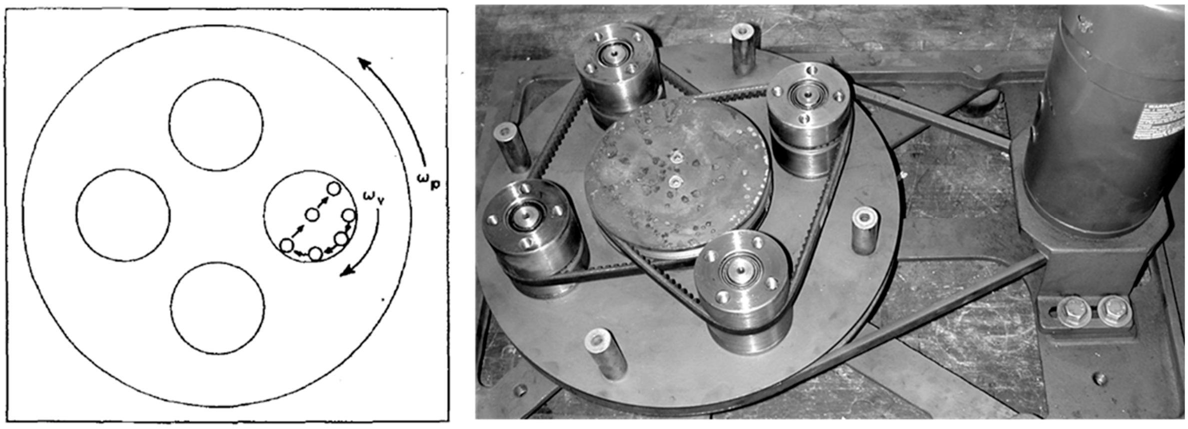

Figure 33-Scheme of Fritsch Pulverisette ball mill. Wp and Wv are the non-independent angular velocities of the ball mill plate and of the jar, respectively [88].

The superimposed centrifugal forces induce the movement of the balls that drives the milling process. Several parameters can be modified to tune the energy released during the process, such as jar and balls material, rotational speed of the disk, milling time and the number of balls, which corresponds to vary the weight ratio between sample mass and balls mass. Based on the chosen operational parameters the sample materials can be only comminute and mixed, chemically activated or synthesized to form another chemical structure.

In a laboratory planetary mill, the filling is usually modest, and the collision becomes the dominant event. For this reason, ENEA [91]has proposed and validated a kinematic model for the simulation of the movement of the ball essentially based on the collision, to obtain the fundamental equations for calculating the energy transferred by the ball per unit mass (ball-to-powder energy transfer) for each individual collision event. The proposed model agrees with the ones previously proposed by Maurice and Courtney [92] and Burgio [88].The ENEA model is briefly described in the paragraph 3.3.

For this work, two different planetary ball mills are used: PM 100, provided by Retsch and Pulverisette 5, provided by Fritsch. Both the mills are represented in Figure 34 and their main characteristics are summarized in Table 11.

Figure 34- The PM100 mill is shown on the left and the Pulverisette 5 mill on the right.

Table 11-Main characteristics of the used mills

	PM100 [93]	Pulverisette 5 [94]
Number of working stations	1	4
Grinding bowl sizes	12 ml / 25 ml / 50 ml / 80 ml / 125 ml / 250 ml / 500 ml	80, 250, 500 ml
Materials of the grinding tools	stainless steel, tungsten carbide, agate, sintered aluminium oxide, silicon nitride, zirconium oxide	agate, sintered corundum, silicon nitride, zirconium oxide, hardened stainless steel, hard metal tungsten carbide
Grinding ball diameter	5 - 40 mm	0.1 - 40 mm
Optimal for material type	Tough-fibrous, hard-brittle, medium-hard, fibrous, medium-hard/ fibrous, medium-hard, hard-brittle, soft-wet grinding	hard, medium-hard, soft, brittle, tough, moist
Grinding process	dry/wet	dry/wet
Grinding in inert gas	yes	yes
Rotational speed of main disk	100-650 rpm	50 - 400 rpm
Centrifugal acceleration (g = 9.81 m/s^2)	33.3 g	22 g
Sample quantity	Up to 220 ml	10-900 ml
Final fineness (depends on material)	<100 nm	< 1 µm

4.2.2 Microwave Plasma Atomic Emission Spectrometry (MP-AES)

Atomic spectroscopy refers to a series of analytical techniques used to determine the elemental composition of a sample by examining its electromagnetic spectrum or its mass spectrum.

Techniques that identify an analyte element from its electromagnetic spectrum include Flame Atomic Absorption Spectroscopy (FAAS), Inductively Coupled Plasma Optical Emission Spectroscopy (ICP-OES), and Microwave Plasma Atomic Emission Spectroscopy (MP- AES).

Microwave Plasma Atomic Emission Spectroscopy is an atomic emission technique that is based on the fact that an excited atom of a specific element emits light in a characteristic pattern of wavelengths (emission spectrum) as it returns to the ground state. Sources of atomic emission include microwave plasma (MP) and inductively coupled argon plasma (ICP), both of which are high-temperature sources, and thus excellent excitation sources for atomic emission spectroscopy. Nitrogen-fed microwave plasma reaches temperatures close to 5000 K. At these temperatures, atomic emission is strong, producing excellent limits of detection and a linear dynamic range for most elements.

The intensity of the light emitted is measured using optical detection at the characteristic wavelengths of the elements of interest.

Inside an MP-AES instrument (Figure 35), the microwave energy generated by an industrial magnetron is used to form a nitrogen plasma. Using a magnetic rather than an electric field for excitation generates a very robust plasma that can handle a wide range of sample types. An optimized microwave waveguide creates concentrated electromagnetic fields at the torch. Then an axial magnetic field and a radial electric field concentrate and contain the microwave energy to create a plasma. The operating principle is schematized in Figure 36.

Figure 35- Agilent 4210 MP-AES instrument present in ENEA-Casaccia laboratories.

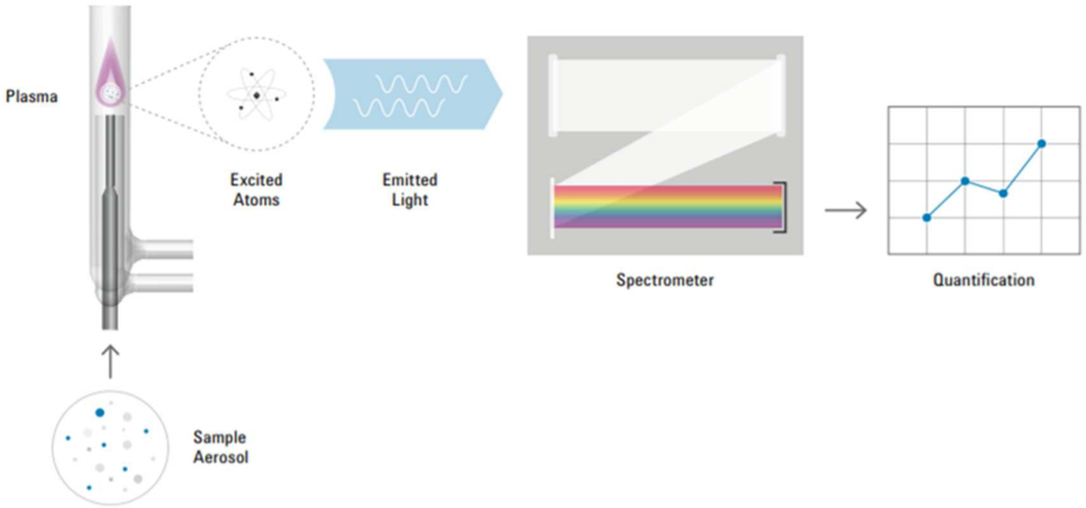

Figure 36- Operating principle of MP-AES.

During the sample introduction step, an aerosol is created from a liquid sample using a nebulizer and spray chamber. The aerosol is then introduced into the centre of the hot plasma, dries, decomposes, and is then atomized. The excited atoms emit light at characteristic wavelengths for each element returning to the lower energy states.

The plasma emission is directed towards a fast-scanning monochromator. The selected wavelength range is displayed on the high efficiency CCD detector. This detector simultaneously measures both the spectra and the background for optimal accuracy. MP-AES quantifies the concentration of an element in a sample by comparing its emission with that of the known concentrations of the element, plotted on a calibration curve. The result of the analysis is the concentration of the element in the sample.

The parts that make up the Nitrogen Plasma Atomic Emission Spectrometer are as follows:

- MP AES 4210.
- Air compressor / N_2 generator.
- Autosampler
- Computer.

The torch consists of an injector (internal part), Plasma (intermediate part) and bearing, which avoids direct contact of the plasma with the walls of the torch itself (external part) as shown in Figure 37:

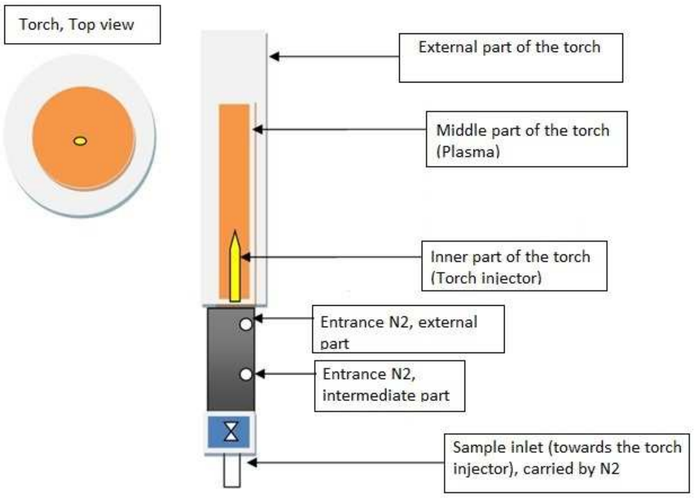

Figure 37-Description of the components of the torch.

The samples subjected to measurements with MP AES are prepared and dissolved in aqueous solution acidified with concentrated $\mathrm{HNO_3}$.After digesting the samples in nitric acid, hydrochloric acid or aqua regia, the resulting solution is filtered and then brought to volume. Before the sample was injected into the instrument, about 10-15ml of the solution was passed into syringe filters of about 0.22µm, to protect the nebulizer from easy obstructions due to its very small size (capillaries). To perform the measurement with Microwave Plasma Atomic Emission Spectroscopy (MP-AES) it is necessary to weigh 0.5g of salt sample and dissolve it in a 0.1l flask.

4.2.3 Differential Scanning Calorimetry- DSC

The Differential Scanning Calorimetry (Figure 38) or also known by the acronym DSC, is one of the most used techniques for thermal analysis. The basic principle consists of obtaining information on the material under test while it is being subjected to cycles of controlled heating and/or cooling. DSC monitors the difference in heat flow between the test sample and a reference, the latter remaining inert to temperature changes, while both are bound to the same heat treatment. The differential measurement of the system is extremely important because the resulting signal can be studied independently of thermal effects external to the system.

Figure 38-Mettler Toledo DSC instrument present in ENEA-Casaccia laboratories.

The instrument is prepared by placing on the housings two identical pans chosen to withstand the test temperatures without interacting with the sample under examination. One of the two pans will remain empty because it will serve as a reference for differential measurement. The DSC software allows to set the temperature program and the flow of the carrier gas (N_2, air). The heat transferred from the furnace heats both the sample and the reference in the same way; a control circuit compares the mean value between the temperatures detected on the sample and on the reference with the one selected by the temperature controller. Any temperature variation is due to phenomena that arise in the material being analysed: an exothermic reaction will raise the temperature of the sample while an endothermic will do the opposite.

The temperature difference is proportional to the sample adsorbed or released heat. The sample can be in liquid form, solid, powder, films, or granules and in small quantities (20-70 mg, depending on the pan used) but should be well distributed in the sample holder. The weight must be determined using a balance presenting at least an accuracy to the tenth of milligram. In case of hygroscopic substances, it is important to determine the weight of the dry material. The most feasible way is to weigh the sample and the holder (pan plus lid) together and dry them inside the instrument, under a water-free gas atmosphere, by heating up at 250 °C (10 °C/min) and keeping that temperature for 30 min. Finally, the holder plus the sample is weighed again, repositioned in the calorimeter, and the DSC measurement program (always under dry atmosphere) is run.

During the experiments a system of thermocouples collects the temperature data and sends it to specific software, which generates the DC output. The differential heat flow is directly proportional to the temperature difference between the output signals from the thermocouples. The DSC diagrams are graphs in which the differential speed of heating (in mW) is shown as a function of temperature or time of reaction. After choosing an adequate base line, the area under the curve is the total heat generated during the process.

4.2.3.1 MELTING POINTS and latent heat MEASUREMENT: Description of the method

Before starting the measurements, calibration of the DSC must be performed by placing samples of indium, zinc, and tin (whose initial solidification and liquefaction, and latent heats are known from literature) in the pans.

After the instrument has been calibrated, or calibration has been verified, 20-30 mg of the sample is placed inside a 100µl aluminium crucible (pan) and the lid is sealed. In case of mixtures presenting a very low enthalpy of phase change (such as, for instance, ternaries/quaternaries containing calcium nitrate) at least 100 mg must be used. As reference, an empty crucible (100µl of aluminium with lid) is used. The measurement is carried out using a 10 K/min ramp, there is no need for a blank curve.

Onset (liquidus and solidus) phase change temperatures are determined using the instrument software (see example below) or by determining a criterion to detect the phase change onset.

Latent heat is calculated by integrating the endothermic (liquefaction) or exothermic (solidification) peaks. The effect of specific heat change between the two phases is well compensated by integrating from the baseline just before the peak to the baseline just after the transition.

Provided the DSC is properly calibrated, the method leads to little measurement errors, which can be estimated, by statistical analysis, as 3% for a single measurement.

4.2.3.2 SPECIFIC HEAT MEASUREMENT: Description of the method

It is possible to measure heat capacity values of synthesized perovskites with the use of a known heat capacity substance as a reference, such as sapphire ($Cp_z \approx 1 \div 1.1 \, J \cdot g^{-1} \cdot K^{-1}$) as in the following:

$$W_z = Cp_z \cdot m_z \cdot \beta \cdot \Delta T \qquad \textit{Eq. 69}$$

$$W_{Perovskite} = Cp_{Perovskite} \cdot m_{Perovskite} \cdot \beta \cdot \Delta T \qquad \textit{Eq. 70}$$

where W is the absorbed power, Cp is the heat capacity, β is the temperature ramp with the corresponding ΔT, m is the weight. From the ratio between the two equations, it is possible to obtain:

$$\frac{W_z}{W_{Perovskite}} = \frac{Cp_z \cdot m_z}{Cp_{Perovskite} \cdot m_{Perovskite}} \qquad \textit{Eq. 71}$$

and the specific heat of the salt:

$$Cp_{Perovskite} = \frac{Cp_z \cdot m_z \cdot W_{Perovskite}}{m_{Perovskite} \cdot W_z} \qquad \textit{Eq. 72}$$

For this measurement a modulated temperature ramp is used, as reported In Figure 39.

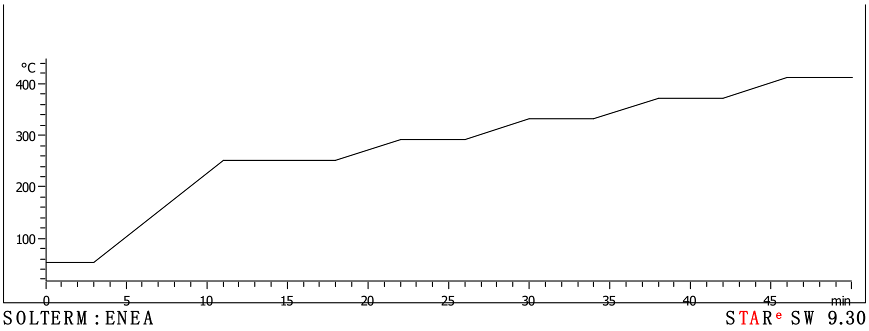

Figure 39-Temperature ramp example

After calibrating the instrument, two pans are placed on the two DSC zones. To better evaluate the baseline, a modulation like method is preferred in which a series of isothermal (typically 4-5 minutes) and temperature ramp (typically 10 K/min for 4 -5 minutes) steps are alternatively set. The absorbed heat can be measured by the height or the area of the obtained rectangular like peaks. The weight of the sample must be around 20 mg, and of sapphire 20 mg. Crucibles (pans) are of aluminium and with 40µl of capacity.

This is the standard DSC method for this instrument, and it is divided in three distinct phases. The pan used as a reference has been left empty during the whole measurement range and does not have the lid, to increase the temperature difference between two pans, and, consequently, improve the reproducibility of the blank curve, while the other one was filled in each step.

- **Blank:** controlled heating is carried out on both empty pans as calibration.

- **Sapphire:** controlled heating is carried out on both pans; the reference pan remains empty while in the other one is inserted 2 known weight sapphire disks (about 40 mg), necessary for the comparison with the salt.

- **Sample:** controlled heating is carried out on both pans; the reference pan remains empty while in the other one is inserted a known amount (approximately 40 mg, measured it on a precision balance) of the mixture of salt which is then sealed.

This method is simple to operate and takes around 3 hours per sample. By performing a statistical analysis, precision can be estimated by measuring the data dispersion over 5 samplings and measurements, and by repeating this method 5 times with different mixtures, nitrites, and nitrates. Using a Gaussian error distribution, a mean value with estimated error of 10% can be obtained in a confidence range of 90%. This can be considered a conservative averaging error if five different samplings are performed. Increasing the sampling figure, the precision of the average value will decrease inversely to the square root of the sampling number, but, evidently, measurement time will increase. For the determination of the specific heat of the perovskites, a "Mettler Toledo DSC" is used.

The instrument, at the ENEA laboratories, is equipped with a silver oven capable of reaching 700 ° C, in the bottom of which it is placed a ceramic coating sensor. This sensor protects from contamination, connected to a system of 56 gold thermocouples to have a very precise measurement and to compensate possible temperature gradient. Such a setup ensures flat baselines and reproducible results with a theoretical error less than $0.04\ \mu W$. The ceramic coating houses for two pans ($Aluminium\ 40\ ul$) covered by perforated lids (to allow the release of any gases).

The tests were carried out in air atmosphere and natural cooling. The instrument interacts with a computer using "Star Evaluation" software.

4.2.4 Thermo-Gravimetric Analysis – TGA

Thermo-gravimetric Analysis (TGA) is a procedure that provides information about physical phenomena, such as phase transitions, absorption, and desorption, as well as chemical phenomena including thermal decomposition and solid-gas reactions. This analysis consists in a mass of a substance which is monitored as a function of temperature or time while the sample specimen is subjected to an established temperature program in a controlled atmosphere. Moreover, TGA provides the possibility to investigate the chemical and physical calorimetric phenomena.

The instrument present at the laboratory of the ENEA Casaccia to perform calorimetric analysis is TGA/DSC 1 from METTLER TOLEDO (Figure 40).

The TGA/DSC 1 is a highly sensitive measuring instrument for thermo-gravimetric analysis (TGA). It includes a high-precision METTLER TOLEDO balance to measure the weight signal. Thanks to the design of the thermal sensors incorporated in the measuring cell, the TGA/DSC 1 also provides the possibility for differential scanning calorimetry (DSC).

This instrument consists of four components, that are a thermal scale, an oven, a purge gas system that ensures an inert or reactive environment and a computer to control the instrument. Once the heat program has been assigned and the pan (alumina or aluminium crucible, chemically inert materials against the substance under investigation) with the sample inserted in the instrument, the heat transferred from the furnace heats the sample, the computer records the behaviour over time and constantly monitors the weight of the crucible containing the sample. From this analysis it is possible to obtain several information regarding the material investigated, such as latent heat and thermal stability.

The instrument is equipped with a horizontal furnace characterized by a cylindrical section, and the heating elements are kanthal plates that are extend all along its length. Near the walls of the tubular furnace there are thermocouples to control the temperature. Inside the furnace, in a coaxial position, there is a sensor of material ceramic, which has also the function of support for the plate above which the crucible is positioned with the sample to be analysed.

Figure 40- Mettler Toledo TGAinstrument present in ENEA-Casaccia laboratories.

The TGA sensor is composed by the plate, the bar of ceramic material and a mechanism of coupling inside the instrument. The other part of the support rod enters a cavity inside the instrument and connects the sensor to the scale mechanism.
A R type thermocouple is positioned directly under the plate, consisting of a platinum-rhodium disk, to ensure that the temperature is measured in an area very close to the crucible.

4.2.5 X-Ray Diffraction (XRD)

X-ray powder diffraction (XRD) is a rapid analytical technique primarily used for phase identification of a crystalline material and to provide information on unit cell dimensions.
X-ray diffractometry (XRD) comes used to determine the crystalline phases contained in the minerals. In addition, it is possible the characterization, investigations, and identification of changes in materials due to degradation.
The analyzed material is finely ground, homogenized, and average bulk composition is determined. In a bi-dimensional lattice structure, each row acts as a reflecting plane by on-phase scattering of the incident radiation. X-ray diffraction is based on constructive interference of monochromatic X-rays and a crystalline sample. These X-rays are generated by a cathode ray tube, filtered to produce monochromatic radiation, with λ wavelength, collimated to concentrate, and directed toward the sample (Figure 41).

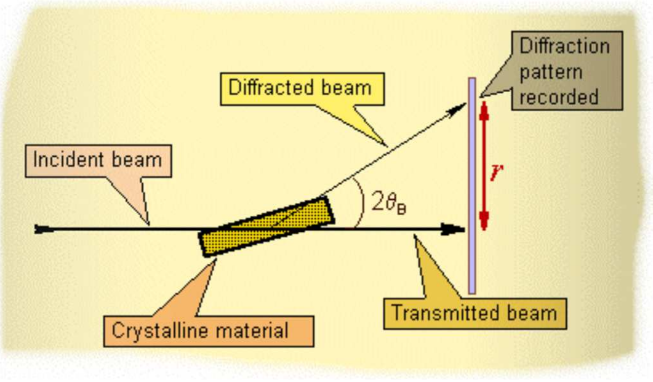

Figure 41-The atomic planes of a crystal cause an incident beam of X-rays to interface with one another as they leave the crystal. The phenomenon is called X-ray diffraction.

The interaction of the incident rays with the sample produces constructive interference (and a diffracted ray) when conditions satisfy Bragg's Law (Figure 42):

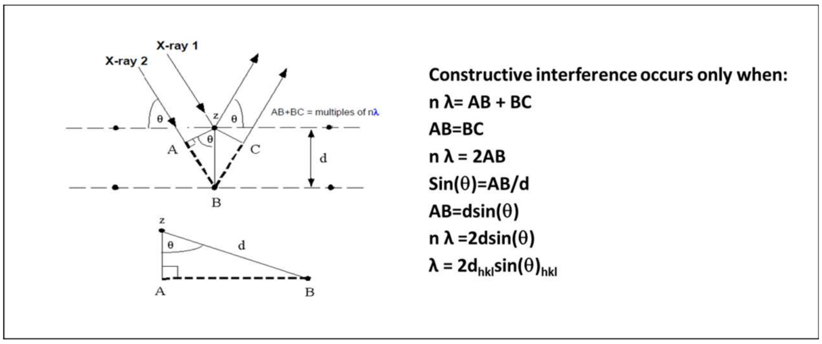

Figure 42- Geometric demonstration of the Bragg's Law.

This law relates the wavelength of electromagnetic radiation to the diffraction angle and the lattice spacing in a crystalline sample. The diffracted X-rays are then detected, processed, and counted. By scanning the sample through a range of 2θ angles, all possible diffraction directions of the lattice should be attained due to the random orientation of the powdered material. Conversion of the diffraction peaks to d-spacings allows identification of the sample because each one has a set of unique d-spacings. Typically, this is achieved by comparison of d-spacings with standard reference patterns.

Although Bragg's law was proposed to explain the interference pattern of X-rays scattered by crystals, diffraction can be used to study the structure of all states of matter with any beam, e.g., ions, electrons, neutrons, and protons, with a wavelength like the distance between the atomic or molecular structures of interest. To define the crystalline planes, the so called "Miller indices, hkl" are used. They are related to the reciprocal of the axial intercepts, considering an arbitrary origin of the axial system. The Figure below shows, as an example, the Miller indices for structure (Figure 43):

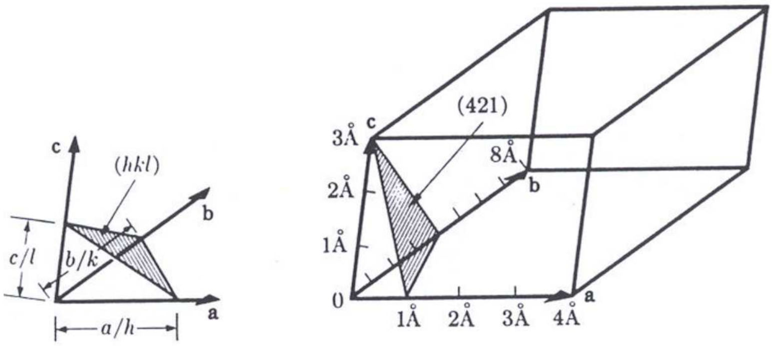

Figure 43-Miller indices-the reciprocals of the fractional intercepts which the plane makes with crystallographic axes.

X-ray diffractometers consist of three basic elements: a X-ray tube, a sample holder, and an X-ray detector. The instrument used in that study, X-ray Diffractometer (XRD 3000 Italstructure, curved Position Sensitive Detector from INEL) equipped with a Fe Ka1 radiation, (Department of Chemical Science and Technologies University of Rome Tor Vergata)

4.2.6 Scanning Electron Microscope (SEM)

Scanning electron microscope (SEM) consists of an instrument through which it is possible to conduct a non-destructive investigation thanks to the interaction between an electron beam and the sample, object of examination. It allows to obtain morphological and structural information, and, due to the presence of an X-ray spectrometer, also important information related to the chemical nature of the sample are analyzed. Scanning Electron Microscopy (SEM) magnifies a specific sample region using a high energy focused beam of electrons. The sample is under vacuum to ensure the electron beam stays focused and does not interact with particles in the air. When the beam of electrons hits the sample, it causes secondary electrons to be released from the sample which are detected to provide an image based off the topography of the surface. The two detectors most used include the Secondary Electron Detector (SED) and the Backscattered Electron (BSE) Detector. The electrons interact with the detector to create an image. The sample region evaluated with SEM Analysis can also be analyzed to determine the specific elements that comprise the sample region by utilizing Energy Dispersion Spectroscopy (EDX).
X-rays are also released from the surface of the sample that carry a unique energy signature that are specific to elements found in the sample. These X-rays are detected with the EDX detector to give elemental information about the sample. EDX provides data about the chemical composition of the sample and provides additional data about the features that are observed in the SEM micrographs. This combined technique is referred to as SEM-EDX or SEM-EDX Analysis. However, to perform a SEM analysis it is necessary to use a scanning electron microscope that is a microscope that uses the electrons instead of the light to form the sample image. Compared to optical microscopes, the SEM has several advantages and allows to obtain images with very high resolution and magnifications from 10 to 200.000 times. In Figure 44 the SEM scheme is represented.

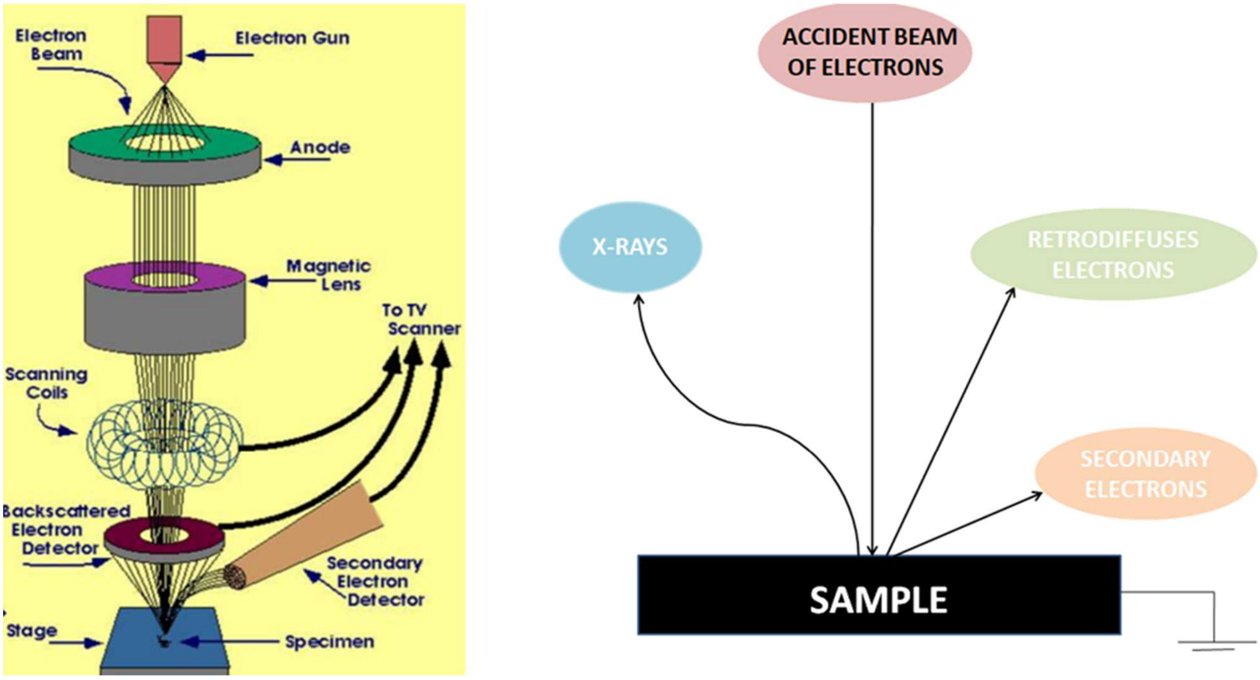

Figure 44-Scanning Electron Microscope (SEM) scheme. Operating principle of Scanning Electron Microscope technique.

To obtain good images it is advisable that the sample, which is bombarded by electrons, then from charged particles, if it is not already metallic, is metalized, or covered with a thin metallic layer (usually gold or graphite). In this way it is prevented the accumulation of charge on the sample (disturbed image). The electron source (or electron gun), that is a heated filament, produces an electron beam which, accelerated by an electric field and focused by a series of electromagnetic "lenses", reaches the sample. It should be noted that all the apparatus is under vacuum. When the electron beam hits the sample, different types of phenomena can take place (Figure 45):

Figure 45- TESCAN VEGAN SEM equipped with a EDX.

- *Secondary electrons:*
  when the electrons of the primary beam not reflected lose their energy transferring it to the electrons of the solid, part of the latter will escape to the outside; the signal does not depend on Z; the emission comes from 1-10 nm and **gives exclusively morphological information**.
- *Backscattered electrons:*
  when part of the incident electrons is reflected but keeps the same energy of the initial beam. The signal gets more intense as the atomic number Z increases; the emission comes from about 0.1-1 µm of depth from the surface and **gives mainly information of composition, as well as morphological**.
- *X-ray:*
  an electron of the primary beam can interact with the atomic structure of the sample ionizing it and obliterating an electron from the innermost orbitals, the structure as well excited it relaxes returning to its fundamental state through the emission of a photon X; the signal comes from very high depths (1-10 µm) and **gives information regarding the sample composition**.

The SEM image is obtained using secondary and / or backscattered electron, that convert and transmit these signals to a TV screen. With this technology it is possible to also perform the X

fluorescence analysis, thus the elemental analysis of the sample, using an X-ray detector. With the SEM-EDX technology it is possible to obtain very enlarged and detailed images of the sample (topographic and morphological analysis) and at the same time the elemental analysis of the sample itself. Moreover, it is possible to perform the mappings (scans) of the elements present in the sample. In practice, images obtained show the distribution of the different elements on the entire analysed surface.
The instrument used in this work is a TESCAN VEGAN equipped with a EDX (Department of Chemical Science and Technologies University of Rome Tor Vergata)

4.2.7 Gas Chromatograph– Thermal Conductivity Detector (GC-TCD)

A micro gas chromatograph was placed downstream the experimental set-up shown above (Figure 20 and Figure 21)to control in real time, the permanent gases (non-condensable gases) production.

In this work, a Varian Cp 4900 Micro GC, represented in Figure 46, was used; this instrument can be equipped with one to four independent column channels each consisting of an Electronic Gas Control (EGC) injector, a column, and a detector. The device has two columns working in parallel: a molecular sieve capillary column (able to separate most permanent gases with low molecular weights such as oxygen, nitrogen, hydrogen, carbon monoxide and methane) and a Poraplot like column that provides the separation of methane from the composite air peak and separate carbon dioxide from methane and C2 hydrocarbons [95].

Each GC channel is equipped with a Thermal Conductivity Detector (TCD) that consists of an electrically heated filament in a temperature-controlled cell. The Micro GC is connected to a carrier gas line, and the instrument used in this work is configured to use Argon.

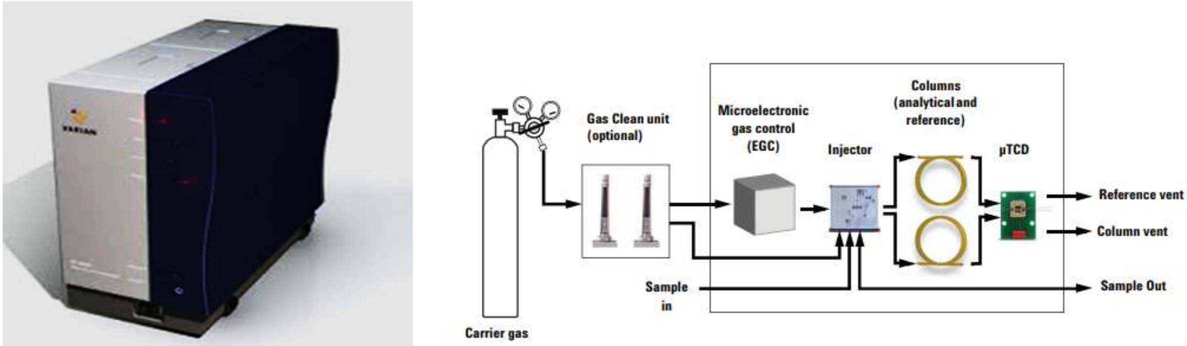

Figure 46-Varian Cp 4900 Micro GC (left) and its schematic representation.

4.2.8 Software

MATLAB R2022b software is used to developed codes require to solve the kinetics of the redox reactions. This software is chosen for its high calculating capacity.

5 Results and discussion

5.1 Perovskites Synthesis and Characterization

In this section, the crystal structure of the CSM 20 for each route is firstly comprehensively analysed by XRD technique; given the evaluation of the XRD patterns it was possible identify and select the best synthesis method to be used to synthetize the other selected perovskites. In addition, the surface morphology of all the synthesized perovskites was evaluated using SEM techniques.

5.1.1 First route

In Figure 47, Figure 48, Figure 49 and Figure 50 the XRD analysis of the sample material synthesized through the route one and calcinated at different temperatures are reported.

The calcination process was performed raising the temperature from room temperature to the calcination temperatures, that in this case are 700, 850 and 1000°C, with a heating rate of 5°C/min, and then maintained for 2 hours.

In each analysis the Reference XRD pattern of the perovskite (50-1747) is not the only one reported; in fact, a series of weak and strong peaks are present identifying also other crystallin compounds contained in the sample material.

Increasing the calcination temperature improves the quality of the results by reducing the peak intensity of the other crystal structures. However, even if the calcination temperature is increased to 1000°C, the presence of second phases is still too high.

In addition, the calcination time of perovskite can be increased improving the elimination of the remaining volatiles due to possible kinetic. Figure 48 shows the XRD analysis of the sample of material calcined at 850°C and kept at this temperature for 6 hours, four hours longer than the one reported in Figure 47.

The results are similar to those obtained by increasing the calcination temperature, leading to the conclusion that raising this parameter appears to be better than increasing the calcination time.

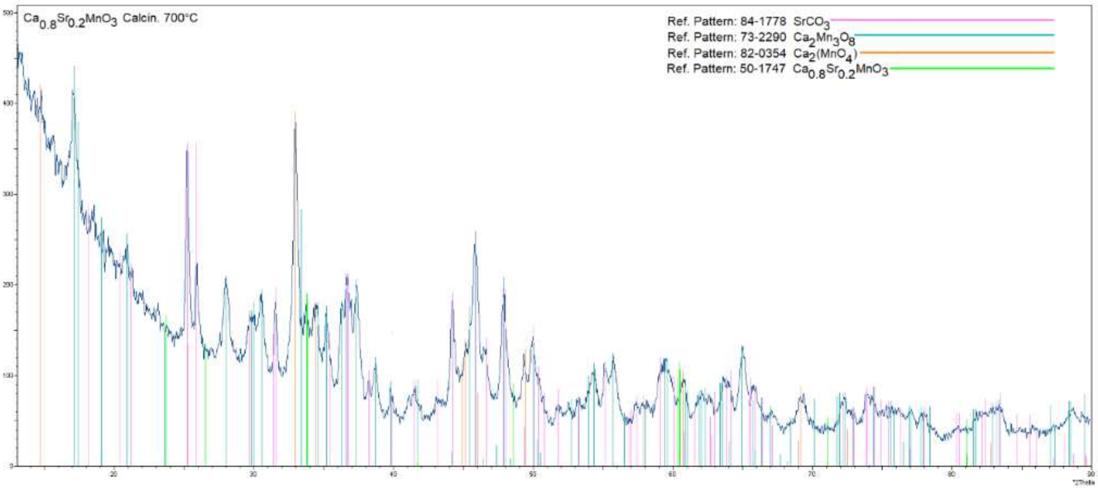

Figure 47- XRD analysis- First route: CSM calcinated for 2h at 700°C.

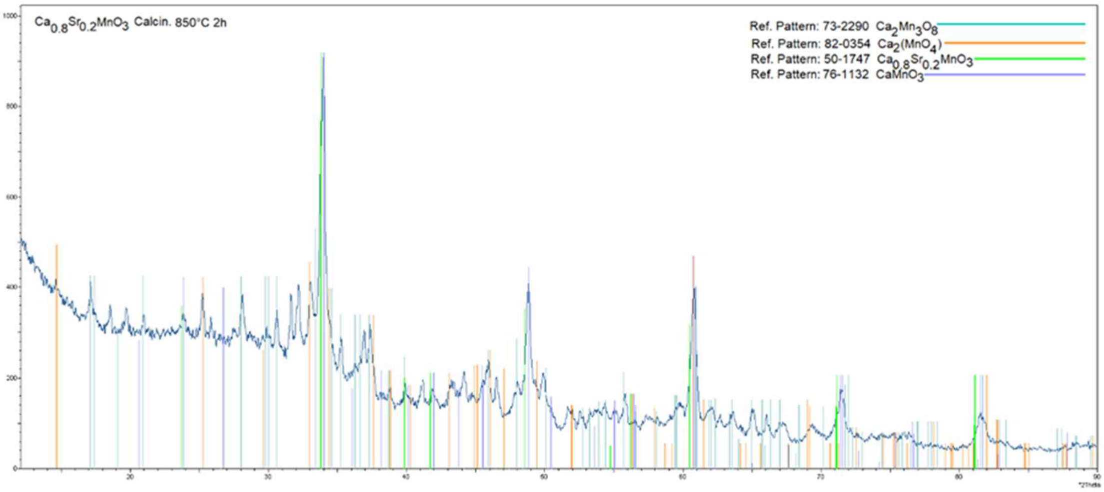

Figure 48- XRD analysis- First route: CSM calcinated for 2h at 850°C.

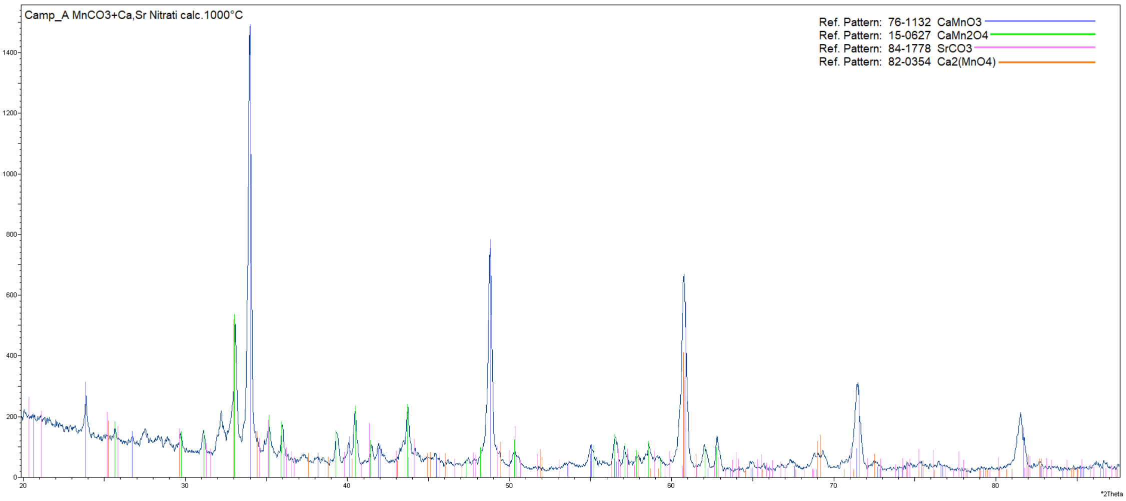

Figure 49- XRD analysis- First route: CSM calcinated for 2h at 1000°C.

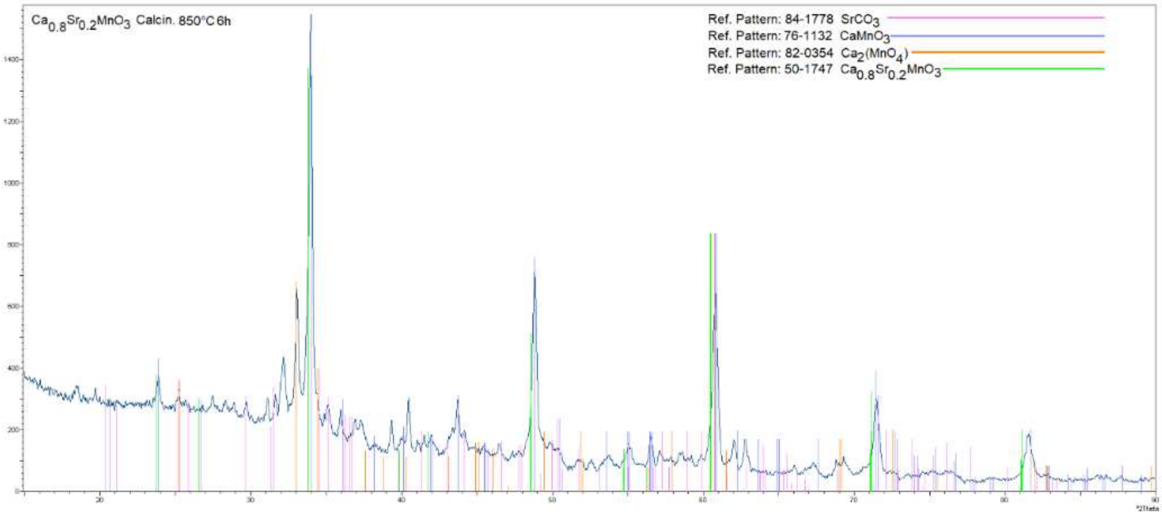

Figure 50- XRD analysis- First route: CSM calcinated for 6h at 850°C.

5.1.2 Second route

Figure 51 shows the XRD patterns after each step of the synthesis, following the evolution of the crystal structures as the synthesis proceeds. Until calcination at 900°C, the XRD patterns are scarcely affected by the process, as confirmed by the similarity of the peaks present in each diffractogram. However, as shown in Figure 52, the XRD pattern of the perovskite calcined at 900°C is present together with other peaks, meaning that there are too many impurities to take the synthesis for granted.

By increasing the calcination temperature to 1000°C (Figure 53) the result is the same, the impurities are reduced but not enough to make the result acceptable. All considered, it is clear that the calcination temperature needs to be high enough to form the perovskite structure and, at the same time, to avoid the problem of sintering that can occur at too greater temperatures; therefore, only one calcination temperature of 1000°C is used for the third route. In addition, also the calcination time at maximum temperature is increased from 2 hours to 3 hours to further improve the process.

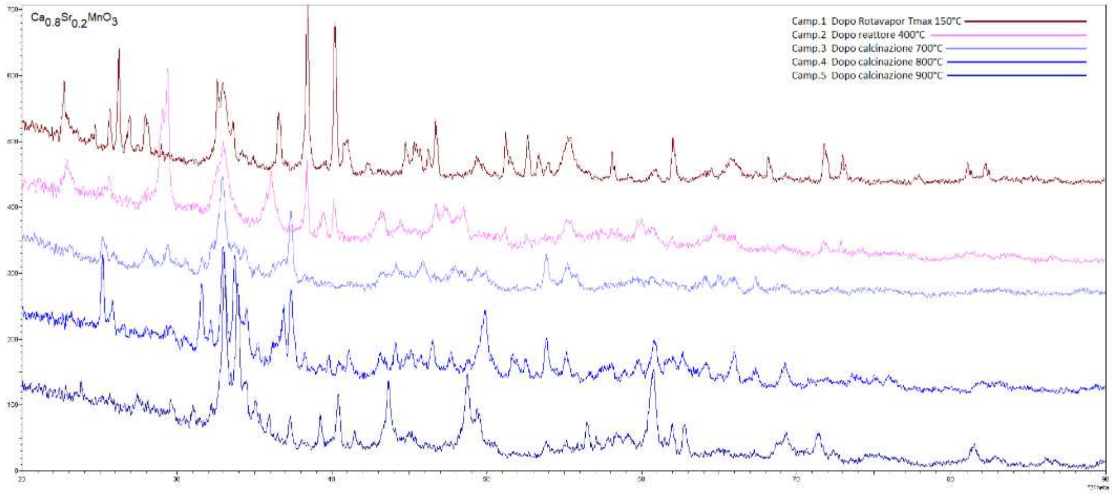

Figure 51- XRD analysis- Second route: comparison of CSM samples prepared, following the steps of the synthesis method.

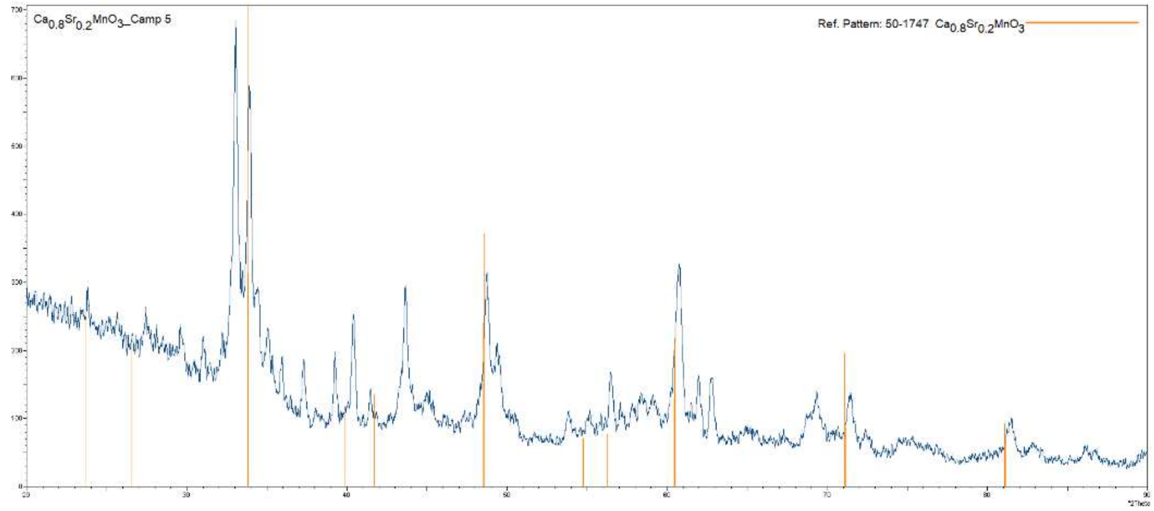

Figure 52- XRD analysis- Second route: CSM calcinated for 2h at 900°C.

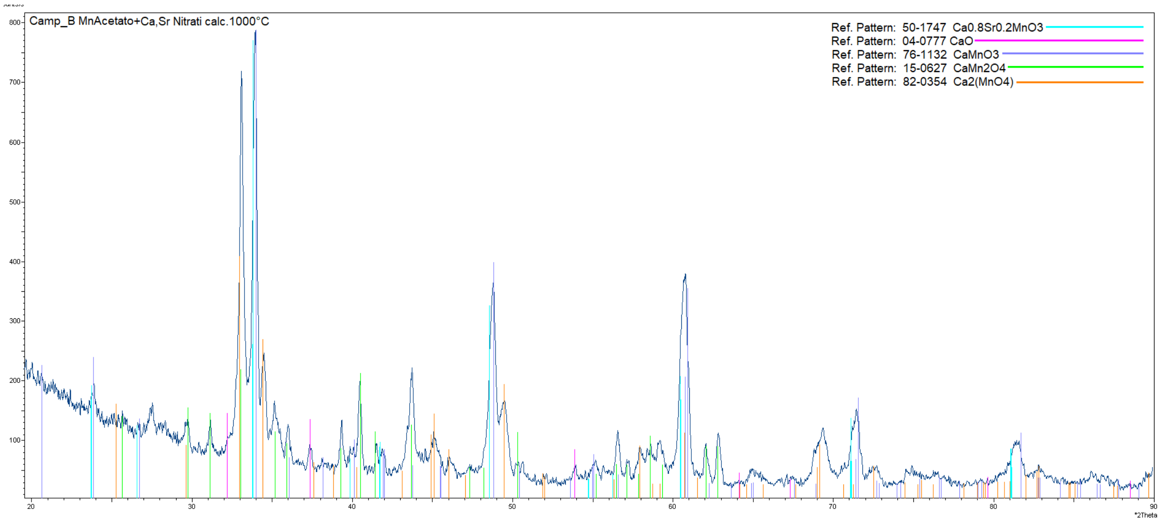

Figure 53- XRD analysis- Second route: CSM calcinated for 2h at 1000°C.

5.1.3 Third route

The mechanically activated dry mixture is prepared by dry milling of around 2g of mixture: the powders are placed in an Agata jar (80 ml) of a planetary ball mill (PM100) with 14 Agata balls, 2 of 10mm diameter, 4 of 8mm and 8 of 4mm, for a total mass of about 32g; the resulting mass ratio between the balls and the sample powders is 16:1. The mill operated at 500 rpm rotational speed for 12 hours. The milling process was not carried out in a continuous operation way; in fact, for every hour of milling, the mill was stopped 30 min, to avoid overheating and to realise the stress accumulated on the balls.

Since the energy transferred could be enough to totally or partially synthesise the perovskites, XRD analysis was also performed before calcination. The result of these analysis are shown in Figure 54, it is evident that no perovskite was already synthesized, while two mixed carbonates are formed: $CaMnCO_3$ and $Ca(Ca,Mn)CO_3$. This first bond between two different carbonates may help the formation of perovskite during calcination, facilitating the doping of strontium into the crystal structure of the perovskite. In conclusion, it can be stated that this milling process represents a chemical activation of the starting material.

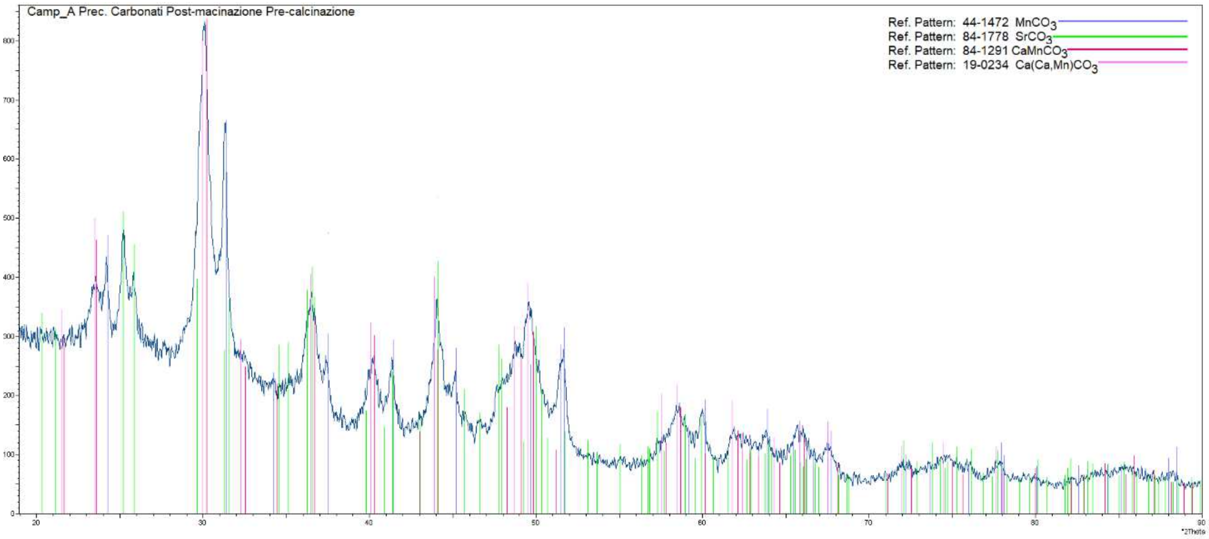

Figure 54-XRD analysis- Third route: CSM ready to be calcinated. It is evident that no perovskite was already synthesized, while two mixed carbonates are formed: $CaMnCO_3$ and $Ca(Ca,Mn)CO_3$.

The calcination process, according to the considerations made in the previous section, was carried out only at 1000°C, following the method already described. Figure 55 shows the XRD analysis after calcination; the milling activation of the powders allowed the formation of the perovskite during the calcination. Although there are some very weak peaks along the entire curve, the pattern of the perovskite is the only one detected and reported, which means that the perovskite was formed with high purity.

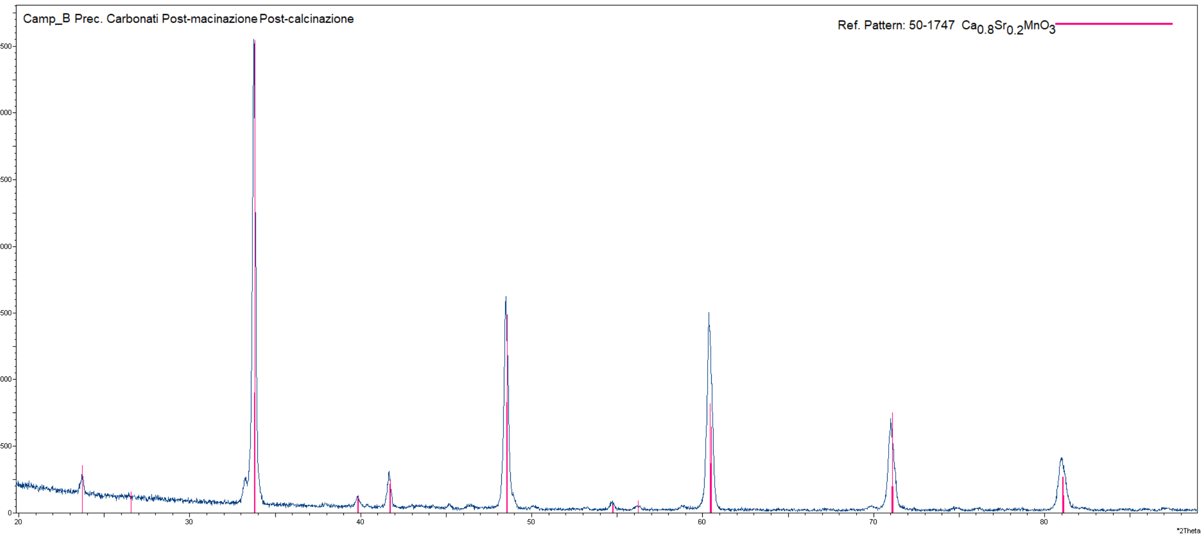

Figure 55-XRD analysis- Third route: CSM calcinated for 2h at 1000°C after milling in Agata jar.

With this type of jar, a maximum of about two grams of perovskite can be synthesised in a single process, while the aim of part of this work was to produce at least 15 grams of each powder, which was the minimum amount needed for all subsequent analyses, including the corresponding possible mass losses. Due to the limited capacity of the jar, the other milling processes were carried out in largest jars made with different materials. The specifications of these processes are summarized in Table 12. The milling process was also modified by reducing the grinding time from 12 hours to 2 hours and the rotational speed from 500 rpm to 300 rpm. For the same reasons reported before for the Agata milling process, a 15-minute pause was required for every 15 minutes of milling. The materials used for these other processes were stainless steel and zirconium oxide.

Table 12- Summary of the milling processes characteristics used in this work to synthetize CSM perovskites.

	Powders	Jar and balls material	Jar volume	Mass and diameter of the ball	Mass ratio	Time of effective milling	RPM	PBM
1	CSM (4 g)	Stainless steel	125 ml	5 balls d=15mm m=13.7g for each	1:17	2 hours	300	PULVERISETTE 5
2	CSM (16.5 g)	Zirconia	500ml	5 balls d=30mm m=77g for each	1:23	2 hours	300	PM 100

Figure 56 and Figure 57 show the XRD results of the synthesis of CSM powders by grinding, respectively, with stainless steel and zirconium oxide; in both cases the perovskite was formed but some impurities are present due to the release of material during the milling process. These materials were some residues of the jar and ball washing process, which is done by grinding some silicates typically for 1 hour at 500 rpm. In the case of zirconium oxide, the impurity was identified as (Na_2CaSiO_4).

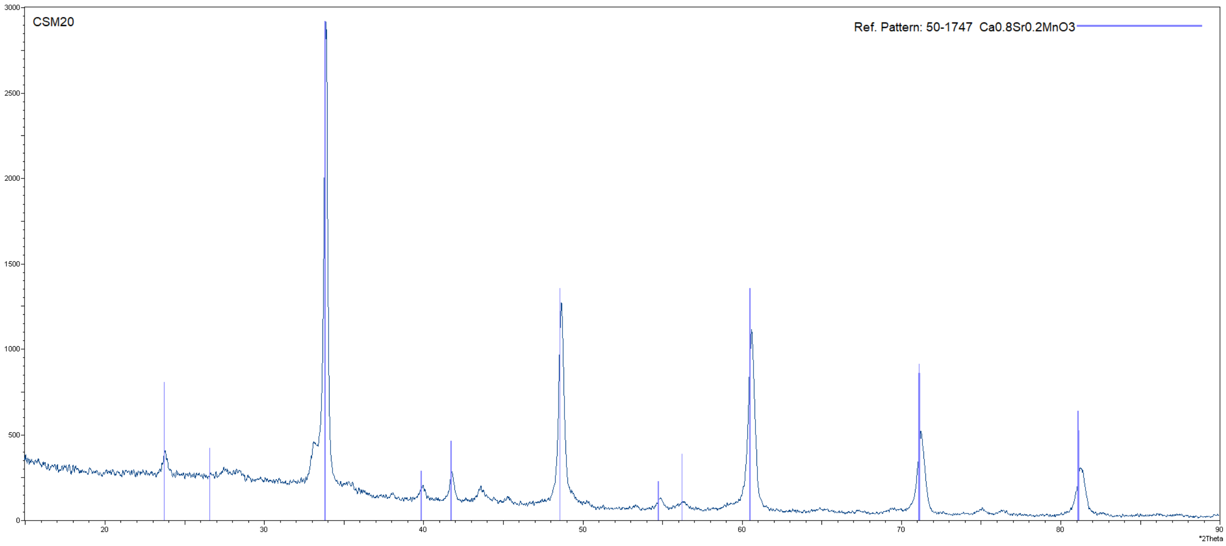

Figure 56- XRD analysis- Third route: CSM calcinated for 2h at 1000°C after milling in a stainless-steel jar.

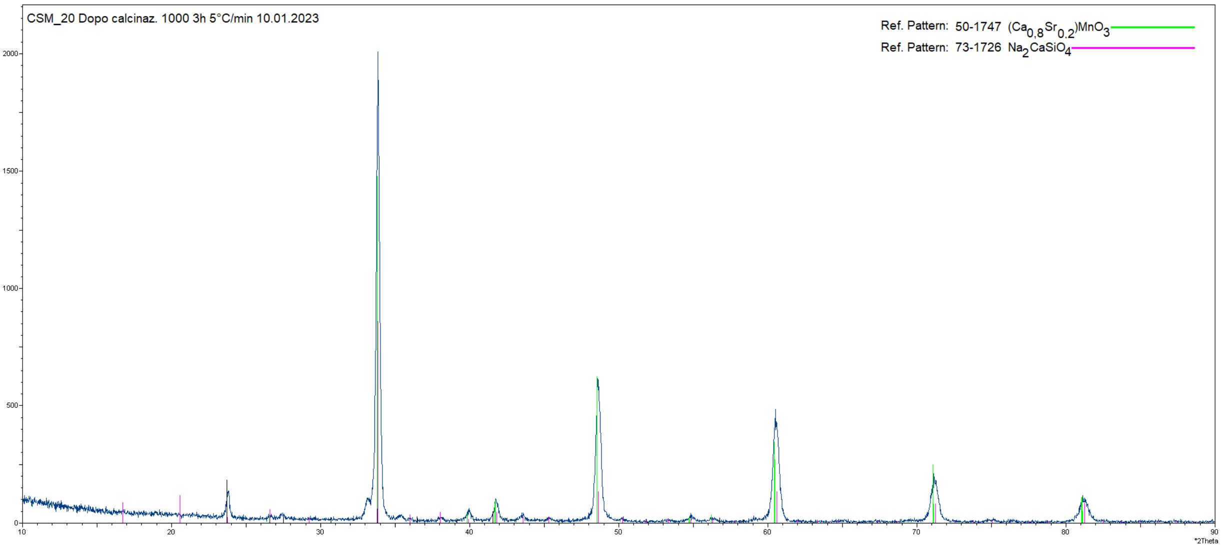

Figure 57- XRD analysis- Third route: CSM calcinated for 2h at 1000°C after milling in zirconium oxide jar.

In addition, for the stainless-steel process, the presence of steel compounds in the final mix was also investigated using the MP-AES technique. The results in ppm are reported in Table 13.

Table 13- MP-AES results- CSM prepared with a stainless-steel jar milling process and calcinated at 1000°C for 2 h.

Elements	PPM
Cr	0.1
Mo	0.09
Fe	2.68
Ni	0.11

In both cases, the presence of impurities can be neglected as they do not consistently affect the potential redox performance of the perovskite.

The total transferred energy can be estimated by using the equations reported in section 3.3. Table x summarises the results considering the milling process of the CSM 20 with stainless steel in Pulverisette 5 mill.

Table 14-CSM: HEBM in stainless-steel, with 5 balls for 2 hours at 300rpm. The constants are chosen as: $K_a = 1, K_b = 0.98, K_v = 1.5$ [91].

$Energy\ transfer\ model$	
$\Delta E\ \left[\frac{J}{hit}\right]$	$10 * 10^{-2}$
$Frequency\ of\ hit\ \left[\frac{hit}{s}\right]$	276
$Time\ [s]$	7200
$Total\ energy\ transferred\ per\ gram\ of\ powder\ \left[\frac{kJ}{g}\right]$	43

5.1.4 Other perovskites syntheses

The study of the crystalline structure formed in each different route tested for CSM20 preparation identifies the third one as the best method in terms of perovskite formation and purity. The other two perovskites selected in this work, LAF and LSF, were therefore synthetized using the same approach. A summary of all the tests performed are reported in Table 15.

Table 15- Summary of the methods used to prepare LAF20 and LSF20 perovskites.

	Powders	Jar and balls material	Jar volume	Mass and diameter of the ball	Mass ratio	Time of effective milling	RPM
1	LAF (2 g)	Agata	80 mL	2 with a diameter of 10mm, 4 of 8mm and 8 of 4mm	1:17	9 hours	500
2	LAF (2 g)	Agata	80 mL	2 with a diameter of 10mm, 4 of 8mm and 6 of 4mm	1:16	6 hours	500
3	LSF (18g)	Zirconia	500 mL	5 balls d=30mm m=77g for each	1:21,5	2 hours	300

During the first test, one of the smaller balls broke, contaminating the results. To avoid this breakage, the grinding time was then reduced from the second test onwards.

Figure 58 shows the XRD results of the LSF synthesis; as before, some impurities due to the washing material are present but also the perovskite were formed.

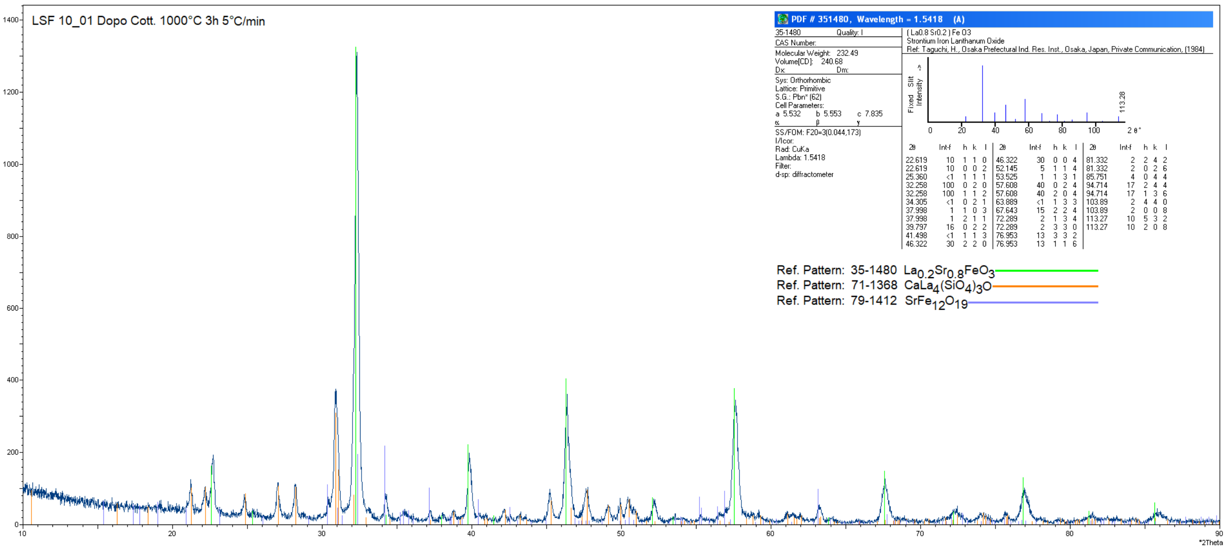

PDF # 351480, Wavelength = 1.5418 (A)

35-1480 Quality: I
CAS Number:
Molecular Weight: 232.49
Volume[CD]: 240.68
Dx: Dm:
Sys: Orthorhombic
Lattice: Primitive
S.G.: Pbn* (62)
Cell Parameters:
a 5.532 b 5.553 c 7.835
α β γ
SS/FOM: F20=3(0.044,173)
I/Icor:
Rad: CuKa
Lambda: 1.5418
Filter:
d-sp: diffractometer

(La0.8 Sr0.2) Fe O3
Strontium Iron Lanthanum Oxide
Ref: Taguchi, H., Osaka Prefectural Ind. Res. Inst., Osaka, Japan, Private Communication, (1984)

2θ	Int-f	h	k	l	2θ	Int-f	h	k	l	2θ	Int-f	h	k	l
22.619	10	1	1	0	46.322	30	0	0	4	81.332	2	2	4	2
22.619	10	0	0	2	52.145	5	1	1	4	81.332	2	0	2	6
25.360	<1	1	1	1	53.525	1	1	3	1	85.751	4	0	4	4
32.258	100	0	2	0	57.608	40	0	2	4	94.714	17	2	4	4
32.258	100	1	1	2	57.608	40	2	0	4	94.714	17	1	3	6
34.305	<1	0	2	1	63.889	<1	1	3	3	103.89	2	4	4	0
37.998	1	1	0	3	67.643	15	2	2	4	103.89	2	0	0	8
37.998	1	2	1	1	72.289	2	1	3	4	113.27	10	5	3	2
39.797	16	0	2	2	72.289	2	3	3	0	113.27	10	2	0	8
41.498	<1	1	1	3	76.953	13	3	3	2					
46.322	30	2	2	0	76.953	13	1	1	6					

Figure 58-XRD analysis- Third route: LSF calcinated for 3h at 1000°C after milling in zirconium oxide jar.

Unfortunately, for LAF 20 (Figure 59), the pattern of the perovskite was not available in the XRD Instrument database; however, disregarding the presence of iron oxide in its diffractogram, the other pattern reported is $LaFe0_3$, which is itself a perovskite. Starting from this reference, all the peaks of the sample are slightly shifted to the right, which may be due to the doping with aluminium in the crystal structure. Therefore, there is a high probability that the required perovskite was formed.

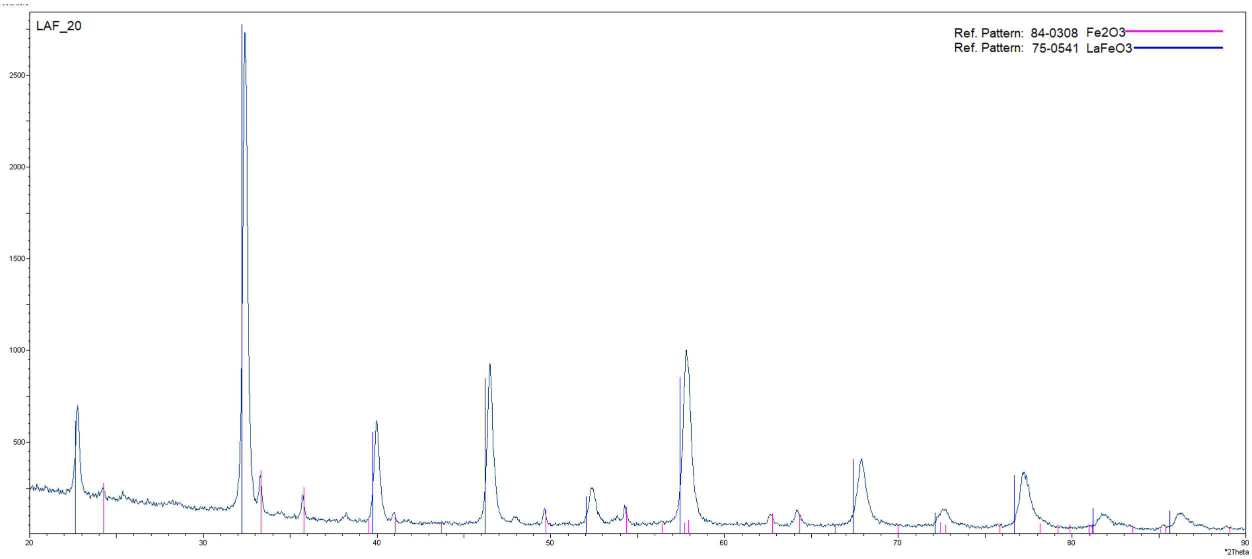

Figure 59- XRD analysis- Third route: LAF calcinated for 3h at 1000°C after milling in agata jar.

However, no further investigation regarding the redox capabilities of the LAF 20 were performed because, as can be seen in Figure 60, it is not reducible under nitrogen at 1000°C $\left(\frac{dm}{dt} \approx 0\right)$, which is the limiting operating upper temperature considered in this work.

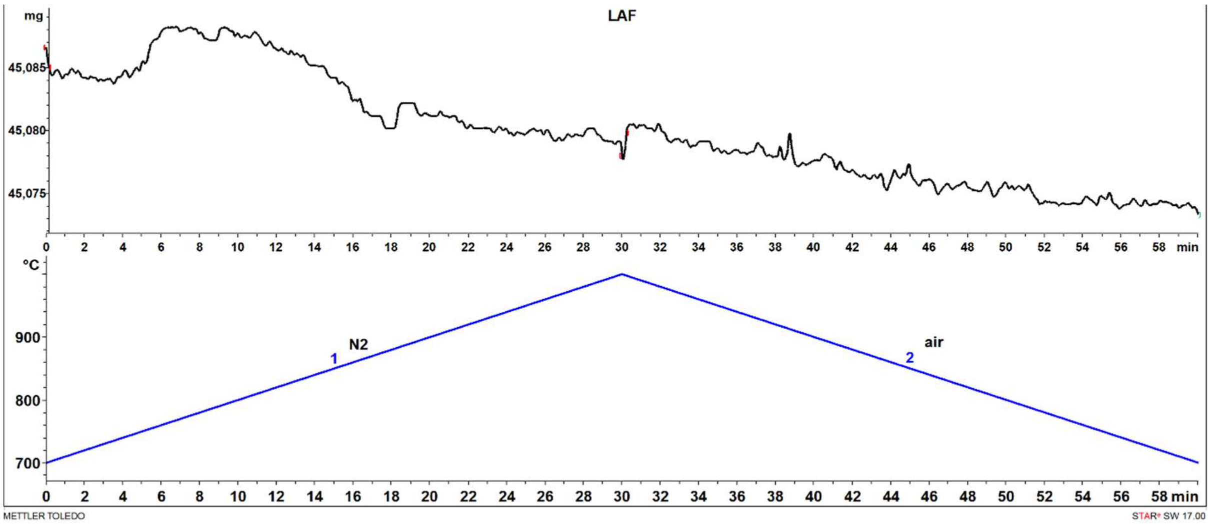

Figure 60- TGA/DTA analysis of LAF: the Figure shows, from top to bottom, the thermo-gravimetric pattern and the temperature program used. Test carried out with a flow of 40 Nml/min of N2 (segment 1) and of 40 Nml/min of air (segment 2).

5.1.5 Perovskites Morphology

The perovskites morphology was evaluated by SEM technique. In Figure 61 is reported the SEM analysis of the synthesized CSM before thermal cycles with magnification of 10µm on the left and 1 µm on the right. CSM is formed by the aggregation of small particles, with resulting size of around 15-20 µm.

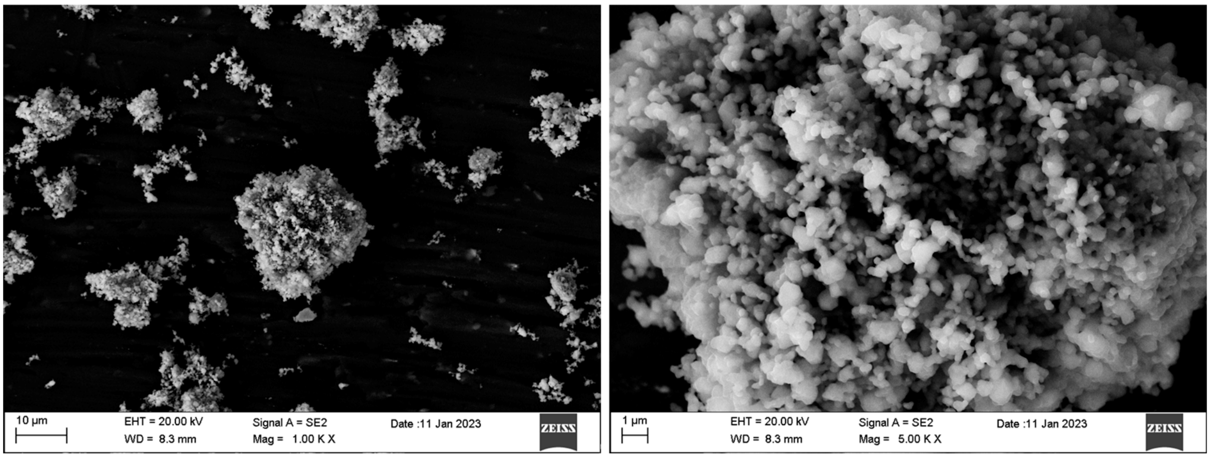

Figure 61-SEM analysis of the synthetized Ca0.8Sr0.2MnO3 (CSM) before thermal cycles; magnification of 10µm (on the left) and 1 µm (on the right).

The average diameter of the particles forming the agglomerates was measured by increasing the magnification of the SEM to 25000x, which corresponds to a scale of 200nm. This analysis is reported in Figure 62. The mean diameter of the CSM particles is estimated to be around 280 nm; this parameter will be used to evaluate the kinetic constants, as explained in the following sections.

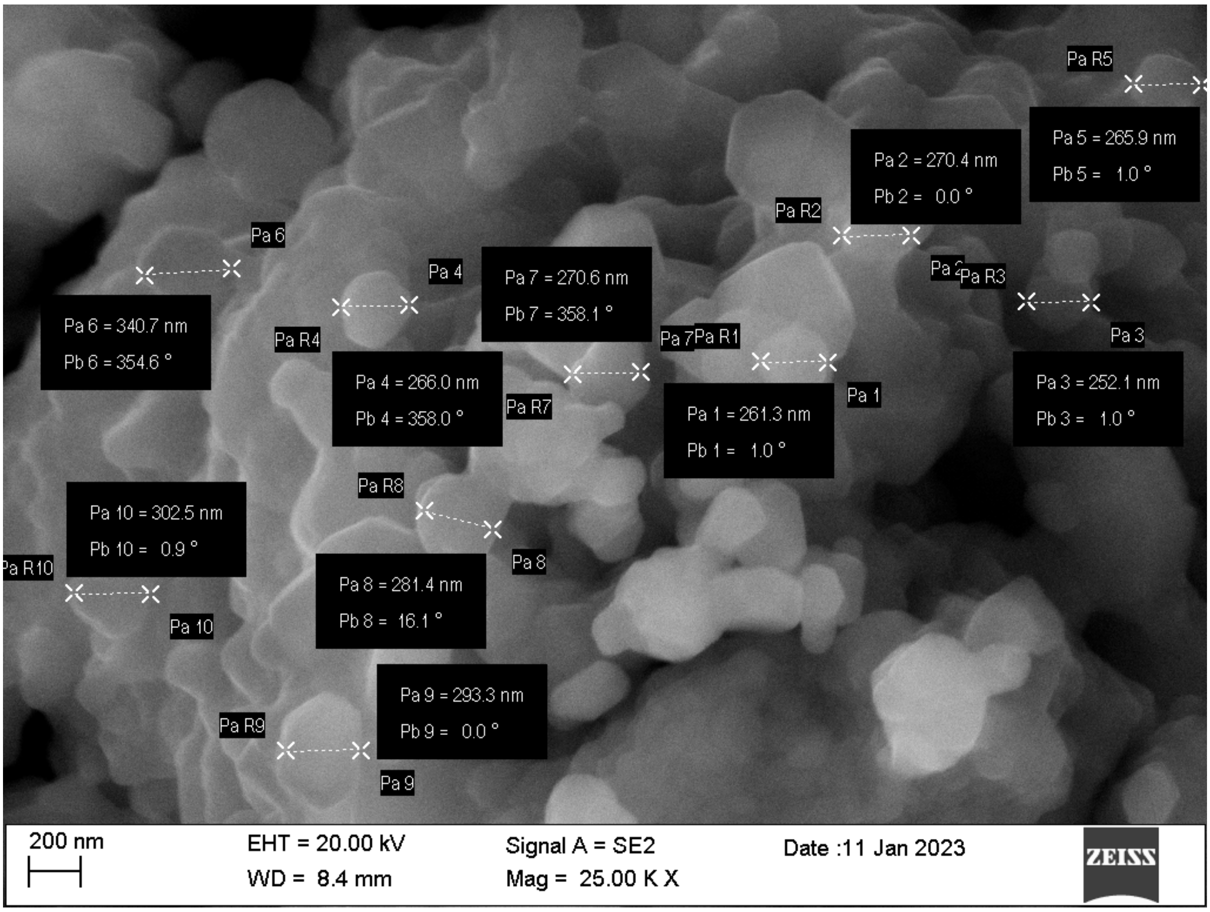

Figure 62-SEM analysis of the synthetized Ca0.8Sr0.2MnO3 (CSM) before thermal cycles (magnification of 200µm); averaged diameters of the particles measured and reported.

The same analysis were carried out for the LSF, and the corresponding SEM images are shown in Figure 63 and Figure 64. The agglomerates appear to be larger with respect to those of the CSM and are of the order of 30 µm, while the mean diameter is smaller, about 70 nm.

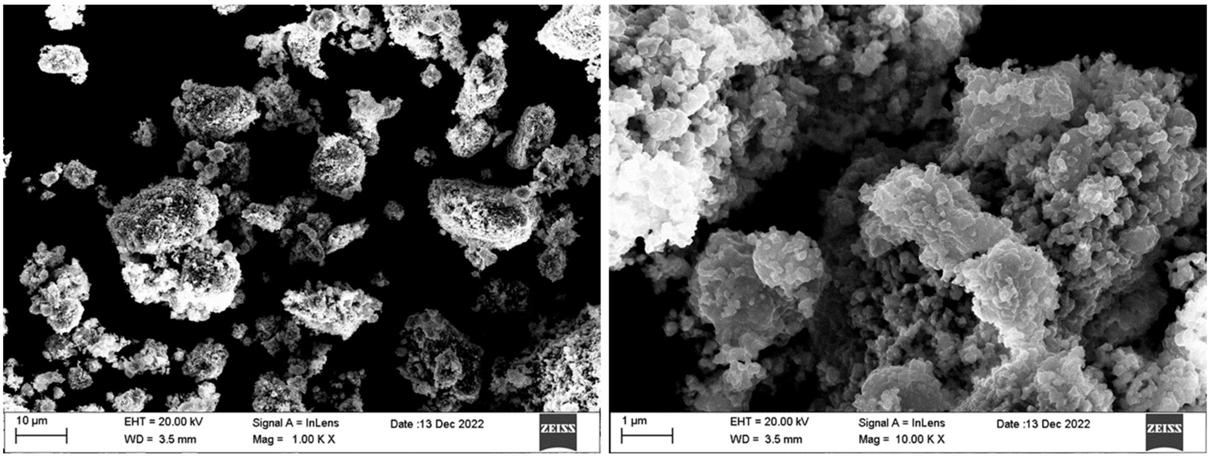

Figure 63-SEM analysis of the synthetized LA0.8Sr0.2FeO3 (CSM) before thermal cycles; magnification of 10µm (on the left) and 1 µm (on the right).

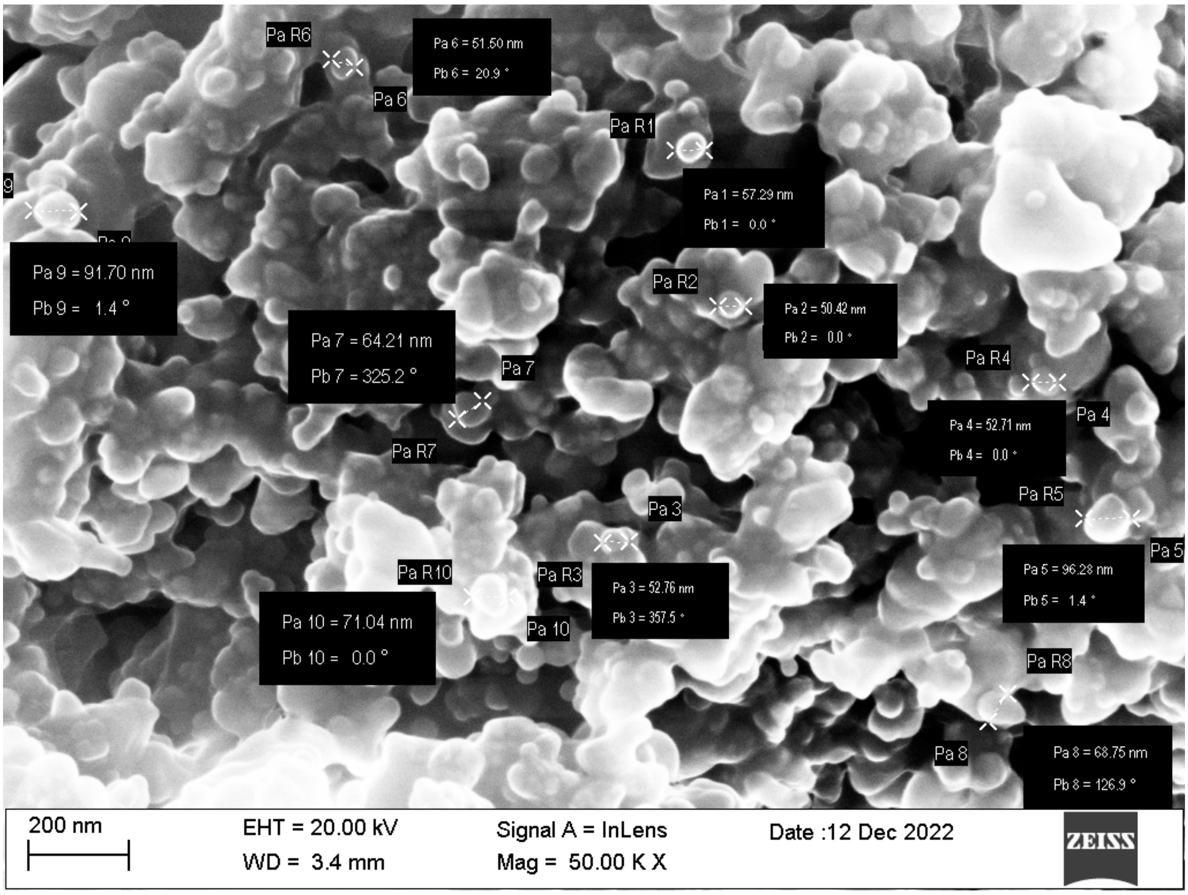

Figure 64-SEM analysis of the synthetized LA0.8Sr0.2FeO3 (LSF) before thermal cycles (magnification of 200µm); averaged diameters of the particles measured and reported.

5.2 CSM: thermophysical, thermodynamic and kinetic evaluations

In this section all the experimental and theoretical results obtained for the CSM are reported and discussed in detail.

5.2.1 Specific heat measurement

Using the method already described in Chapter 4, ten independent tests were performed to determine the specific heat, using the temperature program shown in Figure 39, within a temperature range between 50 and 500 °C. An example of a DSC pattern is illustrated in Figure 65, while the resulting cp as a function of temperature is shown in Figure 66.

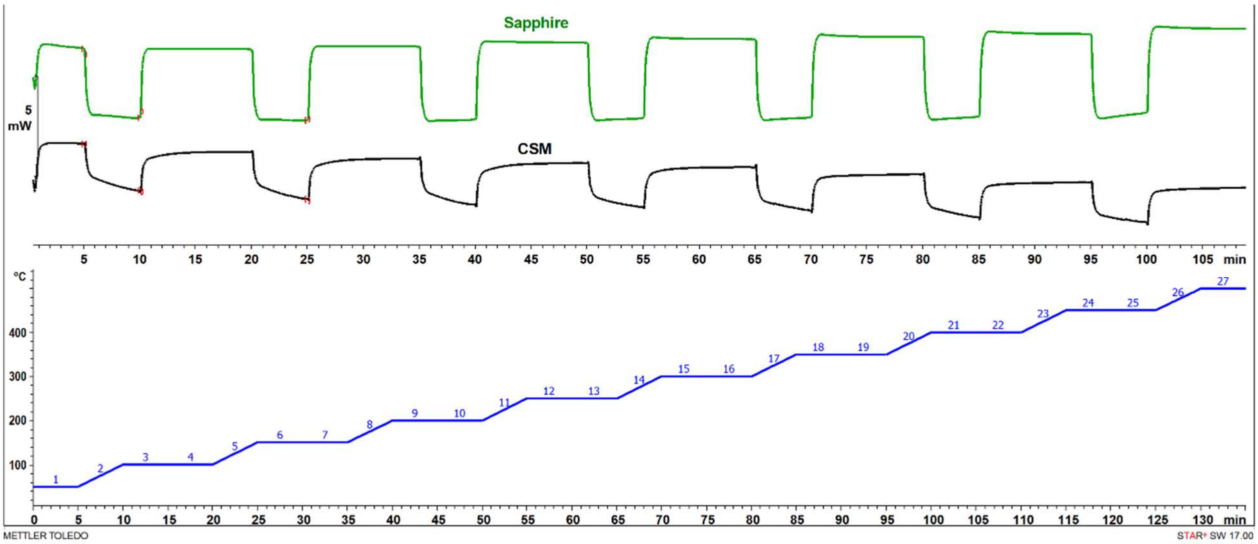

Figure 65-Example of DSC measurement test: from top to bottom, the sapphire heat flow, the sample heat flow, the used temperature program. All the segments were carried out under 40 Nml/min of air.

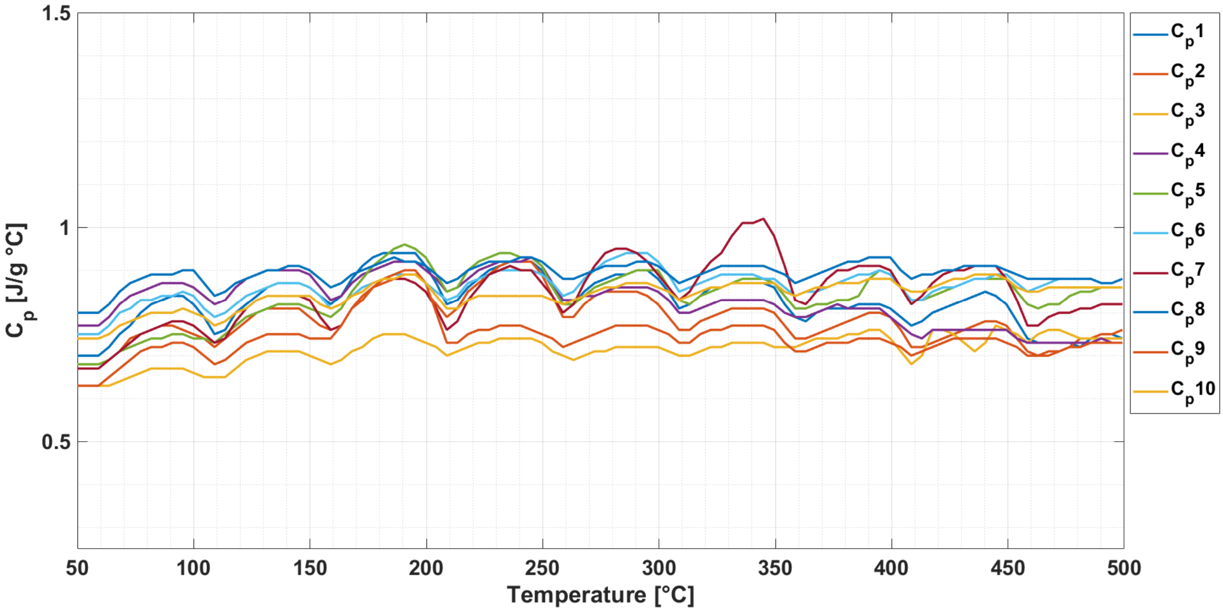

Figure 66- Overlaid DSC patterns of the CSM heat capacity between 50 and 500 °C

Collecting all the data set, the average specific heat as function on temperature was then evaluated and reported in Figure 67, with its error bar. The maximum error, considered with an interval of confidence of 99%, is about the 9%.

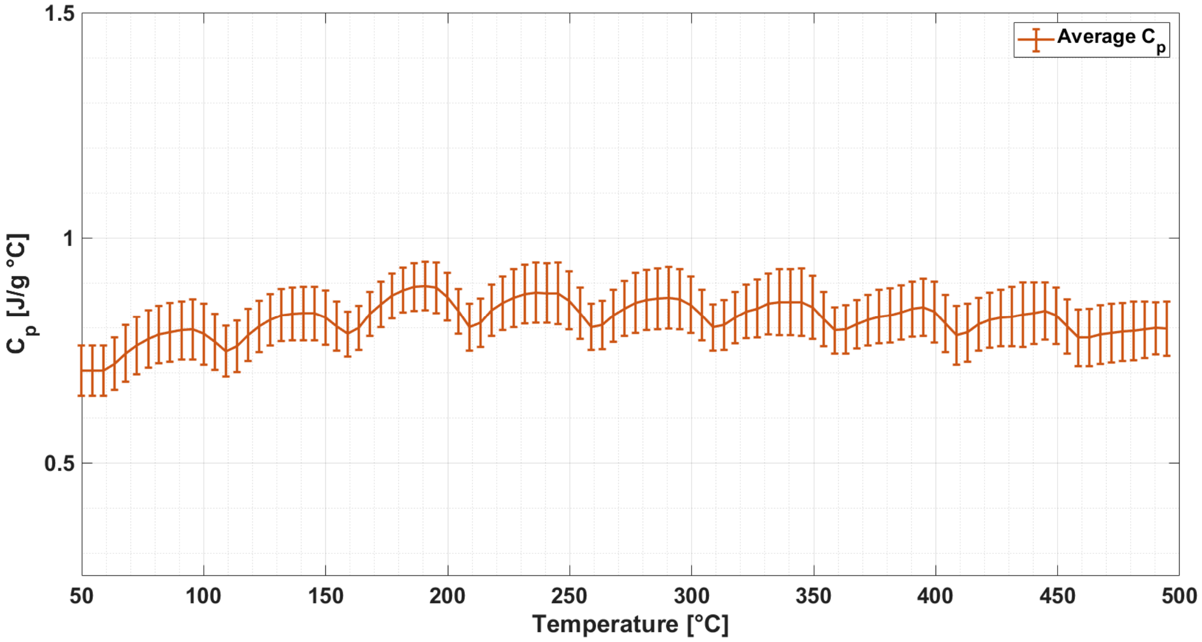

Figure 67-CSM average specific heat as function on temperature.

The result was linearly fitted as following:

$$Cp = 0.00007\,T + 0.80050$$

Where the Cp is expressed as $\left[\frac{J}{g\,°C}\right]$ and the Temperature as [°C]. From the fitting it is clear the weakly dependence of the specific heat with temperature.

5.2.2 Average enthalpy of reaction

Reaction enthalpy is the energy required or released during the reaction and it is a function of temperature and δ, according to [84];this last dependence can be considered weak and therefore neglected. For the aim of this work, it was not necessary to find an expression between enthalpy and temperature, but to measure the average reaction enthalpy at high temperatures, compliant to the theoretical levels for the thermal reduction.

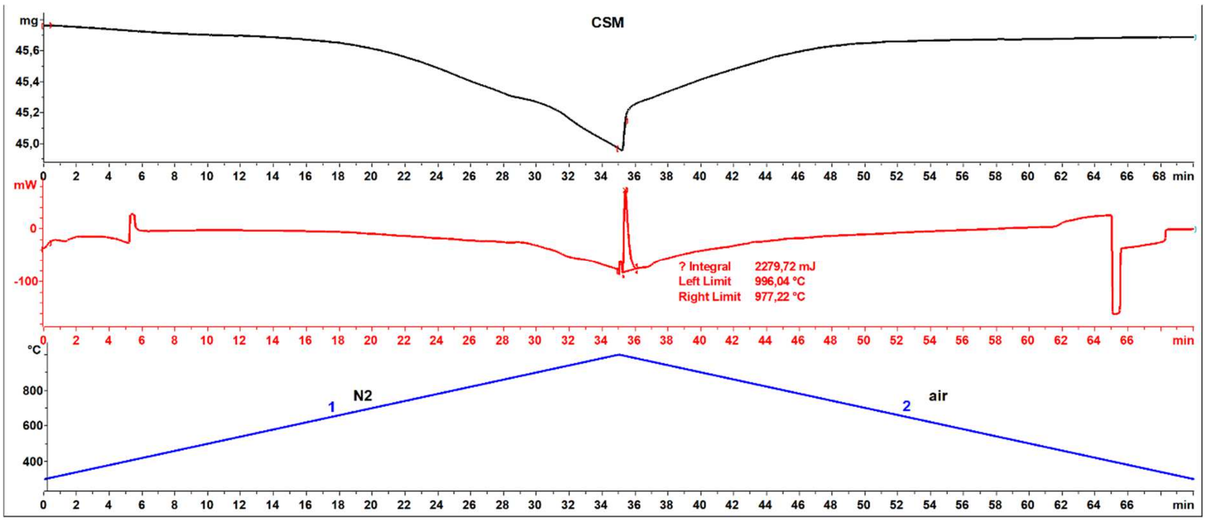

Figure 68- TGA/DTA analysis of CSM: the Figure shows, from top to bottom, the thermo-gravimetric pattern, the heat-flow and the temperature program used. The red line shows the reaction enthalpy measured by integrating the exothermic peaks between the temperature indicate in figure as left limit and right limit. Test carried out with a flow of 40 Nml/min of N2 (segment 1) and of 40 Nml/min of air (segment 2).

In the middle part of the Figure 68 the DTA analysis performed for the CSM is reported, which is submitted to the temperature program reported on the bottom part of the same figure. Reaction enthalpy is measured by integrating the exothermic peaks between the temperature indicated in figure as left limit and right limit.

The endothermic heat of reduction is not visible from the DTA analysis due to the slow time evolution of the reaction; however, it can be taken equal to the one measured for the oxidation because reduction is the inverse reaction. As a first approximation, this value is taken also for the water shift. The obtained value is then normalized with respect to the absorbed oxygen and, due to calibration issues of the instrument, was adjusted through an external calibration curve (empirical fitting). The results are reported in Table 16.

Table 16-CSM reaction enthalpy measured by DTA analysis.

Measured ΔH	2279.72	mJ
mg of absorbed oxygen	0.31	mg
mmol of absorbed oxygen	0.0097	$mmol\ O2$
$Measured\ \Delta H$	235	$\frac{kJ}{molO_2}$
Extern calibration (Second-order polynomial)	$0.012x^2 + 0.1764x + 22.085$	-
$Adjusted\ \Delta h$	130	$\frac{kJ}{molO_2}$

5.2.3 Thermodynamic considerations

In the scientific literature, the perovskites thermodynamics presents several issues due to the formation of intermediate solid phases, which have, correlated with the variation of stochiometric coefficient δ, different formation Gibbs free energy. In this thesis the same approach shown by [78], [84], [83].

Firstly, it was necessary to verify that equilibrium conditions can be achieved by working with the TGA. To do this, the CSM powders, analysed with the thermogravimetry, were used to fill a batch reaction, with the aim to directly measure the equilibrium oxygen pressure at different temperatures (section 3.1.1). The results from the batch reactor showed that the equilibrium pressure was reached after some minutes along the various isotherms.

Figure 69 shows the temperature profile and the evolution of the pressure over time. Starting from 400°C, the batch reactor was heated by a radiative heater and the pressure of the system was measured by a manometer installed outside the reactor. The trend of the temperature ramp is very similar to that of the absolute pressure, therefore when the temperature becomes constant, the pressure does not change with time. This experimental setup demonstrated that equilibrium was reached under sufficiently rapid conditions to permit the measurement of equilibrium δ, as a function of temperature and oxygen partial pressure, by thermogravimetry.

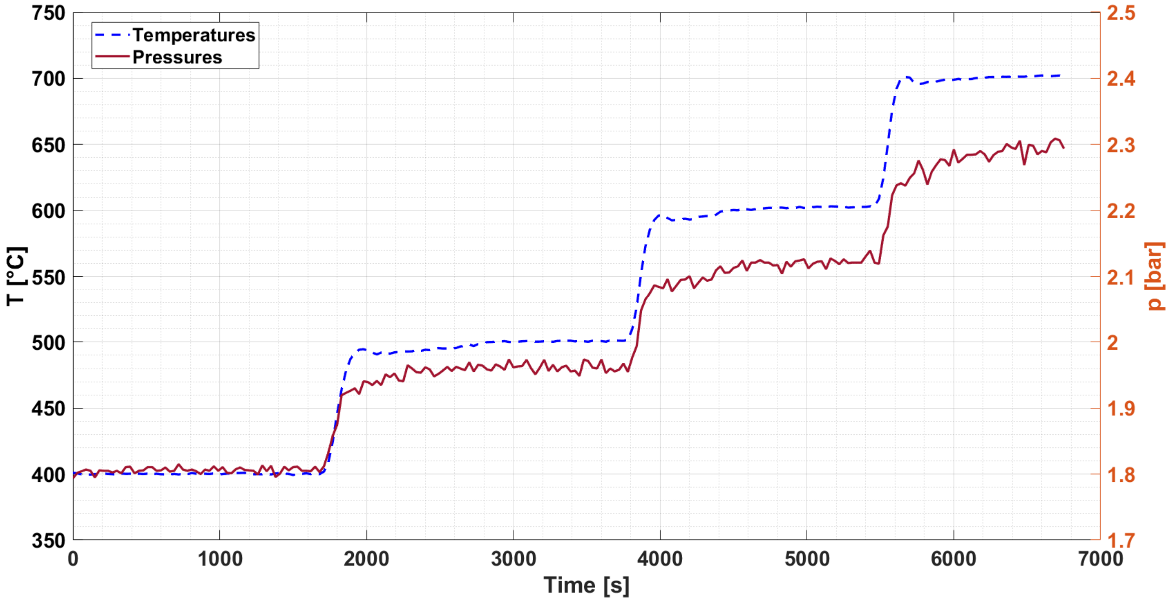

Figure 69- CSM: evolution of pressure staring from 400°C to the isothermal condition at around 700°C, with a stepped heating mode.

The estimation of the equilibrium δ was done by testing the perovskite under reduction and oxidation cycles using descending oxygen partial pressure, from 0.2 bar to 0.025 bar and at maximum constant temperatures. Between each cycle a short isothermal was set, allowing the reaction to reach the equilibrium. An example of this methodology is reported in Figure 70.

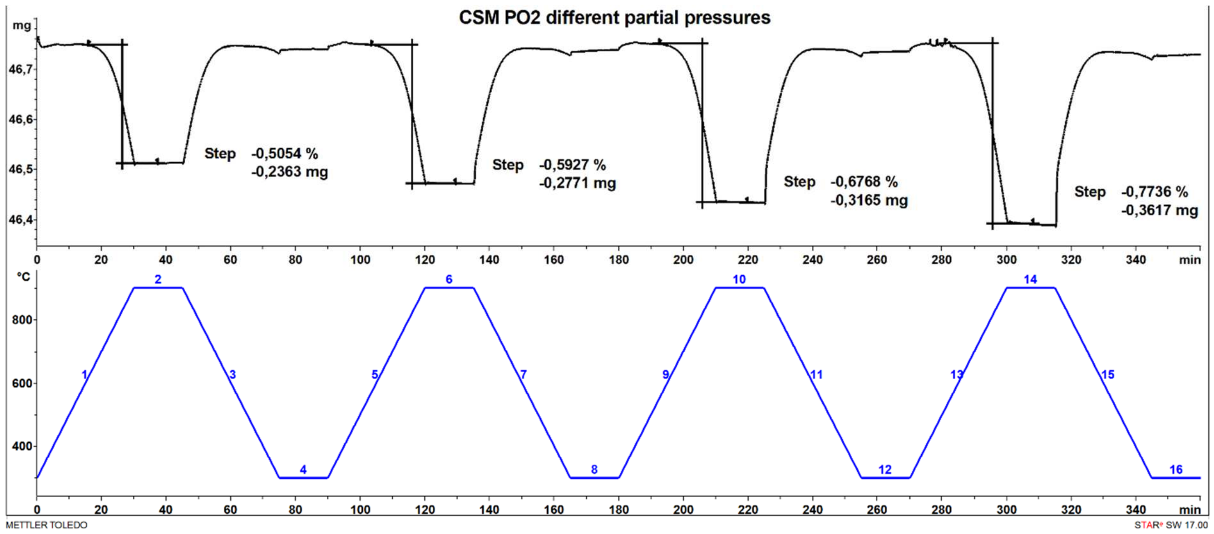

Figure 70- TGA/DTA analysis of CSM: the figure shows, from top to bottom, the thermo-gravimetric pattern and the temperature program used. Test carried out with a flow of 40 Nml/min of N2 (segments 1-2) and of 40 Nml/min of air (segments 3-4), varying oxygen partial pressure, from 0.2 bar to 0.025 bar and at maximum constant temperatures.

The technical specifications of all TGA analysis performed varying oxygen partial pressures are reported in Table 17.

Table 17-CSM: Technical specifications of all the TGA analysis performed varying oxygen partial pressures.

	Temperature and Oxygen pressure program							
	1	2	3	4	5	6	7	8
$Nitrogen\ flow\ \left[\frac{mL}{min}\right]$	40	40	0	0	40	40	0	0
$Air\ flow\ \left[\frac{mL}{min}\right]$	0	0	40	40	0	0	40	40
$Heating\ rate\ \left[\frac{°C}{min}\right]$	20	0	-20	0	20	0	-20	0
$Temperature\ [°C]$	300-900	900	900-300	300	300-900	900	900-300	300
$pO_2\ [bar]$	0.2	0.2	0.2	0.2	0.1	0.1	0.2	0.2
	9	10	11	12	13	14	15	16
$Nitrogen\ flow\ \left[\frac{mL}{min}\right]$	40	40	0	0	40	40	0	0
$Air\ flow\ \left[\frac{mL}{min}\right]$	0	0	40	40	0	0	40	40
$Heating\ rate\ \left[\frac{°C}{min}\right]$	20	0	-20	0	20	0	-20	0
$Temperature\ [°C]$	300-900	900	900-300	300	300-900	900	900-300	300
$pO_2\ [bar]$	0.05	0.05	0.2	0.2	0.025	0.025	0.2	0.2

It is expected that as the oxygen partial pressure decreases, the mass variation in the reduction reaction increases; this is confirmed by the evaluation of the horizontal step tool of the TGA analysis. The mass variations are used to estimate the equilibrium δ, this procedure is illustrated in Table 18.

Table 18- CSM: mass variations from TGA analysis used to estimate the equilibrium δ.

pO_2 $[bar]$	$Molar\ mass$ $\left[\frac{mg}{mmol}\right]$	$Mass\ of\ the\ perovskite\ completely\ oxidated$ $[mg]$	$Mols\ of\ the\ perovskite\ completely\ oxidated$ $[mmol]$	$Oxygen\ mass\ released\ during\ the\ thermal\ reduction$ $[mg]$	$Moles\ of\ ½\ O_2\ released$ $[mmol]$	δ
0.2	152.53	47.760	0.313	0.236	0.015	0.047
0.1	152.53	47.760	0.313	0.277	0.017	0.055
0.05	152.53	47.760	0.313	0.317	0.020	0.063
0.025	152.53	47.760	0.313	0.362	0.023	0.072

This procedure was repeated for different temperatures between 750°C and 1000°C. Figure 71 summarises the evolution of the equilibrium δ as a function of the imposed oxygen partial pressure for each temperature considered. The points obtained by the batch reactor and the analysis carried out under nitrogen, considered as the limit of $pO_2 \rightarrow 0$, are also shown. The differences between the reactor analysis and the TGA analysis are due to temperature inhomogeneities of the powders inside the reactor. Actually, inside the batch reactor the powders temperature inhomogeneities can be conservatively of $\pm 30°C$, while the error on the δ estimation by TGA analyses, in first approximation can be neglected.

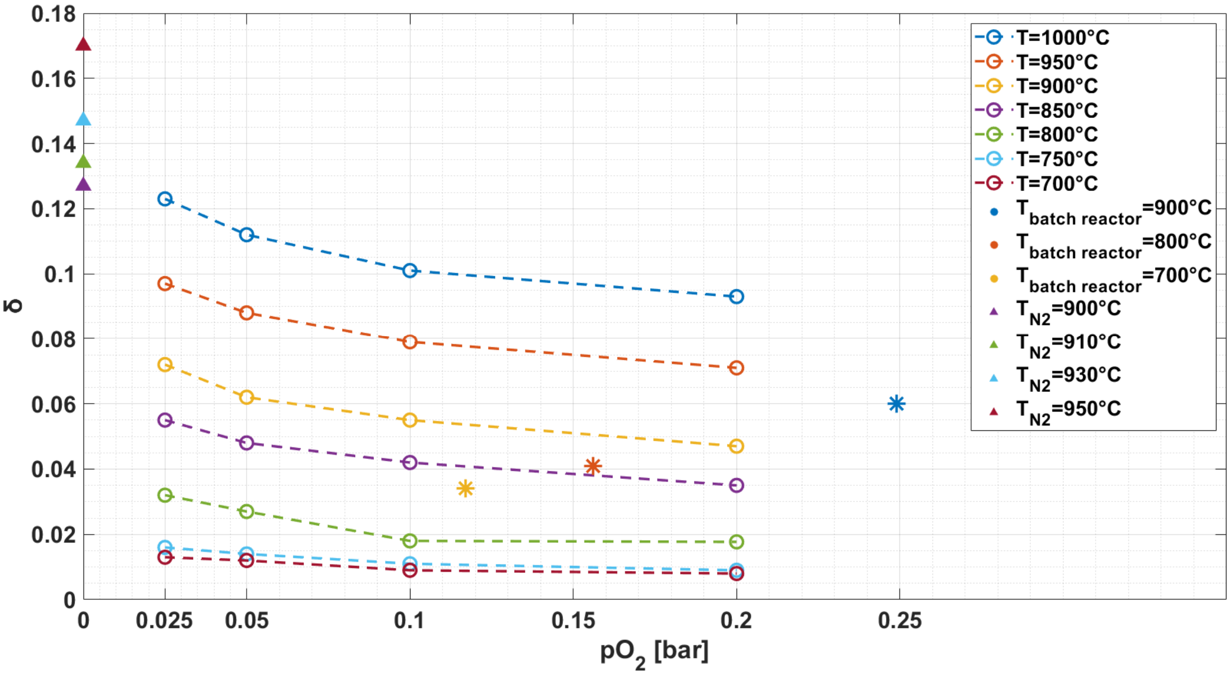

Figure 71- CSM: the graph shows the evolution of the equilibrium δ as a function of the imposed oxygen partial pressure for each temperature considered, the points obtained by the batch reactor and the analysis carried out under nitrogen, considered as the limit of $pO_2 \rightarrow 0$

The obtained trend for the equilibrium δ , which is around the same for each temperature, confirms what was written in the scientific literature: increasing pO_2, the equilibrium δ decreases. The points on the various isotherms can be seen as equilibrium conditions of different reactions which involve the formation of different perovskite lattices. As just seen in section 3.1, it can be possible to relate the difference between ΔG_f^0 of the oxidated and reduced solid with the oxygen partial pressure, through the equilibrium constant,K_{red} (Eq. 35). As an example, in Figure 72 are reported ΔG_{Solid}^0as a function of pO_2 at fixed temperatures.

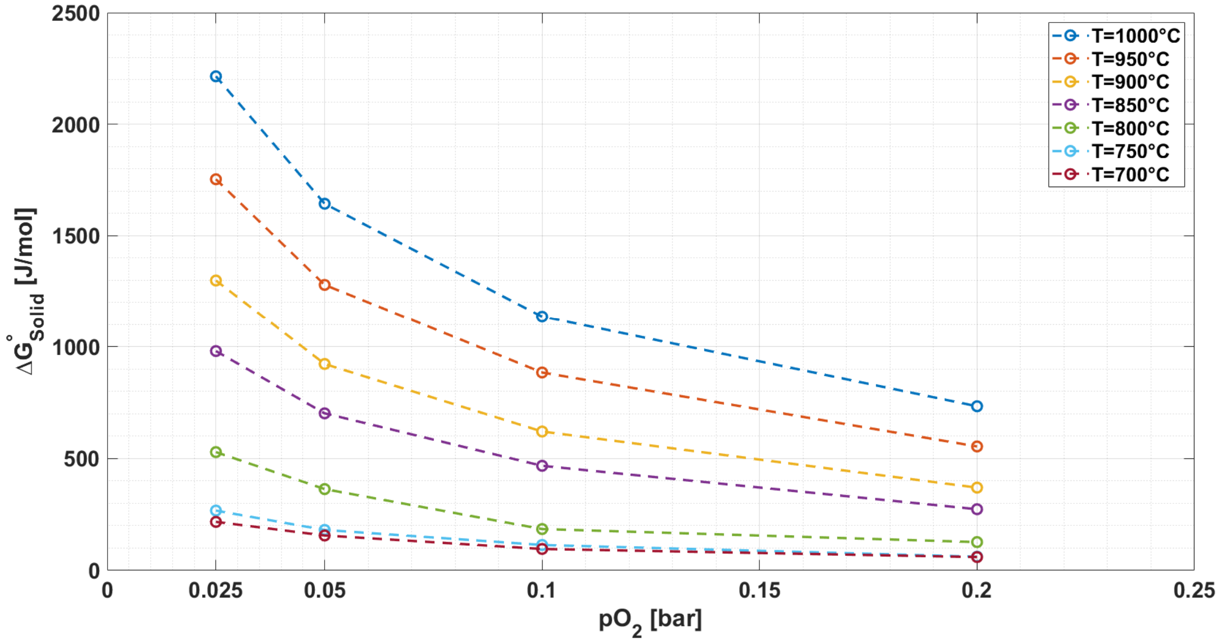

Figure 72- ΔG_{Solid}^0*as a function of* pO_2 *at fixed temperatures*

From this, as described by the Eq. 42, it is possible to extrapolate the minimum δ required for different temperatures levels that makes the oxidation reaction favourable, from a thermodynamic point of view. As an example, in Figure 73 , it is reported the ΔG_{Solid}^0as function of δ at 750°C. The other results are summarized in Table 19.

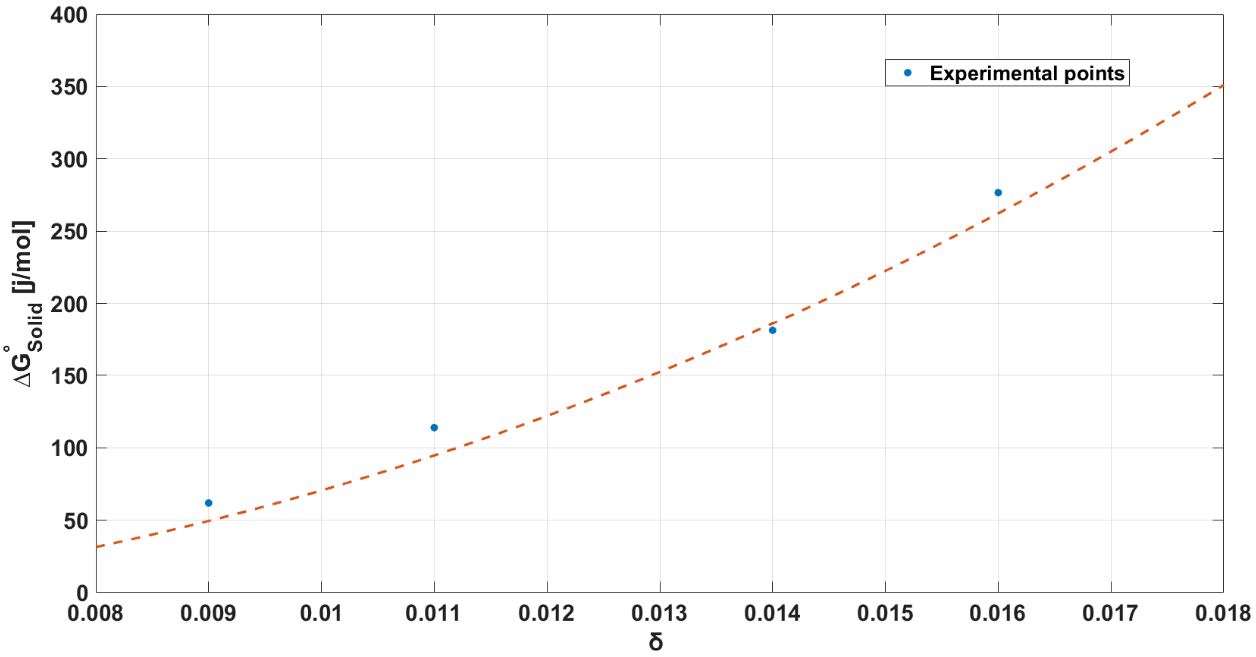

Figure 73-ΔG^0_{Solid}*as function of* δ *at 750°C.*

Table 19- ΔG^0_{Solid}*as function of* δ *at different temperatures.*

$Temperature$ $[°C]$	δ	ΔG_{Solid}° $\left[\frac{j}{mol}\right]$	$Temperature$ $[°C]$	δ	ΔG_{Solid}° $\left[\frac{j}{mol}\right]$
700	0.008	60	800	0.017	126.9
	0.009	96.1		0.018	185.1
	0.012	156.3		0.027	363.7
	0.013	217.2		0.032	529.0
$Temperature$ $[°C]$	δ	ΔG_{Solid}° $\left[\frac{j}{mol}\right]$	$Temperature$ $[°C]$	δ	ΔG_{Solid}° $\left[\frac{j}{mol}\right]$
850	0.035	273.7	900	0.047	370.2
	0.042	467.7		0.055	621.0
	0.048	702.1		0.063	922.8
	0.055	980.6		0.072	1298.6
$Temperature$ $[°C]$	δ	ΔG_{Solid}° $\left[\frac{j}{mol}\right]$	$Temperature$ $[°C]$	δ	ΔG_{Solid}° $\left[\frac{j}{mol}\right]$
950	0.071	554.2	1000	0.093	733.8
	0.079	884.7		0.101	1135.7
	0.088	1278.9		0.112	1643
	0.097	1752.8		0.123	2214.6

As a roughly approximation, a second-degree polynomial dependency, passing through the origin, can be used to model the variation of the ΔG^0_{Solid} with $\delta_{equilibrium}$ of the reaction. An example of a fitting is reported in Figure 74; in particular, the focus is posed on the point in which the $\Delta G^0_{Oxidation}$ becomes negative, which is the necessary condition that makes the water shift favourable from a thermodynamic point of view.

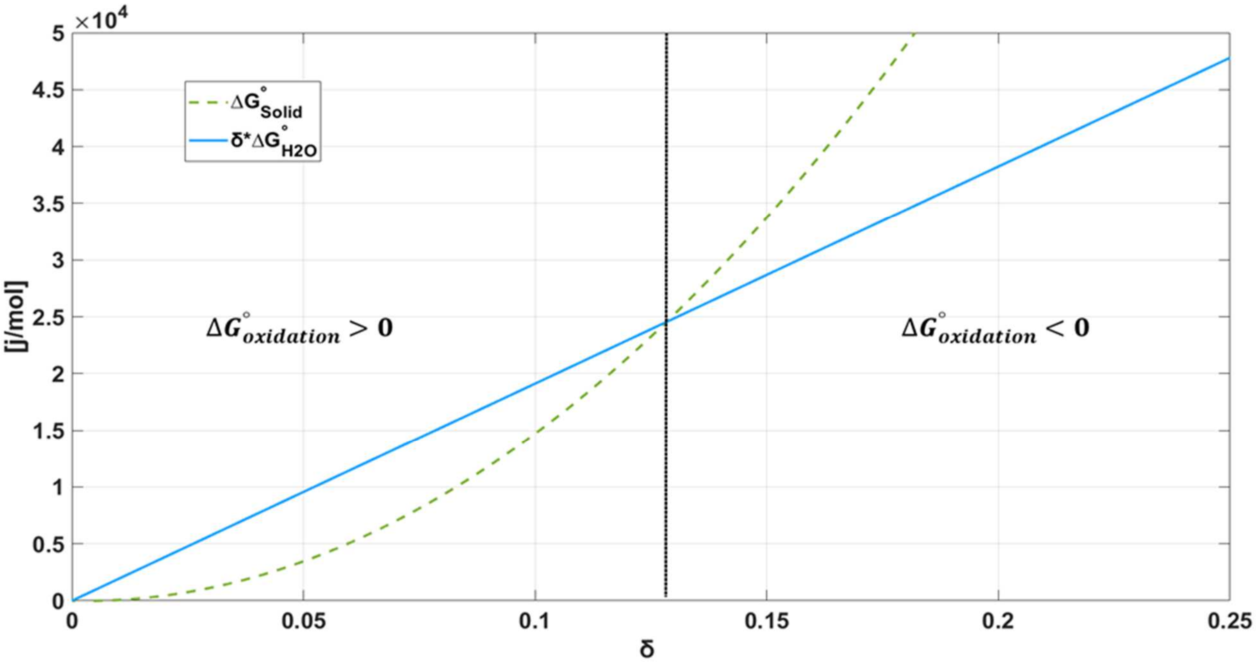

Figure 74- A second-degree polynomial dependency fitting, passing through the origin, used to model the variation of the ΔG^0_{Solid} with δ of the reaction. The focus is posed on the point in which the $\Delta G^0_{Oxidation}$ becomes negative, which is the necessary condition that makes the water shift favourable, from a thermodynamic point of view.

The results of this extrapolation were calculated and reported in Table 20.

Table 20- CSM: minimum δ, referring to oxidation at a fixed temperatures.

$Temperature\ [°C]$	$\delta_{minimum}$
700	0.11
750	0.13
800	0.35
850	0.36
900	0.48
950	0.54
1000	0.62

The main purpose of this thermodynamic analysis was to find a couple of temperatures, one for the thermal reduction and one for the re-oxidation with steam, suitable for the testing of the TCWS cycle based on CSM. This result was obtained comparing the values already reported in Table 20 with the ones from the thermal reduction under nitrogen. From this comparison, it is clear that the oxidation temperature must be lower than the reduction temperature.

The temperatures ranges selected are between 700 and 750°C for the oxidation step and between 900 and 950°C for the thermal reduction under nitrogen. To reduce as much as possible the kinetic limitation for both the temperatures the upper values were chosen. Therefore, for an oxidation temperature equal to 750°C, the minimum required δ value is around 0.13, which can be easily obtained carrying out the reduction reaction, under nitrogen, at 950°C.

5.2.4 Kinetic evaluations

Since the theoretical-experimentally thermodynamic results are favourable, the reduction and oxygen oxidation kinetics are studied. The aim is to provide and validate methodologies, that may be used to further investigations on these reactions.

5.2.4.1 Reduction step under nitrogen

For what concerns the nitrogen reduction, based on the equations reported in section 3.2, the Arrhenius constants are evaluated following two different models, and the results are reported in Table 21.

Table 21- Arrhenius constants evaluated following two different models.

Isothermal Approach			
Temperature [°C]	700	800	900
$A\ [s^{-1}]$	$7.8 * 10^{-6}$		
$E_a \left[\frac{J}{mol}\right]$	87067		
Non-isothermal approach			
$Heating\ rate\ \left[\frac{°C}{min}\right]$	5	10	20
$A'[s^{-1}]$	$5.5 * 10^{-6}$		
$E_a{}'\left[\frac{J}{mol}\right]$	74000		

Regarding the isothermal approach method, the Arrhenius least square fitting is reported in Figure 75.

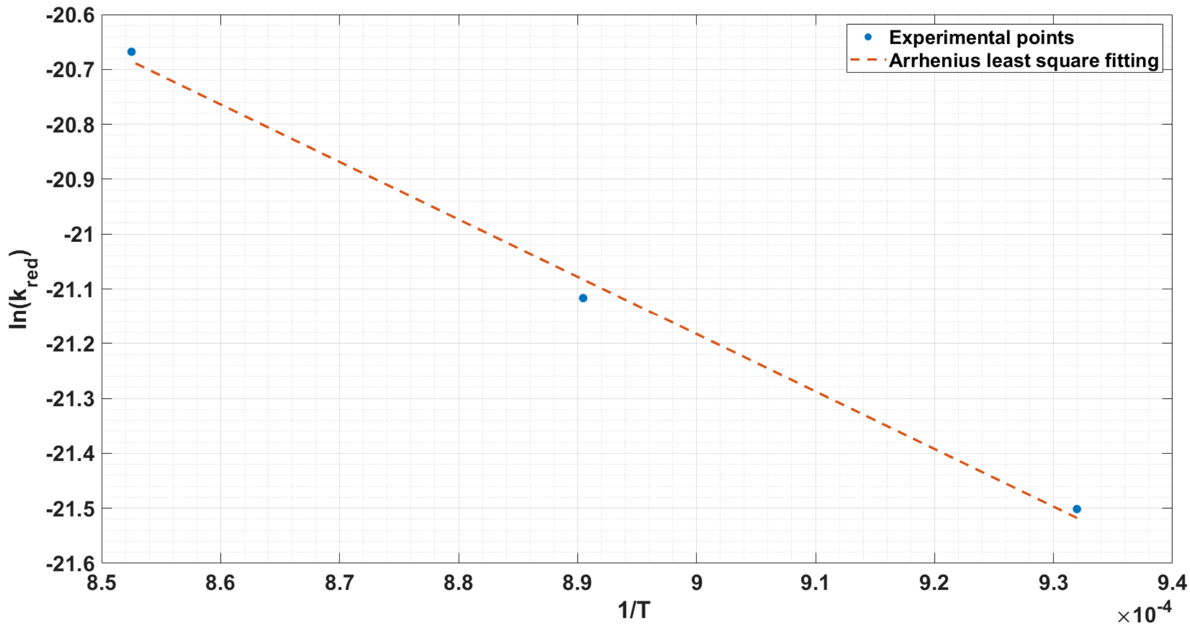

Figure 75- $ln\ (k_{red})$versus 1/T and the Arrhenius least square fitting, calculated using isothermal evaluation method.

Figure 76 and Figure 77 show the comparison between the two models and the experimental curves, considering three different heating rates. The fitting bad quality is mainly due to two factors:

- The weight variations are very small, and the data obtained are not sufficient, it would be useful to work with larger quantities and do more tests in order to have more precise kinetic constants.
- The reactions mechanism should be studied more in detail to verify the effective constancy of Arrhenius parameters throughout thermal decomposition.

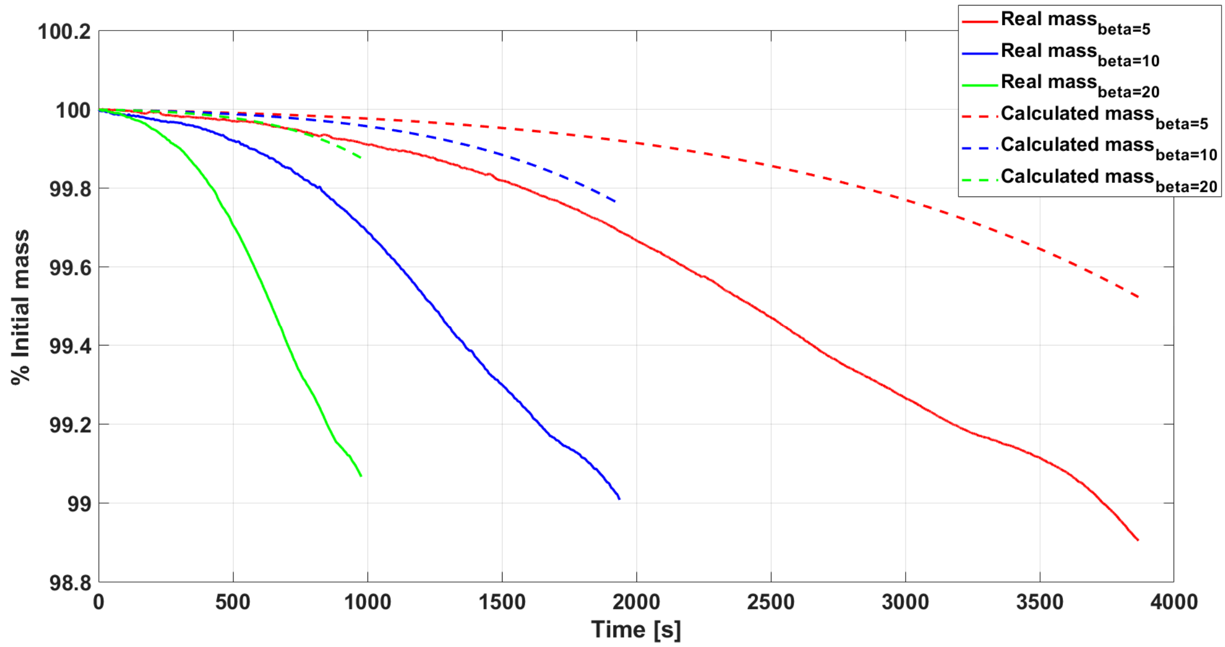

Figure 76-Comparison between the result from the isothermal model and the experimental curves, considering three different heating rates.

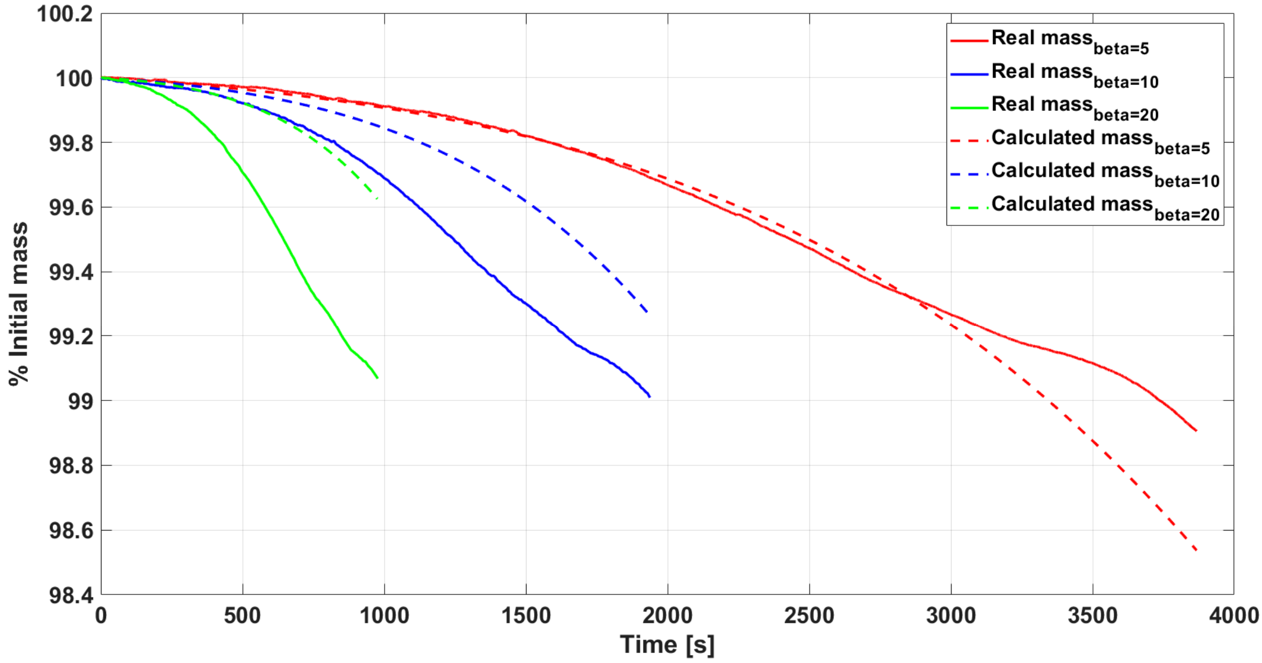

Figure 77-Comparison between the result from the non-isothermal model and the experimental curves, considering three different heating rates.

5.2.4.2 Oxidation step under air

The kinetic constants calculated through the non-isothermal approach are summarised in the Table 22.

Table 22- Arrhenius constants evaluated following the non-isothermal approach.

Non-isothermal approach			
$Cooling\ rate\ \left[\frac{°C}{min}\right]$	-5	-10	-20
$A'[s^{-1}]$	$1.4 * 10^{-8}$		
$E_a'\left[\frac{J}{mol}\right]$	32000		

Figure 78 shows the comparison between the experimental curves and the calculated patterns obtained with the Arrhenius parameters provided by the non-isothermal approach.

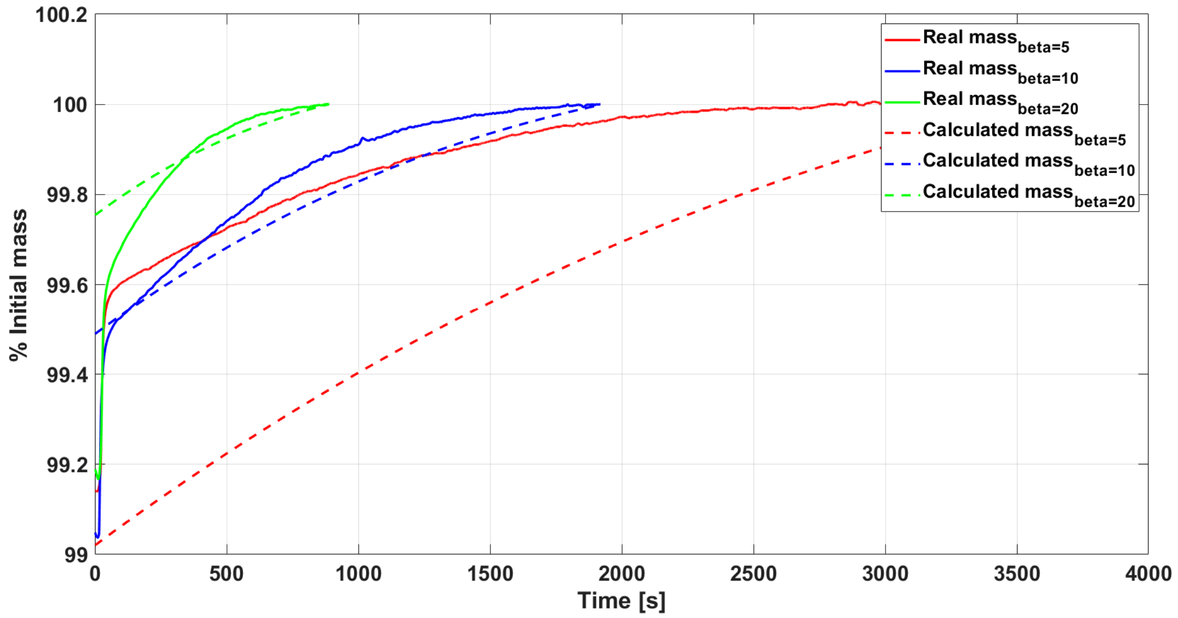

Figure 78-Comparison between the results from non-isothermal model and the experimental curves, considering three different heating rates.

Two out of three curves are well approximated by the model, but the fitting is poor for the points for lower time values.

Nonacceptable fitting results were achievable with the isothermal analysis, and therefore the obtained parameters can be considered not realistic for the process description. For this reason, they are not reported in this section.

5.2.5 Lab-scale cycle demonstration

A qualitative verification of the experimental and theoretical results was performed by a dedicated lab scale facility. The CSM 20 powders was inserted in a fixed bed reactor, represented in Figure 79.

Figure 79 Stainless steel fixed bed reactor

The scheme of the set-up is shown in the following Figure 80.

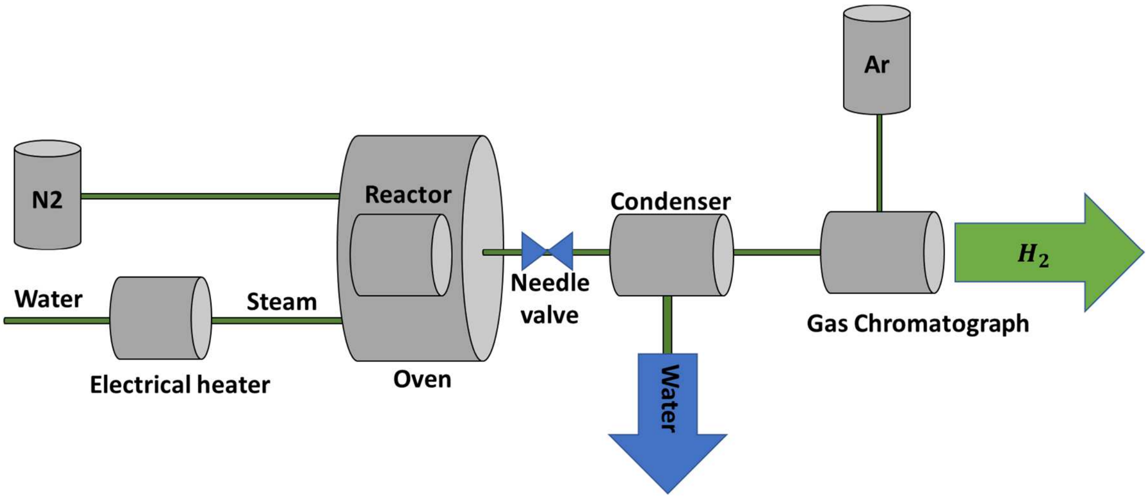

Figure 80-Scheme of the experimental facility used to perform the water splitting cycle with CSM 20.

The experimental analysis was carried out as the following:

- Nitrogen in flowed inside the reactor, which is at the same time heated up the TR temperature.
- Oxygen released is detected by a GC.

- Reactor is cooled down to the WS temperature.
- Water is vaporised, mixed with nitrogen, and injected into the reactor.
- Hydrogen production is followed by GC.

The reduction and the oxidation temperatures are chosen by the thermodynamic considerations illustrated in paragraph 5.2.3, and are, respectively, 950°C and 750°C.

During the heating process, up to the TR-temperature, it was detected a slow oxygen evolution which is started before reaching the set point temperature. Then, the reactor temperature was decreased of 200°C and water was flowed inside the system. After a certain time, due to the necessity of filling up the lines, hydrogen was produced. The whole oxidation reaction lasted for about 90 minutes. In Figure 81 the hydrogen production formation during the water shift is shown.

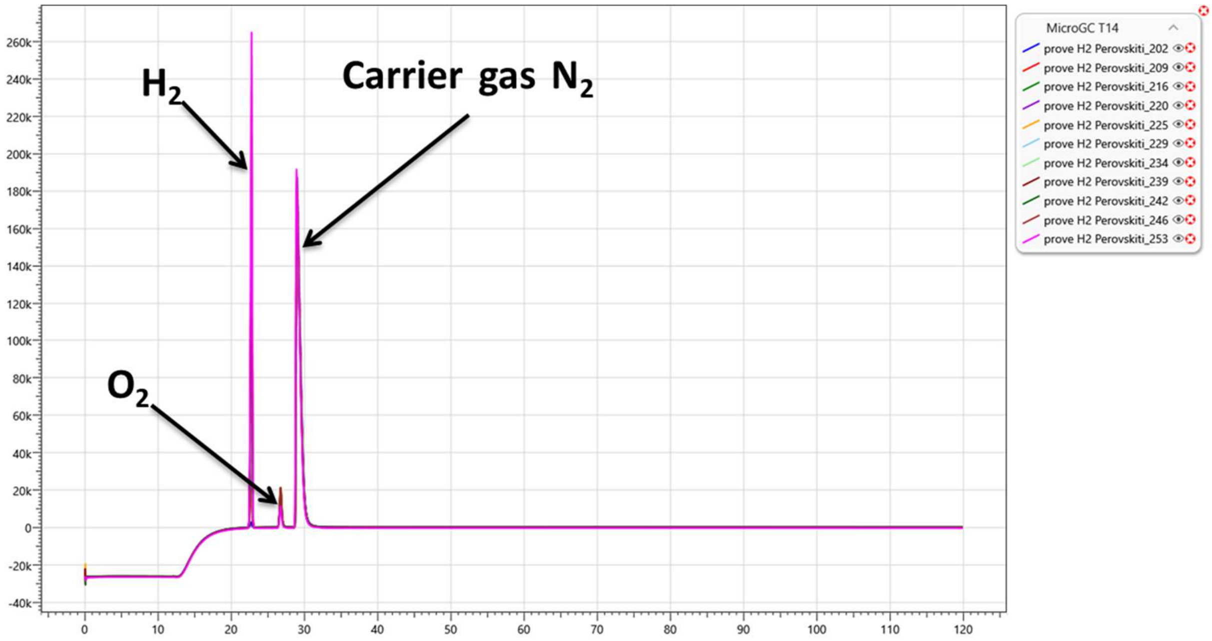

Figure 81- Hydrogen evolution during the water shift step detected by Gas Chromatography with a TCD detector.

Given the small quantities of formed hydrogen, it was not possible to perform a quantitative analysis, but the test results clearly demonstrate the feasibility of the cycle using the CSM 20 perovskite in this temperature range.

5.3 LSF: thermophysical, thermodynamic evaluation

This section addresses the partial results obtained for the LSF 20; in particular, specific heat, average enthalpy of reaction measurements and thermodynamic considerations are reported and discussed. All the methodologies employed are the same already illustrated and used for the CSM in the previous paragraphs.

5.3.1 Specific heat measurement

Ten independent tests were performed to determine the specific heat, using the same temperature program used for CSM, within a temperature range between 50 and 500 °C. The DSC patterns are illustrated in Figure 82.

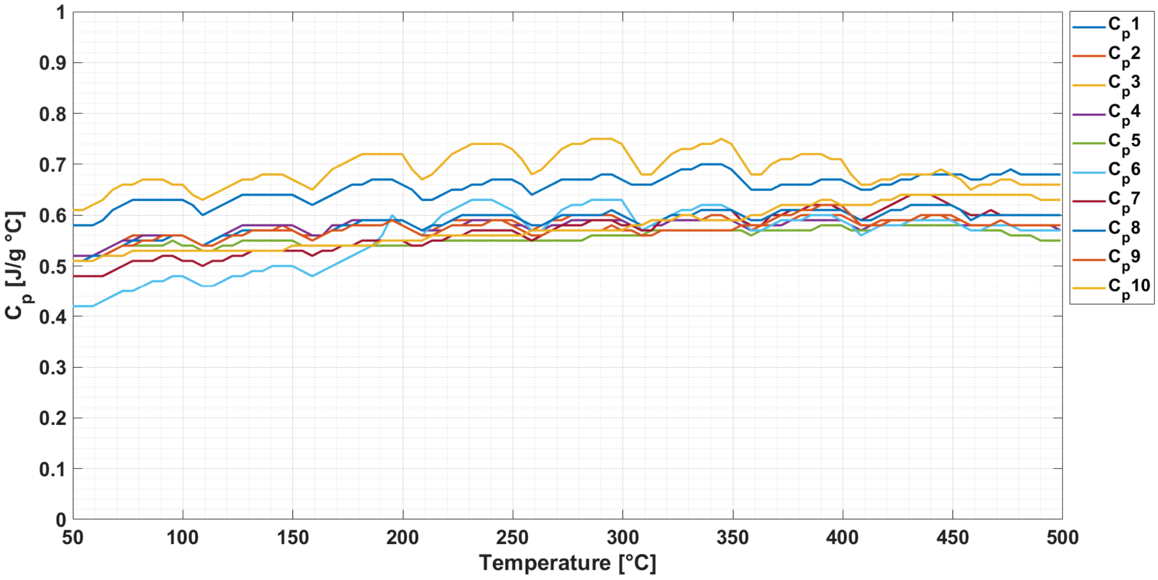

Figure 82- Overlaid DSC patterns of the LSF heat capacity between 50 and 500 °C

From this data set the average specific heat as function on temperature was evaluated and reported in Figure 83, with its error bar. The maximum error, evaluated with an interval of confidence of 99%, is about the 10%.

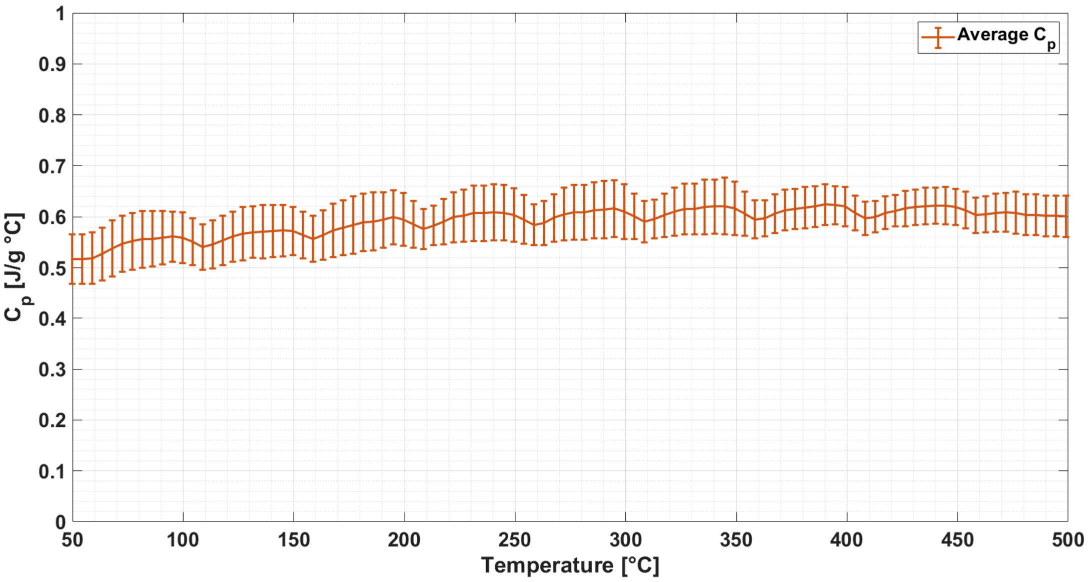

Figure 83- LSF average specific heat as function on temperature.

The result was linearly fitted as following:

$$Cp = 0.0002\,T + 0.54430$$

Where the Cp is expressed as $\left[\frac{J}{g\,°C}\right]$ and the Temperature as $[°\mathrm{C}]$. With respect to the specific heat of the CSM, it has a slightly greater dependence on temperature, however still not relevant.

5.3.2 Average enthalpy of reaction

Following the same test conditions used for the CSM, the sample was submitted to a temperature ramp from 300°C to 1000°C, with a heating rate of 20°C/min, under nitrogen, and then it was re-oxidated under air from 1000°C to 300°C, with a cooling rate of 20°C/min.

In the middle part of Figure 84 is reported the DTA analysis performed for the LSF. The average reaction enthalpy is measured by integrating the exothermic peaks between the temperature indicate in figure as left limit and right limit.

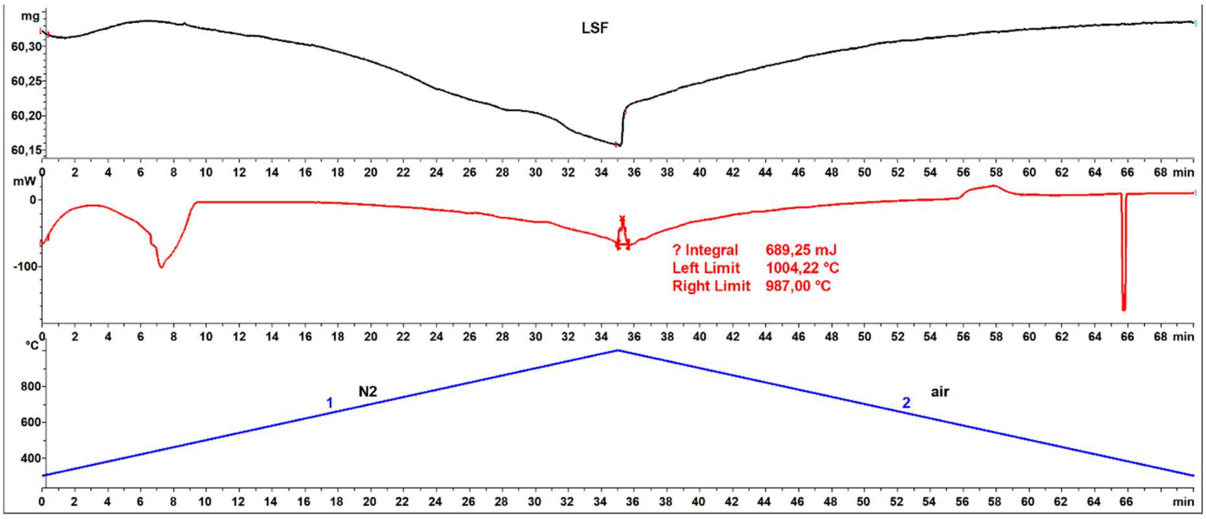

Figure 84- TGA/DTA analysis of LSF: the Figure shows, from top to bottom, the thermo-gravimetric pattern, the heat-flow and the temperature program used. The red line shows the reaction enthalpy measured by integrating the exothermic peaks between the temperature indicate in figure as left limit and right limit. Test carried out with a flow of 40 Nml/min of N2 (segment 1) and of 40 Nml/min of air (segment 2).

Also in this case, the reduction endothermic heat was not visible from the DTA analysis due to the slow time evolution of the reaction in time; this value can be assumed the same for the thermal reduction and for the water shift and can be taken equal to the one measured for the oxidation because reduction is the inverse reaction.

The obtained value is then adjusted through the external calibration curve (empirical fitting). The results are reported in Table 23.

Table 23 -LSF reaction enthalpy measured by DTA analysis.

Measured ΔH	689	mJ
mg of absorbed oxygen	0.05	mg
mmol of absorbed oxygen	0.0016	$mmol\ O2$
$Measured\ \Delta h$	441	$\frac{kJ}{molO_2}$
Extern calibration (Second-order polynomial)	$0.0120x^2 + 0.1764x + 22.0850$	-
$Adjusted\ \Delta h$	333	$\frac{kJ}{molO_2}$

5.3.3 Thermodynamic considerations

Following the same path done for the CSM, it was verified whether working with TGA instrument would achieve equilibrium conditions. To do this, the same powder tested in TGA was used to feed the batch-type reactor previously described, with the aim of directly measuring the partial pressure of oxygen at equilibrium at different temperatures.

These results showed that the equilibrium pressure was reached after a few moments when the temperature was kept constant, thus confirming the result obtained for CSM. Part of these analysis are summarized in Figure 85, in which is reported the evolution of pressure staring from 400°C to the isothermal condition at around 700°C. The same observation could be done for higher temperatures, obviously when the isothermal conditions are reached.

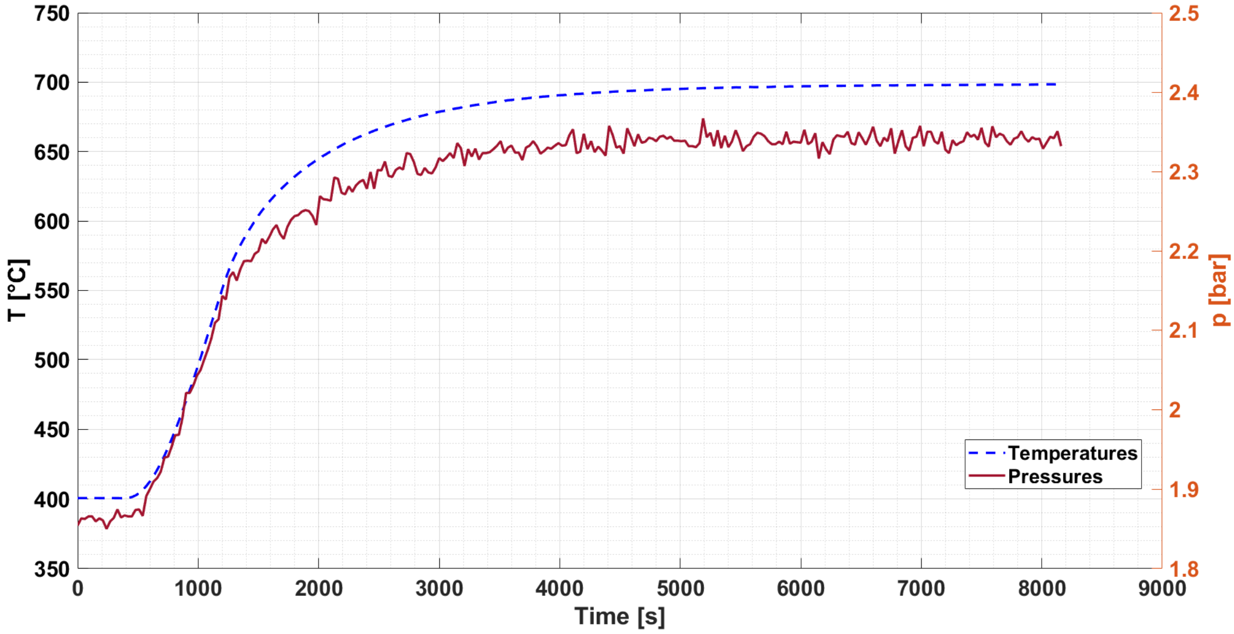

Figure 85-LSF: evolution of pressure staring from 400°C to the isothermal condition at around 700°C.

Then, decreasing oxygen partial pressure and maximum constant temperatures, reduction and oxidation cycles were performed to evaluate the thermodynamic behaviour of the LSF. The results of these TGA analysis are reported in Figure 86.

The differences between reactor and TGA analysis (within the experimental error) are due to temperature inhomogeneities in the powders inside the reactor, as already mentioned for the CSM. Also in this case, the obtained trend for the equilibrium δ, that is around the same for each temperature, confirmed what reported in the scientific literature: increasing PO_2, the equilibrium δ decreases.

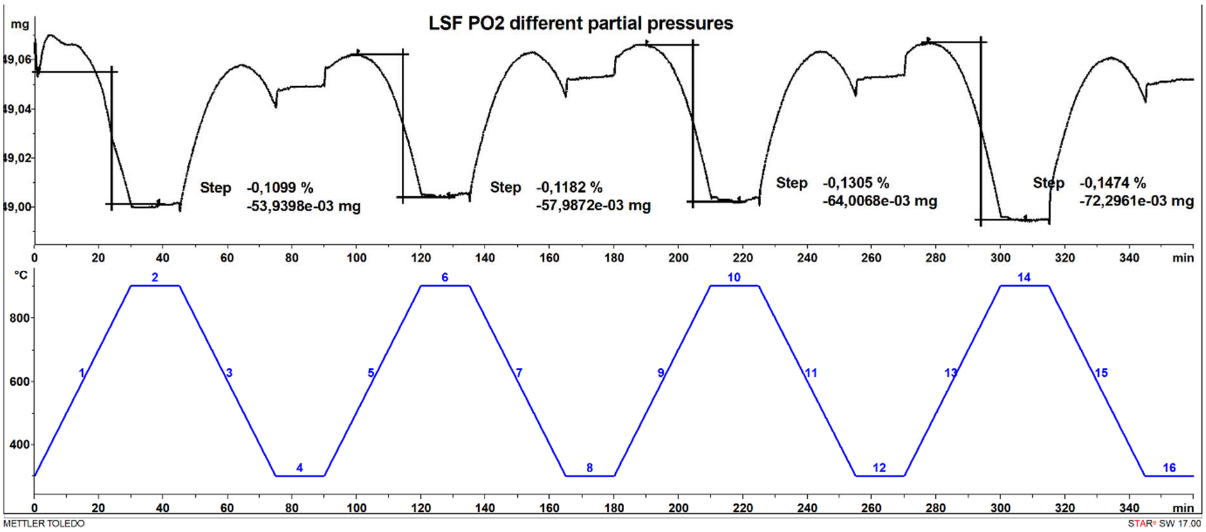

Figure 86- TGA/DTA analysis of LSF: the figure shows, from top to bottom, the thermo-gravimetric pattern and the temperature program used. Test carried out with a flow of 40 Nml/min of N2 (segments 1-2) and of 40 Nml/min of air (segments 3-4), varying oxygen partial pressure, from 0.2 bar to 0.025 bar and at maximum constant temperatures.

The technical specifications of all TGA analysis performed varying oxygen partial pressures are reported in Table 24.

Table 24- LSF: TGA analysis performed varying oxygen partial pressures.

	Temperature and Oxygen pressure program							
	1	2	3	4	5	6	7	8
$Nitrogen\ flow\ \left[\frac{mL}{min}\right]$	40	40	0	0	40	40	0	0
$Air\ flow\ \left[\frac{mL}{min}\right]$	0	0	40	40	0	0	40	40
$Heating\ rate\ \left[\frac{°C}{min}\right]$	20	0	-20	0	20	0	-20	0
$Temperature\ [°C]$	300-900	900	900-300	300	300-900	900	900-300	300
$pO_2\ [bar]$	0.2	0.2	0.2	0.2	0.1	0.1	0.2	0.2
	9	10	11	12	13	14	15	16
$Nitrogen\ flow\ \left[\frac{mL}{min}\right]$	40	40	0	0	40	40	0	0
$Air\ flow\ \left[\frac{mL}{min}\right]$	0	0	40	40	0	0	40	40
$Heating\ rate\ \left[\frac{°C}{min}\right]$	20	0	-20	0	20	0	-20	0
$Temperature\ [°C]$	300-900	900	900-300	300	300-900	900	900-300	300
$pO_2\ [bar]$	0.05	0.05	0.2	0.2	0.025	0.025	0.2	0.2

The relations between δ and pO_2 at fixed temperatures are represented in Figure 87.

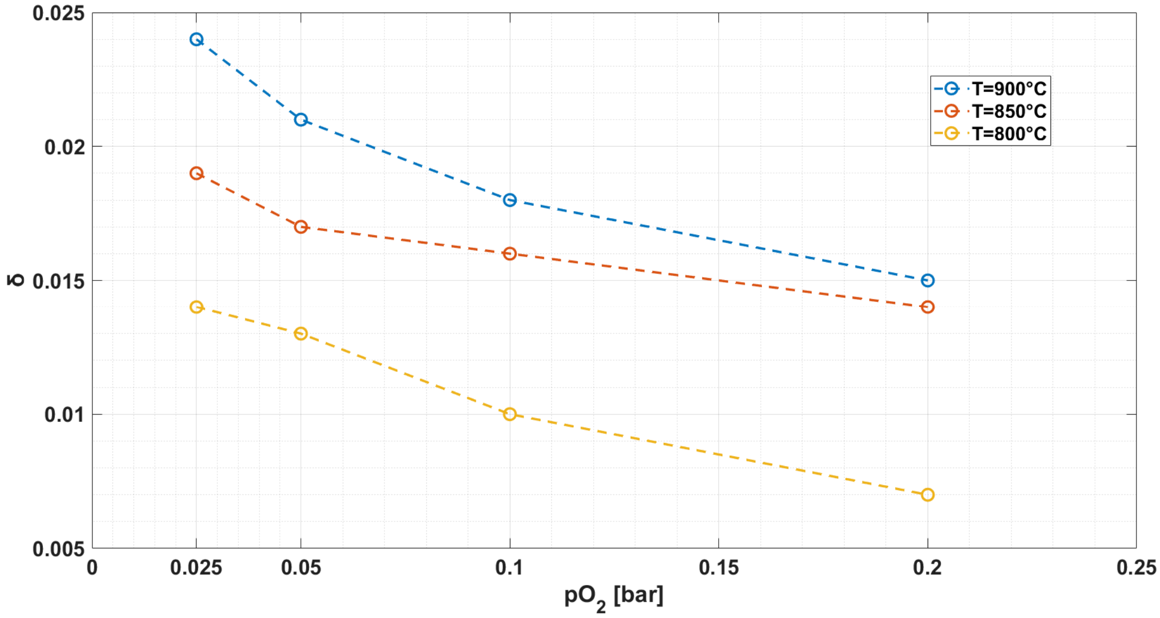

Figure 87- LSF: the graph shows the evolution of the equilibrium δ as a function of the imposed oxygen partial pressure for each temperature considered.

Exploiting the already described relation between $\Delta G^0_{reduction}$ and the pO$_2$, through the equilibrium constant K_{red} (Eq. 35),the ΔG^0_{Solid}, as function of pO$_2$ at fixed temperature, is calculated. The results are reported in Figure 88.

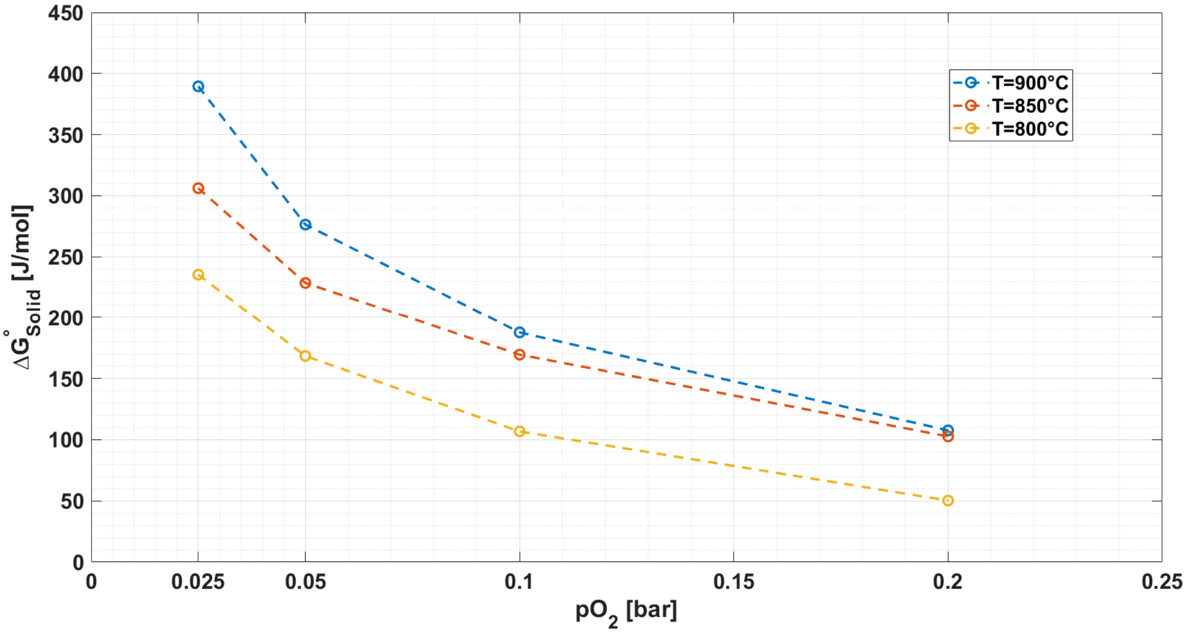

Figure 88-ΔG^0_{Solid}as a function of pO$_2$ at fixed temperatures.

Moreover, using the same empirical extrapolation method for the CSM, the minimum δ allowing the oxidation at selected fixed temperature, was calculated. The obtained results are summarised Table 25.

Table 25-LSF: minimum δ, referring to oxidation at a fixed temperature.

Temperature [°C]	$\delta_{minimum}$
800	0.14
850	0.18

With respect to CSM, the LSF delta reduction, compared to the one of the CSM at 900°C, is significantly lower. Furthermore, analysing in detail the data reported in Table 25 with the same obtained for the CSM, at the same temperature, even if the LSF requires minimum oxidation δ lower than CSM, they cannot be obtained from thermal reductions under 1000°C.

A possible solution to this problem is to operate with lower oxidation temperatures, probably under 650-600°C. However, this can be unaffordable for kinetic limitations. Further investigations are needed to confirm this hypothesis.

For these reasons, data collected for the LSF are lower with respect to CSM and further experimental analyses, such as kinetics and analysis in the experimental set-up, were not carried out for LSF in this context.

6 Process analysis: flow diagram evaluation

The experimental and theorical results described in the previous chapters showed the possibility to use the CSM perovskite in a two steps thermochemical cycle in the interval from 750°C to 950°C. In this paragraph, the obtained data are used to build a flow diagram, in order to estimate a realistic efficiency for a perovskite-based water splitting process, neglecting, for the time being, the issues related with the reaction kinetics.

Two different configurations are presented: one with partial internal heat recovery and one in which also the exothermic oxidation heat is exploited.

The net required thermal energy can be provided by a heliostat field, which concentrates the solar irradiation directly on a central solar receiver where the perovskite powder is flowed, whilst hydrogen is obtained by condensing the non-reacted water downstream the oxidation reactor.

All the mass and energy balances reported in the following sections are normalized to produce $1\ \frac{mol}{s}$ of hydrogen.

The thermochemical cycle is assumed to be performed involving two different circulating fluidized bed reactors [85]: one for the reduction, directly fed by the solar irradiation, and the second one, where the exothermic heat is removed by an air-cooling system.

6.1 Scheme with partial internal heat recovery (Scheme 1)

In Figure 89 is represented the flow diagram of the process with a partial internal heat recovery. For an easier comprehension, the scheme is divided in three main sub-sections:

- CSM loop
- Nitrogen loop
- Water-steam sub-section

For all the sub-sections is carried out a detailed description of the involved streams and are elaborated the molar and energy balances.

Table 26 reports the composition, temperature, pressure, and mass flow rate for each stream described in Figure 89, while the amount of heat recovered in the heat exchangers are illustrated in Table 27.

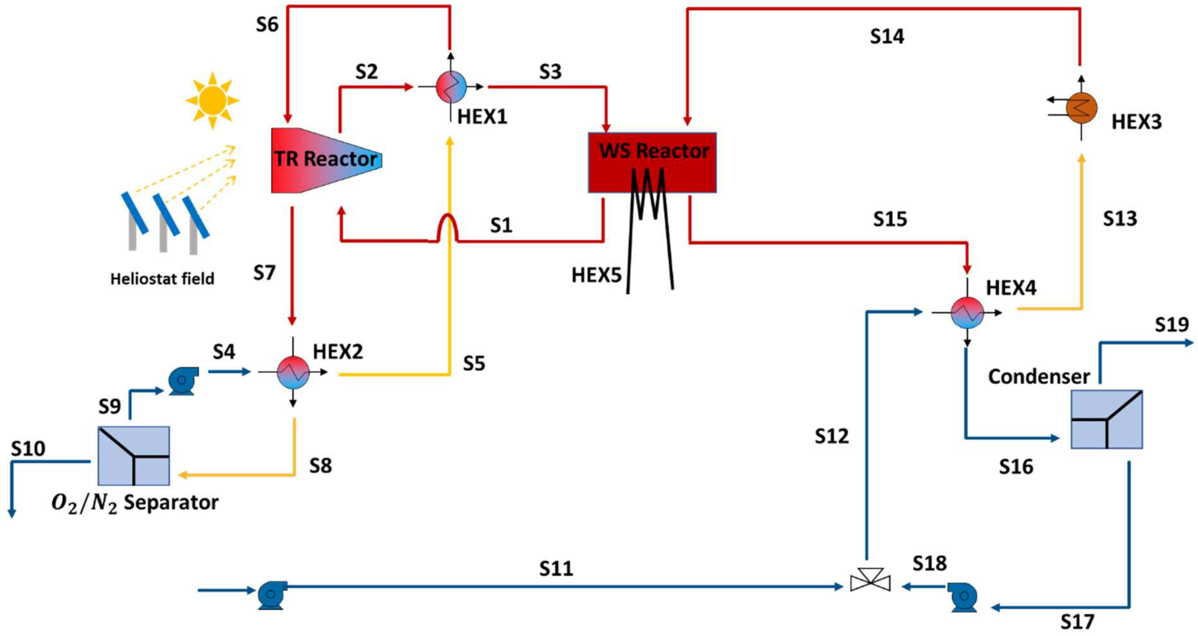

Figure 89 -Flow diagram of the solar driven TCWS cycle based on CSM (with partial internal heat recovery)

Table 26-Description of the stream of the flow diagram in Figure 89. Pressure is equal to 1bar in each stream.

Stream	N_2 $\left[\frac{mol}{s}\right]$	O_2 $\left[\frac{mol}{s}\right]$	H_2 $\left[\frac{mol}{s}\right]$	H_2O $\left[\frac{mol}{s}\right]$	$Ca_{0.8}Sr_{0.2}MnO_3$ $\left[\frac{mol}{s}\right]$	$Ca_{0.8}Sr_{0.2}MnO_{3-\delta}$ $\left[\frac{mol}{s}\right]$	T $[°C]$
S1	0	0	0	0	5.67	0	750
S2	0	0	0	0	0	5.67	950
S3	0	0	0	0	0	5.67	750
S4	13	0	0	0	0	0	25
S5	13	0	0	0	0	0	850
S6	13	0	0	0	0	0	900
S7	13	0.5	0	0	0	0	950
S8	13	0.5	0	0	0	0	175
S9	13	0	0	0	0	0	25
S10	0	0.5	0	0	0	0	25
S11	0	0	0	1	0	0	20
S12	0	0	0	2	0	0	20
S13	0	0	0	2	0	0	100
S14	0	0	0	2	0	0	750
S15	0	0	1	1	0	0	750
S16	0	0	1	1	0	0	150
S17	0	0	0	1	0	0	20
S18	0	0	0	1	0	0	20
S19	0	0	1	0	0	0	20

Table 27- Description of the heat recovery for each HEX present in the flow diagram of Figure 89.

	$HEX1$	$HEX2$	$HEX3$	$HEX4$	$HEX5$
$Heat\ exhanged$ $[kW]$	21.7	332.0	101.9	40.4	95

6.1.1 CSM Loop

According to the base reactions of the two step TCWS cycle based on CSM and normalized with respect to the hydrogen stochiometric coefficient, the water gas shift reaction can be written as follow:

$$WS\colon \frac{1}{\delta} Ca_{0.8}Sr_{0.2}MnO_{3-\delta} + H_2O \rightarrow \frac{1}{\delta} Ca_{0.8}Sr_{0.2}MnO_3 + H_2$$

The minimum solid amount employed to obtain a hydrogen flow of 1 $\frac{mol}{s}$ is $\frac{1}{\delta} mols$. Under the hypothesis of a continuous mode operation, the solid particles temperatures are always included between the TR temperature and the WS temperature, respectively 950°C and 750°C, chosen from the previously described thermodynamic considerations (section 5.2.3).

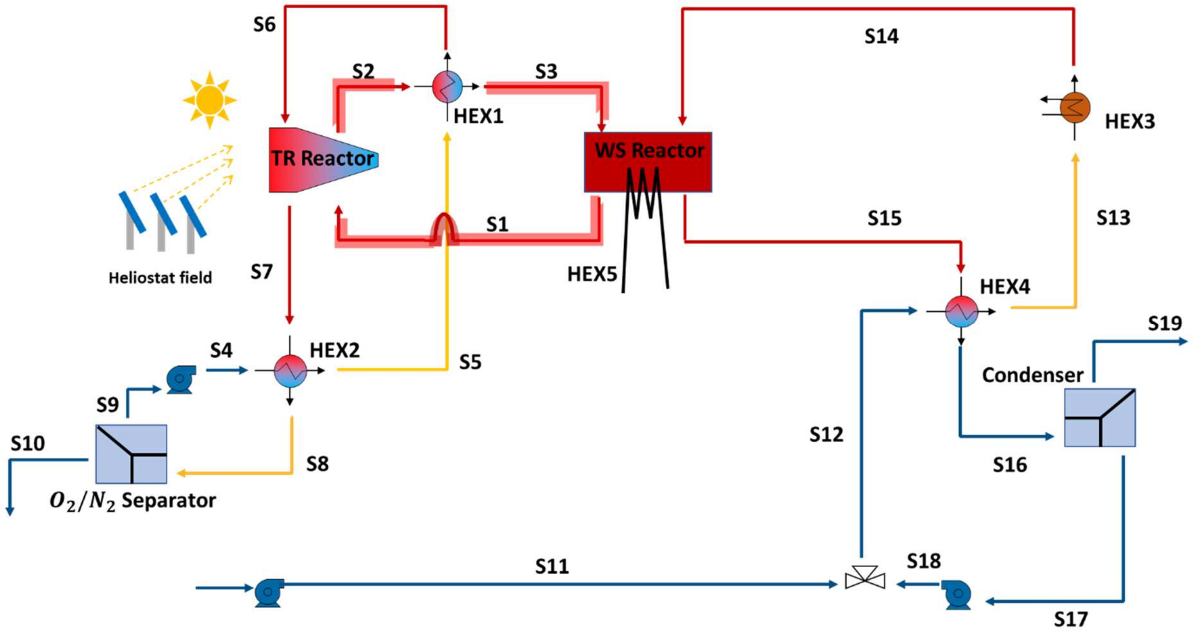

Figure 90-Detailed representation of the 'CSM loop' in the flow diagram of Figure 89

In Figure 90 is highlighted the CSM sub-section. Starting from stream 1, the powders are in their oxidized form and enter the reduction reactor, which is a central solar receiver, at 750°C. Here, through a heliostat field the solar radiation is directly concentrated on the powder, in order to increase the perovskite temperature up to the TR value and to provide the necessary endothermic enthalpy. At the reactor exit, stream 2, the solid is still at 950 °C and it needs be cooled to 750°C before the oxidation reactor. Between the two reactors is positioned a heat exchanger (HEX1), in which the solid available sensible enthalpy is used to preheat the nitrogen flow, which is then provided in the reduction reactor. The powder then leaves the HEX1 at 750°C, (stream 3) and enters the water shift reactor.

6.1.2 Nitrogen loop

A nitrogen flow is needed to remove the oxygen produced by the perovskite, from $Ca_{0.8}Sr_{0.2}MnO_3$ to $Ca_{0.8}Sr_{0.2}MnO_{3-\delta}$, and thus increase the reduction capability. This part of the process is detailed in Figure 91.

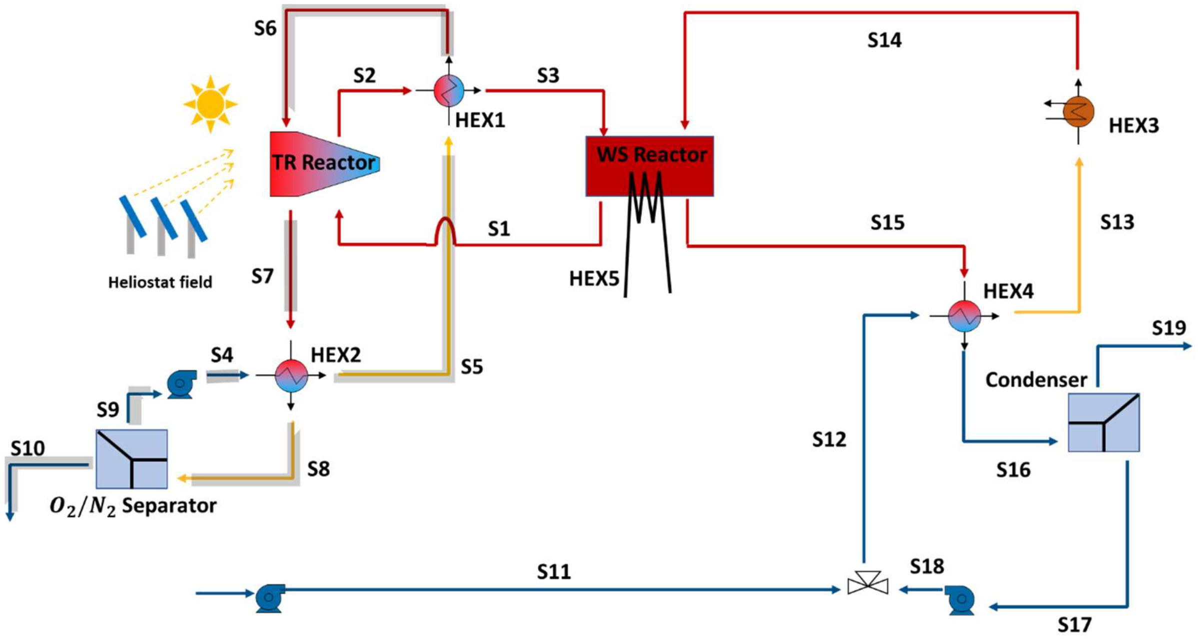

Figure 91-Detailed representation of the 'Nitrogen loop' in the flow diagram of Figure 89

Before entering the TR reactor, the nitrogen flow is pre-heated by two heat exchangers. The first one (HEX2) exploit part of the heat presented by nitrogen and oxygen leaving the solar receiver. The nitrogen temperature reached at the exit of HEX1, (stream 5) is around 850°C. Then, in HEX1 it is utilized some of the reduced solid sensible heat. Thanks to this additional heat supply, the nitrogen temperature of the stream 6 is around 900°C. The necessary extra heat to 950°C is provided by the heliostat field, directly inside the TR reactor.

The gas mixture that leaves the reactor, stream 7, is formed by nitrogen and the released oxygen $\left(\frac{1}{2}O_2\right)$. Due to its high temperature (950°C), it is used to feed the hot side of HEX2, from which it exits at a temperature of around 175°C.

Instead of being dispersed, the stream 8 is sent to an oxygen-nitrogen separator. The energetic cost in terms of electricity is considered of 200 $\frac{kWh}{ton\ of\ O_2}$, according to [96]. At the exit of the separator, stream 9, nitrogen is at room temperature and can be reintroduced in the stream 4, whilst oxygen (stream 10) is ejected from the system and can be stored, disposed or used for other purposes.

6.1.3 Water loop

The water required for the process is the sum of two contributions: the water used as reactant (stream 11), and the non-reacted recycled flow (stream 17 and 18). Through a three-way valve the two water streams are mixed together (stream 12) and then, they are sent to a heat exchanger (HEX4), in which part of the products (steam + hydrogen) heat is recovered. After the HEX4 (stream 13), the steam fraction is 35% and the temperature is 100°C, therefore, a heater is required to vaporise the remaining liquid and bring it to the WS reaction temperature. As a result, the stream 14, which enters the oxidation reactor, is at 750°C. Operating at temperature and stoichiometric conditions at which the WS equilibrium constant is unitary (see Chapter 5), one mol/sec of water is reacted to produce one mol/sec of hydrogen. Then, as already mentioned, the hydrogen and the unreacted steam (stream 15) are used to feed the hot side of the HEX4, from which they exit at 150°C (stream 16). At this point, the gas mixture is separated into its constituents through a condensation unit. The obtained water is recirculated while almost pure hydrogen (stream 19) can be stored or used for other purposes, such as to produce electricity. In case, all traces of water can be removed by another condensation unit.

This part of the cycle is reported in Figure 92.

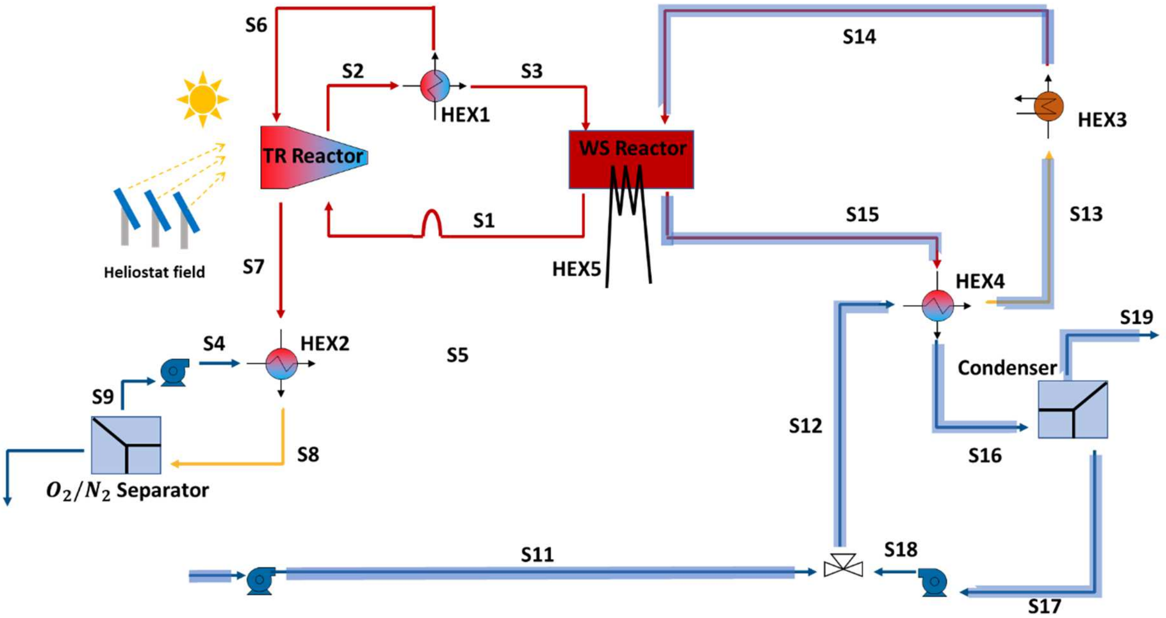

Figure 92-Detailed representation of the 'Water loop' in the flow diagram of Figure 89

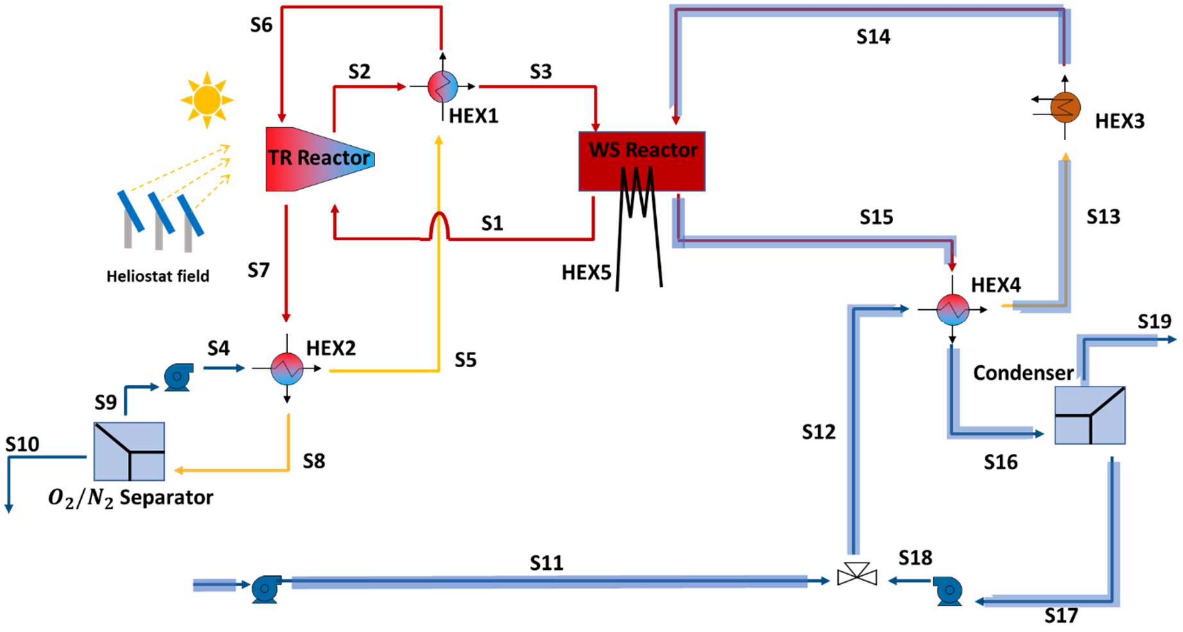

Figure 93- Detailed representation of the 'Water loop' in the flow diagram of Figure 89

6.2 Scheme with further heat recovery (Scheme 2)

Figure 94 reports the whole process where the exothermic reaction enthalpy is used in the HEX6 to bring the water stream from 100 to 474 °C. As a result, the stream 14 is totally vaporised.

This way, further 80 kW can be recovered, thus enhancing the overall process efficiency.

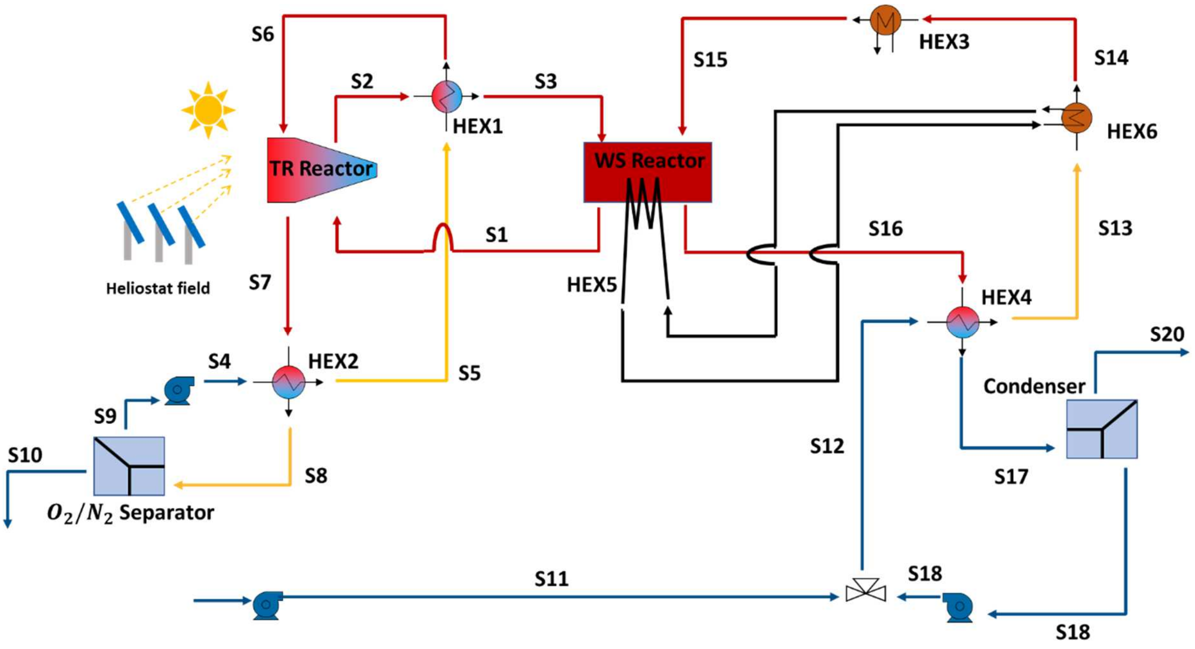

Figure 94- Flow diagram of the solar driven TCWS cycle based on CSM (with further internal heat recovery

6.3 Process efficiency

Table 28 reports all the interval heat recovered, the necessary auxiliary heat, and the thermal efficiency for each of the considered scheme.

Table 28- Results of the energy balances of the two presented scheme and thermal efficiency calculation.

Scheme	Internal heat recovery $[kW]$	Auxiliary heat $[kW]$	Solar heat requirement $[kW]$	Electrical work for the $N_2 - O_2$ separation	Thermal efficiency [%]
	HEX1+HEX2+HEX4	HEX3	Q_{sol}	Wel	$\eta = \frac{LHV(H_2)}{Q_{sol} + auxiliary + 2.5 * Wel}$
1	394	101.8	290	11.5	58
2	394	21.9	290	11.5	71

It Is worth mentioning that the composition of the Solar heat requirement, (Q_{sol}), is the sum of three quantities: the endothermic reduction heat, the heat required by the perovskite to be heated from the WS-temperature to the TR-temperature and the heat requested from nitrogen to be heated up to TR-temperature from the temperature of the stream 6. The auxiliary heat (HEX3) could be provided by green energy sources.

In particular, thermal efficiency was calculated dividing the hydrogen lower heating value, $242 \frac{kJ}{mol}$ [97], by the net heat requirement of the process.

The obtained values are, respectively, 58% for the first configuration and 72% for the second one.

Clearly, considering the overall thermal efficiency, the more heat recoveries are present the better results are achieved; on the other hand, increasing the number of heat exchangers also worsen the plant complexity and cost. Therefore, subsequent evaluations will be necessary to assess whether the cost with recovery is compensable by the efficiency gain.

At any rate, in both cases the calculated efficiency is quite competitive in comparison with the values reported for other currently proposed two steps thermochemical water splitting cycles. Some of these values are summarized in Table 29

Table 29-Efficiency of some TCWS cycle for hydrogen production

$TCWS\ cycle$	$Efficiency$ [%]
$ZnO/Zn\ based\ (optimized)$	~ 50 [98]
$SnO_2/SnO\ based$	~ 50 [99]
$Sm_2O_3/Sm\ based$	~ 30 [100]

In [98]–[100], the solar-to-fuel efficiency also included the efficiency of the solar reactors, which are considered as ideal cavities (Eq. 13). Considering the parameters used in the scientific literature for the calculation of reactor efficiencies, for the temperature levels hypothesized in this work, this efficiency is around the 97%, even higher. Therefore, the values reported in Table 28, including these values, do not change significantly and can be considered realistic for the whole process.

7 Conclusions and perspectives

The focus of this thesis work is concerned with the development of mixed oxides as chemical intermediate materials for green water splitting. All the aspects related to perovskite preparation, characterization and reactivities have been addressed with the aim to validate suitable procedures for further investigations. Part of the work has been innovative with respect to the current state of the art. The experimental results have been qualitative verified by lab-scale set-up and used to perform a preliminary flow sheeting analysis, to estimate an upper realistic limit for the water splitting process efficiency.

The obtained results show that perovskites are quite promising materials in terms of preparation cost, given they can be synthesized starting from cost effective precursors. Moreover, they demonstrate good redox properties, consequently they can be employed below 1000°C, which is a practical limit for operating efficiently with CSP.

The main drawback is their limited reaction extent, which leads to the necessity to use large amount of solid with respect to the produced hydrogen.

In any case, there are several points that still should be further investigated: the reactions kinetics, the material thermal cyclability and a thermodynamic model able to better describe the physical mechanism of the molecular processes.

Another important issue is represented by the improvement of the synthesis method, trying different methodologies from the HEBM, described in this work.

As far as the process models are concerned, it will be useful to carry on the flow sheeting analysis using more realistic and accurate schemes, and to include a tecno-economic analysis, in order to be able to compare the feasibility of this technology with currently commercial methods for hydrogen production, such as water electrolysis. Finally, it will be very important to study these systems also in the context of the hydrogen storage, with the aim to improve the hydrogen dispatchability.

8 Nomenclature

ENEA	Agenzia nazionale per le nuove tecnologie, l'energia e lo sviluppo economico sostenibile
MASE	Ministero dell’ambiente e della sicurezza energetica
PNRR	Piano nazionale di ripresa e resilienza
EU	European Union
CSP	Concentrating solar plants
TWSC	Thermochemical water-splitting cycles
XRD	X-ray diffraction
TGA	Thermogravimetric analysis
DSC	Differential scanning calorimetry
SEM	Scanning electron microscopy
GHGs	Greenhouse gases
RES	Renewable energy systems
HTF	Heat transfer media
LCOE	Levelized cost of energy
SPD	Solar-Parabolic Dish
PTC	Parabolic Trough Collector
SMR	Methane steam reforming
CCS	Carbon capture system
CCUS	Carbon capture, utilization, and storage system
LTE	Low Temperature Electrolysis
HTE	High Temperature Electrolysis
AWE	Alkaline Water Electrolyser
PEMWE	Proton Exchange Membrane Water Electrolysers

Bibliography

[1] bp, “Statistical Review of World Energy 2022.”

[2] “Sintesi per tutti Cambiamento Climatico 2021.”

[3] “2020 on track to be one of three warmest years on record,” Dec. 02, 2020. https://public.wmo.int/en/media/press-release/2020-track-be-one-of-three-warmest-years-record (accessed Jan. 28, 2023).

[4] “Effetti del cambiamento climatico.” https://unric.org/it/effetti-del-cambiamento-climatico/ (accessed Jan. 28, 2023).

[5] I. Renewable Energy Agency, *World Energy Transitions Outlook 2022: 1.5°C Pathway*. 2022. [Online]. Available: www.irena.org

[6] “Renewables share of power generation in the Net Zero Scenario, 2010-2030,” Oct. 26, 2022. https://www.iea.org/data-and-statistics/charts/renewables-share-of-power-generation-in-the-net-zero-scenario-2010-2030 (accessed Jan. 28, 2023).

[7] “Renewable Energy Finance Flows.” https://www.irena.org/Data/View-data-by-topic/Finance-and-Investment/Renewable-Energy-Finance-Flows (accessed Mar. 07, 2023).

[8] J. H. Norman, G. E. Besenbruch, L. C. Brown, and C. L. Allen, “DISCLAIMER.”

[9] B. en Zalba, J. M. Mar ı ın, L. F. Cabeza, and H. Mehling, “Review on thermal energy storage with phase change: materials, heat transfer analysis and applications.” [Online]. Available: www.elsevier.com/locate/apthermeng

[10] K. el Alami, M. Asbik, and H. Agalit, “Identification of natural rocks as storage materials in thermal energy storage (TES) system of concentrated solar power (CSP) plants – A review,” *Solar Energy Materials and Solar Cells*, vol. 217, Nov. 2020, doi: 10.1016/j.solmat.2020.110599.

[11] I. Renewable Energy Agency, *Renewable power generation costs in 2021*. 2022. [Online]. Available: www.irena.org

[12] A. Bilal Awan, M. N. Khan, M. Zubair, and E. Bellos, “Commercial parabolic trough CSP plants: Research trends and technological advancements,” *Solar Energy*, vol. 211. Elsevier Ltd, pp. 1422–1458, Nov. 15, 2020. doi: 10.1016/j.solener.2020.09.072.

[13] M. T. Islam, N. Huda, A. B. Abdullah, and R. Saidur, “A comprehensive review of state-of-the-art concentrating solar power (CSP) technologies: Current status and research trends,” *Renewable and Sustainable Energy Reviews*, vol. 91. Elsevier Ltd, pp. 987–1018, Aug. 01, 2018. doi: 10.1016/j.rser.2018.04.097.

[14] “India’s PV-led solar growth casts eyes on performance of CSP projects,” Nov. 09, 2015. https://www.reutersevents.com/renewables/csp-today/markets/indias-pv-led-solar-growth-casts-eyes-performance-csp-projects (accessed Jan. 29, 2023).

[15] “Solar Two Tower System,” May 2016, Accessed: Jan. 29, 2023. [Online]. Available: https://www.energy.gov/eere/solar/articles/solar-two-tower-system

[16] "Hydrogen." https://www.enelgreenpower.com/learning-hub/renewable-energies/hydrogen (accessed Jan. 29, 2023).

[17] "Hydrogen Details." https://www.alakai.com/hydrogen-details (accessed Jan. 29, 2023).

[18] "IDROGENO: proprieta'."

[19] "RACCOMANDAZIONE DI SICUREZZA RS23-Proprietà e rischi dell'idrogeno." [Online]. Available: www.eiga.org:

[20] J. Huang, P. Balcombe, and Z. Feng, "Technical and economic analysis of different colours of producing hydrogen in China," *Fuel*, vol. 337, Apr. 2023, doi: 10.1016/j.fuel.2022.127227.

[21] R. S. El-Emam, H. Ozcan, and C. Zamfirescu, "Updates on promising thermochemical cycles for clean hydrogen production using nuclear energy," *J Clean Prod*, vol. 262, Jul. 2020, doi: 10.1016/j.jclepro.2020.121424.

[22] A. Mohammadi and M. Mehrpooya, "A comprehensive review on coupling different types of electrolyzer to renewable energy sources," *Energy*, vol. 158, pp. 632–655, Sep. 2018, doi: 10.1016/j.energy.2018.06.073.

[23] T. Amirthan and M. S. A. Perera, "The role of storage systems in hydrogen economy: A review," *J Nat Gas Sci Eng*, vol. 108, p. 104843, Dec. 2022, doi: 10.1016/j.jngse.2022.104843.

[24] H. Barthelemy, M. Weber, and F. Barbier, "Hydrogen storage: Recent improvements and industrial perspectives," *Int J Hydrogen Energy*, vol. 42, no. 11, pp. 7254–7262, Mar. 2017, doi: 10.1016/j.ijhydene.2016.03.178.

[25] A. Ozarslan, "Large-scale hydrogen energy storage in salt caverns," *Int J Hydrogen Energy*, vol. 37, no. 19, pp. 14265–14277, Oct. 2012, doi: 10.1016/j.ijhydene.2012.07.111.

[26] *18TH World hydrogen energy conference 2010 : WHEC 2010 proceedings*. Forschungszentrum Jülich, 2010.

[27] "The Paris Agreement Related news Related Documents Related links What is the Paris Agreement?" https://unfccc.int/process-and-meetings/the-paris-agreement/the-paris-agreement (accessed Jan. 29, 2023).

[28] "IT IT COMMISSIONE EUROPEA Bruxelles, 8.7.2020 COM(2020) 301 final COMUNICAZIONE DELLA COMMISSIONE AL PARLAMENTO EUROPEO, AL CONSIGLIO, AL COMITATO ECONOMICO E SOCIALE EUROPEO E AL COMITATO DELLE REGIONI Una strategia per l'idrogeno per un'Europa climaticamente neutra." [Online]. Available: https://www.eu2018.at/calendar-events/political-

[29] "PIANO NAZIONALE DI RIPRESA E RESILIENZA #NEXTGENERATIONITALIA."

[30] V. K. Budama, J. P. Rincon Duarte, M. Roeb, and C. Sattler, "Potential of solar thermochemical water-splitting cycles: A review," *Solar Energy*, vol. 249, pp. 353–366, Jan. 2023, doi: 10.1016/j.solener.2022.11.001.

[31] A. Giaconia, M. de Falco, G. Caputo, R. Grena, P. Tarquini, and L. Marrelli, "Solar steam reforming of natural gas for hydrogen production using molten salt heat carriers," *AIChE Journal*, vol. 54, no. 7, pp. 1932–1944, Jul. 2008, doi: 10.1002/aic.11510.

[32] D. Mehanovic, A. Al-Haiek, P. Leclerc, D. Rancourt, L. Fréchette, and M. Picard, “Energetic, GHG, and economic analyses of electrified steam methane reforming using conventional reformer tubes,” *Energy Convers Manag*, vol. 276, Jan. 2023, doi: 10.1016/j.enconman.2022.116549.

[33] M. [Steinberg, “Fossil fuel decarbonization technology for mitigating global warming.”

[34] N. A. K. Aramouni, J. G. Touma, B. A. Tarboush, J. Zeaiter, and M. N. Ahmad, “Catalyst design for dry reforming of methane: Analysis review,” *Renewable and Sustainable Energy Reviews*, vol. 82. Elsevier Ltd, pp. 2570–2585, Feb. 01, 2018. doi: 10.1016/j.rser.2017.09.076.

[35] B. Christian Enger, R. Lødeng, and A. Holmen, “A review of catalytic partial oxidation of methane to synthesis gas with emphasis on reaction mechanisms over transition metal catalysts,” *Applied Catalysis A: General*, vol. 346, no. 1–2. pp. 1–27, Aug. 31, 2008. doi: 10.1016/j.apcata.2008.05.018.

[36] “Improving Coal Gasification Technology.” https://caer.uky.edu/power-generation/coal-gasification/#:~:text=The%20Department%20of%20Energy%20says,often%20just%20above%2030%20percent. (accessed Feb. 05, 2023).

[37] L. Jiang *et al.*, “Coal decarbonization: A state-of-the-art review of enhanced hydrogen production in underground coal gasification,” *Energy Reviews*, vol. 1, no. 1, p. 100004, Sep. 2022, doi: 10.1016/j.enrev.2022.100004.

[38] I. - International Energy Agency, “Global Hydrogen Review 2021.” [Online]. Available: www.iea.org/t&c/

[39] S. Biswas, G. Kaur, G. Paul, and S. Giddey, “A critical review on cathode materials for steam electrolysis in solid oxide electrolysis,” *International Journal of Hydrogen Energy*. Elsevier Ltd, 2023. doi: 10.1016/j.ijhydene.2022.11.307.

[40] S. Becker and V. Karri, “Predictive models for PEM-electrolyzer performance using adaptive neuro-fuzzy inference systems,” in *International Journal of Hydrogen Energy*, Sep. 2010, vol. 35, no. 18, pp. 9963–9972. doi: 10.1016/j.ijhydene.2009.11.060.

[41] S. Hu *et al.*, “A comprehensive review of alkaline water electrolysis mathematical modeling,” *Appl Energy*, vol. 327, Dec. 2022, doi: 10.1016/j.apenergy.2022.120099.

[42] S. Sebbahi, N. Nabil, A. Alaoui-Belghiti, S. Laasri, S. Rachidi, and A. Hajjaji, “Assessment of the three most developed water electrolysis technologies: Alkaline Water Electrolysis, Proton Exchange Membrane and Solid-Oxide Electrolysis,” *Mater Today Proc*, vol. 66, pp. 140–145, Jan. 2022, doi: 10.1016/j.matpr.2022.04.264.

[43] D. S. Falcão and A. M. F. R. Pinto, “A review on PEM electrolyzer modelling: Guidelines for beginners,” *Journal of Cleaner Production*, vol. 261. Elsevier Ltd, Jul. 10, 2020. doi: 10.1016/j.jclepro.2020.121184.

[44] S. Shiva Kumar and V. Himabindu, “Hydrogen production by PEM water electrolysis – A review,” *Materials Science for Energy Technologies*, vol. 2, no. 3. KeAi Communications Co., pp. 442–454, Dec. 01, 2019. doi: 10.1016/j.mset.2019.03.002.

[45] M. B. Karimi, F. Mohammadi, and K. Hooshyari, “Recent approaches to improve Nafion performance for fuel cell applications: A review,” *International Journal of Hydrogen Energy*,

vol. 44, no. 54. Elsevier Ltd, pp. 28919–28938, Nov. 05, 2019. doi: 10.1016/j.ijhydene.2019.09.096.

[46] N. Gokon, T. Suda, and T. Kodama, “Oxygen and hydrogen productivities and repeatable reactivity of 30-mol%-Fe-, Co-, Ni-, Mn-doped CeO2-δ for thermochemical two-step water-splitting cycle,” *Energy*, vol. 90, pp. 1280–1289, 2015, doi: 10.1016/j.energy.2015.06.085.

[47] A. Boretti, “Which thermochemical water-splitting cycle is more suitable for high-temperature concentrated solar energy?,” *Int J Hydrogen Energy*, vol. 47, no. 47, pp. 20462–20474, Jun. 2022, doi: 10.1016/j.ijhydene.2022.04.159.

[48] X. Li, X. Sun, Q. Song, Z. Yang, H. Wang, and Y. Duan, “A critical review on integrated system design of solar thermochemical water-splitting cycle for hydrogen production,” *International Journal of Hydrogen Energy*, vol. 47, no. 79. Elsevier Ltd, pp. 33619–33642, Sep. 15, 2022. doi: 10.1016/j.ijhydene.2022.07.249.

[49] L. E. Bv, S. Spewock, and C. J. Warde, “THE WESTINGHOUSE SULFUR CYCLE FOR THE THERMOCHEMICAL DECOMPOSITION OF WATER,” Pergamon Press, 1977.

[50] A. Demont and S. Abanades, “Solar thermochemical conversion of CO2 into fuel via two-step redox cycling of non-stoichiometric Mn-containing perovskite oxides,” *J Mater Chem A Mater*, vol. 3, no. 7, pp. 3536–3546, Feb. 2015, doi: 10.1039/c4ta06655c.

[51] R. R. Bhosale, G. Takalkar, P. Sutar, A. Kumar, F. AlMomani, and M. Khraisheh, “A decade of ceria based solar thermochemical H2O/CO2 splitting cycle,” *Int J Hydrogen Energy*, pp. 34–60, Jan. 2019, doi: 10.1016/j.ijhydene.2018.04.080.

[52] S. Abanades and G. Flamant, “Thermochemical hydrogen production from a two-step solar-driven water-splitting cycle based on cerium oxides,” *Solar Energy*, vol. 80, no. 12, pp. 1611–1623, Dec. 2006, doi: 10.1016/j.solener.2005.12.005.

[53] L. Xiao, S. Y. Wu, and Y. R. Li, “Advances in solar hydrogen production via two-step water-splitting thermochemical cycles based on metal redox reactions,” *Renewable Energy*, vol. 41. pp. 1–12, May 2012. doi: 10.1016/j.renene.2011.11.023.

[54] A. Steinfeld, “Solar hydrogen production via a two-step water-splitting thermochemical cycle based on Zn=ZnO redox reactions,” 2002. [Online]. Available: www.elsevier.com/locate/ijhydene

[55] R. R. Bhosale, A. Kumar, and P. Sutar, “Thermodynamic analysis of solar driven SnO2/SnO based thermochemical water splitting cycle,” *Energy Convers Manag*, vol. 135, pp. 226–235, 2017, doi: 10.1016/j.enconman.2016.12.067.

[56] J. H. Norman, K. J. Mysels, R. Sharp, and D. Williamson, “Studies of the sulfur-iodine thermochemical water-splitting cycle,” *Int J Hydrogen Energy*, vol. 7, no. 7, pp. 545–556, Jan. 1982, doi: 10.1016/0360-3199(82)90035-0.

[57] D. Oudejans, M. Offidani, A. Constantinou, S. Albonetti, N. Dimitratos, and A. Bansode, “Comprehensive Review on Two-Step Thermochemical Water Splitting for Hydrogen Production in a Redox Cycle,” *Energies*, vol. 15, no. 9. MDPI, May 01, 2022. doi: 10.3390/en15093044.

[58] L. G. Tejuca, J. Luis, G. Fierro, and J. M. D. Tascdn, “Structure and Reactivity of Perovskite-Type Oxides,” 1989.

[59] D. Oudejans, M. Offidani, A. Constantinou, S. Albonetti, N. Dimitratos, and A. Bansode, “Comprehensive Review on Two-Step Thermochemical Water Splitting for Hydrogen Production in a Redox Cycle,” *Energies*, vol. 15, no. 9. MDPI, May 01, 2022. doi: 10.3390/en15093044.

[60] D. Yadav and R. Banerjee, “A review of solar thermochemical processes,” *Renewable and Sustainable Energy Reviews*, vol. 54. Elsevier Ltd, pp. 497–532, Feb. 01, 2016. doi: 10.1016/j.rser.2015.10.026.

[61] Y. Mao *et al.*, “Hydrogen production via a two-step water splitting thermochemical cycle based on metal oxide – A review,” *Applied Energy*, vol. 267. Elsevier Ltd, Jun. 01, 2020. doi: 10.1016/j.apenergy.2020.114860.

[62] Q. Zhu, Y. Zhang, Z. Wang, X. Lin, J. Zhou, and K. Cen, “Thermochemical dissociation of water and carbon dioxide via ZnSI cycle for hydrogen and carbon monoxide production,” in *Energy Procedia*, 2012, vol. 29, pp. 738–743. doi: 10.1016/j.egypro.2012.09.086.

[63] A. Steinfeld, “Solar thermochemical production of hydrogen - A review,” *Solar Energy*, vol. 78, no. 5, pp. 603–615, May 2005, doi: 10.1016/j.solener.2003.12.012.

[64] M. Romero and A. Steinfeld, “Concentrating solar thermal power and thermochemical fuels,” *Energy and Environmental Science*, vol. 5, no. 11. pp. 9234–9245, Nov. 2012. doi: 10.1039/c2ee21275g.

[65] I. Al-Shankiti, B. D. Ehrhart, and A. W. Weimer, “Isothermal redox for H2O and CO2 splitting – A review and perspective,” *Solar Energy*, vol. 156, pp. 21–29, Nov. 2017, doi: 10.1016/j.solener.2017.05.028.

[66] T. Kodama *et al.*, “Flux measurement of a new beam-down solar concentrating system in Miyazaki for demonstration of thermochemical water splitting reactors,” in *Energy Procedia*, 2014, vol. 49, pp. 1990–1998. doi: 10.1016/j.egypro.2014.03.211.

[67] N. Gokon, S. Takahashi, H. Yamamoto, and T. Kodama, “Thermochemical two-step water-splitting reactor with internally circulating fluidized bed for thermal reduction of ferrite particles,” *Int J Hydrogen Energy*, vol. 33, no. 9, pp. 2189–2199, May 2008, doi: 10.1016/j.ijhydene.2008.02.044.

[68] Y. Gao *et al.*, “Efficient generation of hydrogen by two-step thermochemical cycles: Successive thermal reduction and water splitting reactions using equal-power microwave irradiation and a high entropy material,” *Appl Energy*, vol. 279, Dec. 2020, doi: 10.1016/j.apenergy.2020.115777.

[69] A. Pérez *et al.*, “Hydrogen production by thermochemical water splitting with La0.8Al0.2MeO3-δ (Me= Fe, Co, Ni and Cu) perovskites prepared under controlled pH,” *Catal Today*, vol. 390–391, pp. 22–33, May 2022, doi: 10.1016/j.cattod.2021.12.014.

[70] M. T. Azcondo *et al.*, “Novel Perovskite Materials for Thermal Water Splitting at Moderate Temperature,” *ChemSusChem*, vol. 12, no. 17, pp. 4029–4037, Sep. 2019, doi: 10.1002/cssc.201901484.

[71] M. Orfila *et al.*, “Experimental evaluation and energy analysis of a two-step water splitting thermochemical cycle for solar hydrogen production based on La0.8Sr0.2CoO3-δ perovskite,” *Int J Hydrogen Energy*, Dec. 2022, doi: 10.1016/j.ijhydene.2022.03.077.

[72] Y. Chen, L. Zhang, Y. Zhang, H. Gao, and H. Yan, “Large-area perovskite solar cells-a review of recent progress and issues,” *RSC Advances*, vol. 8, no. 19. Royal Society of Chemistry, pp. 10489–10508, 2018. doi: 10.1039/c8ra00384j.

[73] B. Bulfin, J. Vieten, C. Agrafiotis, M. Roeb, and C. Sattler, “Applications and limitations of two step metal oxide thermochemical redox cycles; A review,” *Journal of Materials Chemistry A*, vol. 5, no. 36. Royal Society of Chemistry, pp. 18951–18966, 2017. doi: 10.1039/c7ta05025a.

[74] N. Gokon *et al.*, “Thermochemical H2O splitting using LaSrMnCrO3 of perovskite oxides for solar hydrogen production,” in *AIP Conference Proceedings*, Dec. 2020, vol. 2303. doi: 10.1063/5.0028720.

[75] K. H. Rigdon and A. H. Mcdaniel, “Solar thermochemical hydrogen production with complex perovskite oxides; Solar thermochemical hydrogen production with complex perovskite oxides.”

[76] M. Orfila, M. Linares, R. Molina, J. Á. Botas, R. Sanz, and J. Marugán, “Perovskite materials for hydrogen production by thermochemical water splitting,” *Int J Hydrogen Energy*, vol. 41, no. 42, pp. 19329–19338, Nov. 2016, doi: 10.1016/j.ijhydene.2016.07.041.

[77] L. Wang, M. Al-Mamun, P. Liu, Y. Wang, H. G. Yang, and H. Zhao, “Notable hydrogen production on LaxCa1−xCoO3 perovskites via two-step thermochemical water splitting,” *J Mater Sci*, vol. 53, no. 9, pp. 6796–6806, May 2018, doi: 10.1007/s10853-018-2004-2.

[78] X. Qian *et al.*, “Outstanding Properties and Performance of CaTi0.5Mn0.5O3–δ for Solar-Driven Thermochemical Hydrogen Production,” *Matter*, vol. 4, no. 2, pp. 688–708, Feb. 2021, doi: 10.1016/j.matt.2020.11.016.

[79] R. Del Toro, P. Hernández, Y. Díaz, and J. L. Brito, “Synthesis of La0.8Sr0.2FeO3 perovskites nanocrystals by Pechini sol–gel method,” *Mater Lett*, vol. 107, pp. 231–234, Sep. 2013, doi: 10.1016/J.MATLET.2013.05.139.

[80] J. V. Reis *et al.*, “Synthesis of CeNb3O9 perovskite by Pechini method,” *Mater Lett*, vol. 227, pp. 261–263, Sep. 2018, doi: 10.1016/J.MATLET.2018.05.093.

[81] J. Jouannaux, A. Haeussler, M. Drobek, A. Ayral, S. Abanades, and A. Julbe, “Lanthanum manganite perovskite ceramic powders for CO2 splitting: Influence of Pechini synthesis parameters on sinterability and reactivity,” *Ceram Int*, vol. 45, no. 12, pp. 15636–15648, Aug. 2019, doi: 10.1016/J.CERAMINT.2019.05.075.

[82] V. Berbenni, C. Milanese, G. Bruni, P. Cofrancesco, and A. Marini, “Solid state synthesis of CaMnO3 from CaCO3-MnCO 3 mixtures by mechanical energy,” *Zeitschrift fur Naturforschung - Section B Journal of Chemical Sciences*, vol. 61, no. 3, pp. 281–286, 2006, doi: 10.1515/znb-2006-0307.

[83] J. Vieten *et al.*, “Perovskite oxides for application in thermochemical air separation and oxygen storage,” *J Mater Chem A Mater*, vol. 4, no. 35, pp. 13652–13659, 2016, doi: 10.1039/c6ta04867f.

[84] B. Bulfin *et al.*, “Redox chemistry of CaMnO3 and Ca0.8Sr0.2MnO3 oxygen storage perovskites,” *J Mater Chem A Mater*, vol. 5, no. 17, pp. 7912–7919, 2017, doi: 10.1039/c7ta00822h.

[85] O. Levenspiel, *Chemical reaction engineering*.

[86] H. Schulz, “From the Kissinger equation to model-free kinetics: reaction kinetics of thermally initiated solid-state reactions,” *ChemTexts*, vol. 4, no. 3, Oct. 2018, doi: 10.1007/s40828-018-0062-3.

[87] A. Iasonna and M. Maginit, “POWER MEASUREMENTS DURING MECHANICAL MILLING. AN EXPERIMENTAL WAY TO INVESTIGATE THE ENERGY TRANSFER PHENOMENA,” 1996.

[88] N. Burgio, A. Iasonna, M. Magini, S. Martelli, and F. Padella, “Mechanical alloying of the Fe-Zr system. Correlation between input energy and end products,” *Il Nuovo Cimento D*, vol. 13, no. 4, pp. 459–476, Apr. 1991, doi: 10.1007/BF02452130.

[89] M. K. Beyer and H. Clausen-Schaumann, “Mechanochemistry: The mechanical activation of covalent bonds,” *Chemical Reviews*, vol. 105, no. 8. pp. 2921–2948, Aug. 2005. doi: 10.1021/cr030697h.

[90] C. Suryanarayana, “Mechanical alloying and milling / C. Suryanarayana Steel+Al sputter deposited coatings View project Mechanical alloying and milling,” 2007. [Online]. Available: www.elsevier.com/locate/pmatsci

[91] M. Magini and F. Padella, “0956-716X(95)00465-3 BALL MILLING: AN EXPERIMENTAL SUPPORT TO THE ENERGY TRANSFER EVALUATED BY THE COLLISION MODEL,” Acta Metallurgica Inc, 1996.

[92] A. Al-Azzawi, P. Baumli, and G. Mucsi, “Mechanical Alloying and Milling,” in *The publications of the MultiScience - XXIX. MicroCAD International Scientific Conference*, 2015. doi: 10.26649/musci.2015.017.

[93] “PLANETARY BALL MILL PM 100.” https://www.retsch.com/products/milling/ball-mills/planetary-ball-mill-pm-100/ (accessed Feb. 26, 2023).

[94] “PULVERISETTE 5/4- classic line.” https://www.fritsch-international.com/sample-preparation/milling/planetary-mills/details/product/pulverisette-54-classic-line/technical-details/ (accessed Feb. 26, 2023).

[95] U. Manual, “CP-4900 Micro-GC User Manual,” no. August, 2009.

[96] T. Banaszkiewicz, M. Chorowski, and W. Gizicki, “Comparative analysis of oxygen production for oxy-combustion application,” in *Energy Procedia*, 2014, vol. 51, pp. 127–134. doi: 10.1016/j.egypro.2014.07.014.

[97] *The Hydrogen Economy*. National Academies Press, 2004. doi: 10.17226/10922.

[98] R. R. Bhosale, “Thermodynamic efficiency analysis of zinc oxide based solar driven thermochemical H2O splitting cycle: Effect of partial pressure of O2, thermal reduction and H2O splitting temperatures,” *Int J Hydrogen Energy*, vol. 43, no. 32, pp. 14915–14924, Aug. 2018, doi: 10.1016/j.ijhydene.2018.06.074.

[99] R. R. Bhosale, A. Kumar, and P. Sutar, “Thermodynamic analysis of solar driven SnO2/SnO based thermochemical water splitting cycle,” *Energy Convers Manag*, vol. 135, pp. 226–235, 2017, doi: 10.1016/j.enconman.2016.12.067.

[100] R. R. Bhosale, A. Kumar, F. AlMomani, U. Ghosh, and M. Khraisheh, “A comparative thermodynamic analysis of samarium and erbium oxide based solar thermochemical water splitting cycles,” *Int J Hydrogen Energy*, vol. 42, no. 37, pp. 23416–23426, Sep. 2017, doi: 10.1016/j.ijhydene.2017.03.172.